Amyloidogenesis of a Type III-dependent Hpa1 and Structural analysis of a drug-pump repressor DNA complex

ZHANG, BING

Amyloidogenesis of a Type III-dependent Hpa1 and Structural analysis of a drug-pump repressor DNA complex

By

Bing Zhang B.Sc. (Hons)

A thesis submitted for the degree of Doctor of Philosophy

In

The School of Biological and Biomedical Sciences

University of Durham

May 2010

Declaration

I declare that the work presented herein is my own, except where stated by citation or statement, and has not been submitted for another degree in this or any other university.

Bing Zhang

5th May 2010

Acknowledgements

I would like to give my greatest thanks to Prof. Adrian R. Walmsley for his supervision, constant support and encouragement throughout this project and for the proof reading of this thesis; to Dr. M. Ines Borges-Walmsley for her discussion and guidance of VceR project; to Dr. Ehmke Pohl for his help and guidance in crystallization, structure analysis, crystal tests and data collection at SLS and DLS; to Dr. Santina Russo for her crystal tests and data collection at SLS, and preliminary data processing of the native data set; to Dr. Li Zhang for her discussion on crystallization methods and encouragement; to Dr. Hong Tin Lin for sharing of methods in liposome preparation; to Dr. Paul Yeo for the sharing of methods in sucrose gradient centrifugation; and to all my colleagues, Dr. Daliang Chen, Dr.Dijun Du, Mr. Jongwu Yang, Dr. Teresa Massam-Wu, Dr. Victoria Money and Dr. Thamarai Janganan, for their help in my Ph D study.

I would like to thank Prof. Rick Lewis at the University of Newcastle upon Tyne for his help in crystal tests at his lab and at the ESRF synchrotron source; to Prof. Gongyou Chen at the School of Agriculture and Biology, Shanghai Jiao Tong University, Shanghai, China, for his discussion of the Hpa1 project, encouragement from the beginning to the end of my Ph D study and for one year financial supporting for my experiments; to Dr. Baishi Hu in the Plant Pathology Department, Nanjing Agricultural University, Nanjing, China, for his encouragement.

This work would not be finished without a Wolfson Research Institute studentship and one year Welcome Trust studentship (awarded to Prof. Adrian R. Walmsley) that assisted me to undertake this project.

Further thanks to Diane Hart, Simon Padbury and Ian Edwards for their indispensable technical assistance.

Finally, I express my sincere thanks to all my family and friends in China.

Abbreviations

ABA	Abscisic acid
ABC	ATP binding cassette transporter
Avr	Avirulent
Aβ	Alzheimer's β-amyloid
Be	Berberine
CCCP	Carbonyl cyanide m-chlorophenyl-hydrazone
CD	Circular dichroism
CR	Congo red
CV	crystal violet
DDM	n-dodecyl-β-D maltoside
Dq	dequalinium
DLS	Diamond Light Source
DME	drug/metabolite efflux
DSP	eithiobis (succinimidyl propionate)
DTT	eithiothreitol
Et	ethidium
EGS	ethylglycol bis (succinimidyl succinate)
EPEC	enteropathogenic *Escherichia coli*
EM	electron micrograph
FAO	Food and Agriculture Organizationn
HR	hypersensitive response
HTH	helix-turn-helix
IAPP	islet amyloid polypeptide
IMP	inner-membrane protein
IR	inverted repeat
MAD	multiple-wavelength anomalous dispersion
MATE	multidrug and toxic compound extrusion family
MDR	multi-drug resistant
MF	major facilitator superfamily
MFP	membrane fusion protein
MG	malachite green

MIR	multiple isomorphous replacement
MIRAS	multiple isomorphous replacement with anomalous scattering
MR	molecular replacement
OMP	outer-membrane protein
PCR	polymerase chain reaction
R6G	rhodamine 6G
RND	resistance nodulation division family
R protein	resistence protein
RT	room temperature
SA	salicylic acid
SAD	single-wavelength anomalous dispersion
SDS-PAGE	sodium dodecyl sulfate polyacrylamide gel electrophoresis
SEC	size-exclusion chromatography
SIR	single isomorphous replacement
SIRAS	single isomorphous replacement with anomalous scattering
SLS	Swiss Light Source
SMR	small multidrug resistance
Tc	tetracycline
TEM	transmission electron microscopy
THP	Tris hydroxypropyl phosphine
Tip	transcription inducing peptide
TTSS	type III secretion system
Xoo	*Xanthomonas oryzae* pv. oryzae
Xoc	*Xanthomonas oryzae* pv. oryzicola

Abstract

Part I Amyloidogenesis of Type III-dependent Hpa1 from *Xanthomonas oryzae* pv. oryzicola

The first harpin, HrpN from *Erwinia amylovora*, the bacterium that causes fire blight of pear, apple and other rosaceous plants, was reported as an HR (hypersensitive response) elicitor in 1992. Similar harpins were found in *Pseudomonas syringae*, *Ralstonia solanacearum*, *Xanthomonas campestris*, *X. axopnpodis* and *X. oryzae*, and secreted through a Type III secretion system (TTSS), which is utilized by bacterial pathogens to invade the host. The wide presence and secretion pathway of harpins in plant pathogens indicate the important function of harpins in plant pathogenicity.

Herein, I report that Hpa1, the harpin of *X. oryzae* pv. oryzicola, assembles into fibrils at acidic pHs. As determined by analytical gel filtration chromatography, purified Hpa1 is a decamer. Hpa1 has two predicted α helical domains, located towards its N- and C-terminus, respectively. The C-terminal α helix domain is responsible for the fibril assembly, since the synthesized polypeptide (ASPLTQMLMNIVGEILQAQ), corresponding to the C-terminal α helix domain of Hpa1, could form fibrils. The mature fibrils of this peptide consist of three strands of protofibrils. We propose that the fibril formation by full length Hpa1 involves a conformational transition from α-helix to β-sheet structure, which exposes the C-terminal α helix domain for fibril assembly. In contrast to the assembly of fibrils by full length Hpa1 at acidic pH, that of synthesized polypeptide (ASPLTQMLMNIVGEILQAQ) is at acidic and basic pH, which may be an inherent characteristic of the sequence component. Interestingly, the N-terminal α helix domain (ISEKQLDQLLCQLIQALL) of Hpa1 inhibits the assembly of fibrils by the C-terminal domain polypeptide, suggesting that the intramolecular interaction of Hpa1 between the two α helix domains keeps Hpa1 in a non-fibrillar state.

In addition, the fibrils formed by full length Hpa1, the N-terminal truncated Hpa1 (55-138) and synthesized polypeptide (ASPLTQMLMNIVGEILQAQ) disrupted the

membrane of liposomes prepared from extracted lipids from *E. coli*, which suggests a new function for Hpa1- targeting and damaging the cell membrane.

Part II Crystallization and structure analysis of the *Vibrio cholerae* VceR drug-pump repressor with bound DNA

The VceR protein, from *Vibrio cholerae*, which is encoded by the *vceR* gene, represses transcription of the *vceCAB* operon, which encodes a multidrug efflux pump in this microorganism. This type of pump, composed of a tripartite protein complex that spans the inner and outer membranes, resembles type I secretion systems. VceR, which is a member of the TetR family of transcriptional repressors, binds specifically to a 28 bp inverted repeat (IR) located in the 107 bp *vceR-vceCAB* intergenic region.

In order to completely understand the structural basis and functional mechanism by which VceR binds DNA, we performed crystallization trials on the VceR/DNA complex, with the aim of determining its crystal structure. A number of oligos were screened, including 30 bp, 28 bp, 27 bp, 26 bp and 24 bp duplex, depending on the published operator sequence bound by VceR, to obtain X-ray quality VceR/DNA complex crystals for structure analysis. These crystals have space group I 4_122, with a=b=90.2 Å, c=298.1 Å, α=β=γ=90°.

To retrieve phase information, Se-Met substituted VceR and Br labelled DNA oligonucleotides were prepared and crystallized with unlabelled DNA and native VceR, respectively. Several three-wavelength MAD data sets from these crystals were collected and analyzed. A merged Se-Met data set, obtained from 2 data sets of three wavelengths and one peak data set, yielded the correct positions of 12 Se by ShelxD. Sharp/Autosharp was used to refine these 12 Se positions and for calculating phases. A preliminary electron density map shows, after solvent flattening, clear helical characteristics in the VceR dimer and a partial DNA backbone. A model with one VceR dimer and an 11 base pair duplex was built in the preliminary electron density map.

Contents

Chapter 2 Material and Method

Chapter 1 Introduction

Part I TTSS and harpin

1.1 Type III secretion system

The type III secretion system (TTSS) or type III secretion injectisome (different nomenclatures for the same system in various bacteria) is utilized by Gram-negative bacterial pathogens of animals and plants to deliver effectors (the substrate proteins of TTSS) to their host (Alfano and Collmer, 2004; Ghosh, 2004; Gurlebeck *et al.*, 2006). To date, TTSSs have been found in the plant pathogens *Pseudomonas syringae, Xanthomonas*, *Ralstonia*, *Erwinia*, and *Pantoea* (Alfano and Collmer, 2004) and animal pathogens *Yersinia*, *Salmonella, Pseudomonas aeruginosa, Shigella, Bordetella* and enteropathogenic *Escherichia coli* (EPEC) (Cornelis and Van Gijsegem, 2000).

TTSSs consist of a basal body, which is embedded in the inner and outer membranes of the bacterium, and a needle in animal pathogens or a pilus in plant pathogens, through which contact is made with the host cell (Figure 1.1 a, b &c) (Alfano and Collmer, 2004; Cornelis, 2006; Ghosh, 2004; Tampakaki *et al.*, 2004). TTSSs have been divided into seven different families, after the phylogenetic analyses of four conserved proteins, the cytoplasmic ATPase and the other three proteins from the inner membrane (Cornelis, 2006; Gophna *et al.*, 2003). The seven families are Chlamydiales, Hrp1, Hrp2, SPI-1, SPI-2, Rhizobium and Ysc family. TTSSs of plant pathogens belong to two families, Hrp1 and Hrp2 family, whereas those of animal pathogens locate to three families, SPI-1, SPI-2 and Ysc family (Cornelis, 2006). The other two families, Chlamydiales and Rhizobium are limited to the Chlamydiae phylum and the Rhizobiales order, respectively (Cornelis, 2006).

1.2 TTSSs and bacterial flagella

Components of the TTSS share sequence and structural similarities with those of the bacterial flagellum, which is a motility organelle (Tampakaki *et al.*, 2004). Flagella

consist of a rotating long filament and a rotary motor, which correspond to the pilus or needle, and basal body in TTSS, respectively (Figure 1.1). Before effector export, TTSSs secrete the external components, including the needle (or pilus in plant pathogens) and translocator (or translocon in plant pathogens), which is similar to the flagellar system in secretion its own hook and filament subunits for the flagellum assembly (Cornelis, 2006; He and Jin, 2003; Ferris and Minamino, 2006; Macnab, 2003; Tampakaki *et al.*, 2004). The TTSS is thought to have evolved from the flagellum, or that the TTSS and the flagellum share a common ancestor (Gophna *et al.*, 2003; He and Jin, 2003).

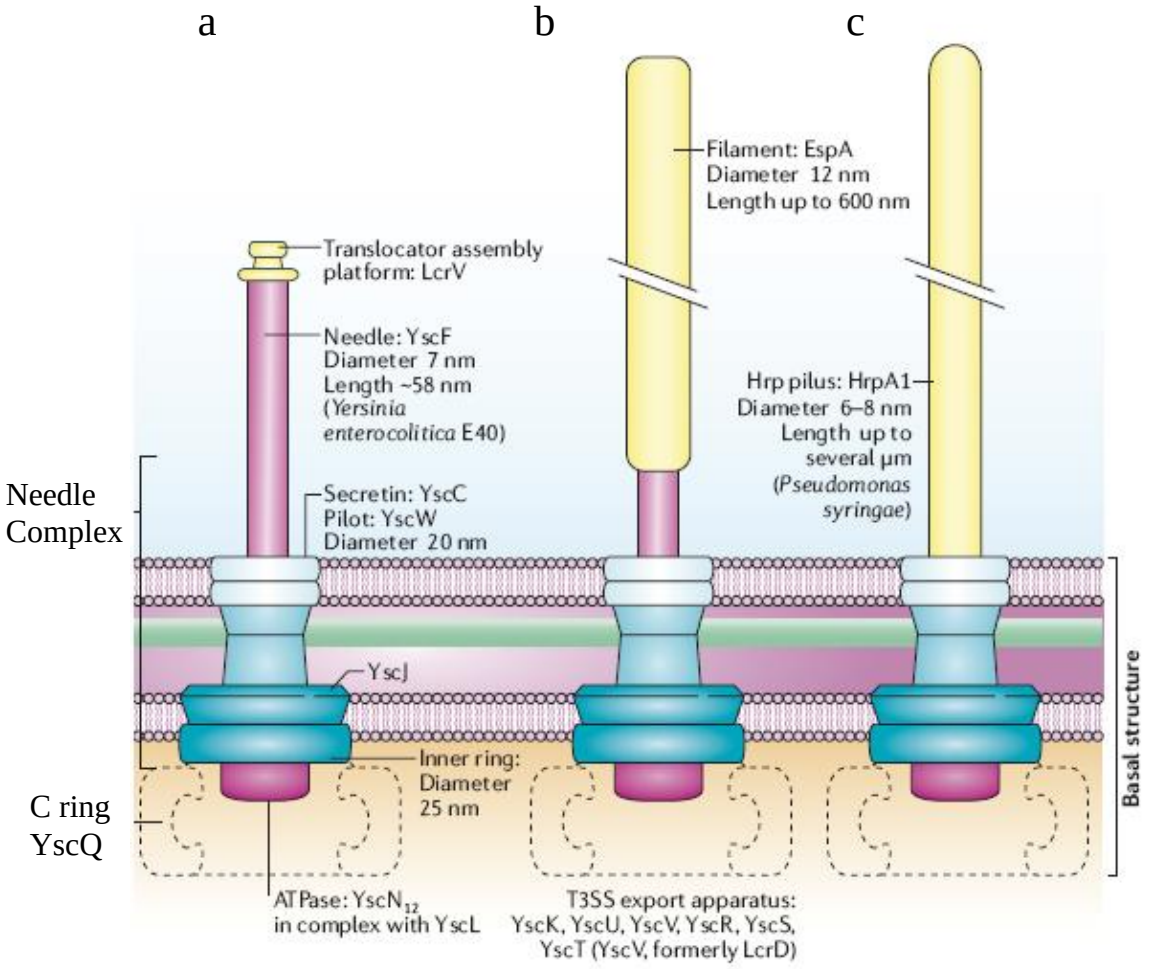

Figure 1.1 Structure of the TTSSs. Schematic representation of Ysc TTSS (a), TTSS from EPECs (b) and the TTSS from plant pathogens (c) (Cornelis, 2006).

Plant pathogen *Xanthomonas oryzae* proteins	Animal pathogen *Yersinia pestis* proteins	Sequence identity (%)	Function/ location
HrcC	YscC	27.9	Secretin Outer membrane protein
HrcJ	YscJ	37.2	MS ring Lipoprotein
HrcN	YscN	57.3	ATPase Ring with 6-fold symmetry
HrcQ	YscQ	21.4	Putative C ring
HrcR	YscR	49.5	Basal structure Inner membrane protein
HrcS	YscS	38.3	Basal structure Inner membrane protein
HrcT	YscT	27.6	Basal structure Inner membrane protein
HrcU	YscU	32.3	Basal structure Inner membrane protein
HrcV	YscV	41.5	Basal structure Inner membrane protein

Table 1.1 Nine core components of TTSS in plant and animal pathogen. Sequence alignment was performed by SIM at Expasy. (Alfano and Collmer, 1997; Cornelis, 2006; Macnab, 2003).

1.3 Components of TTSS

The TTSS has two components, the basal structure and the needle or pilus (Figure 1.1 a, b & c). The basal structure spans the outer and inner membrane of the bacterium. There are approximately 25 proteins required to assemble the TTSS, nine of which form a core, including one outer membrane protein (secretin), 6 inner membrane proteins, one ATPase and one possible C-ring forming protein (Table 1.1) (Cornelis, 2006; Ghosh, 2004).

1.4 TTSS of *Xanthomonas oryzae*

1.4.1 *Xanthomonas oryzae*

X. oryzae pv. oryzae (*Xoo*) and *X. oryzae* pv. oryzicola (*Xoc*) are bacterial pathogens of rice, which result in bacterial leaf blight and bacterial leaf streak, respectively (Gnanamanickam *et al.*, 1999; Seo *et al.*, 2008; Zou *et al.*, 2006). Bacterial leaf blight and bacterial leaf streak are widely distributed in tropical and subtropical Asia, West Africa, South America, and Australia (Seo *et al.*, 2008). Leaf streak can cause grain weight losses of up to 32% and leaf blight induces crop loss of up to 50% (Gnanamanickam *et al.*, 1999). The main differences between *Xoo* and *Xoc* are in the invasion entry point and colonization location (Seo *et al.*, 2008). *Xoo* gains access to the xylem through wounds or natural openings such as hydathodes and invades rice vascular tissue (Seo *et al.*, 2008). *Xoc* enters the leaf mainly through stomata and colonizes the mesophyll parenchyma tissue (Seo *et al.*, 2008). The genomes of *Xoo* and *Xoc* are similar with respect to size, G+C percent, and gene content (Seo *et al.*, 2008). The pathogenicity in susceptible host rice and the hypersensitive response in nonhost tobacco of *Xoo* and *Xoc* are dependent on TTSSs, which translocate effectors to host or nonhost (Alfano and Collmer, 2004; Gurlebeck *et al.*, 2006; Zou *et al.*, 2006). An understanding of the molecular mechanism of the pathogenicity of *Xoo* and *Xoc* on the basis of TTSS could provide new strategies for their management and the means to decrease the loss in rice yield.

1.4.2 TTSS of *Xanthomonas oryzae* pv. oryzicola

TTSSs of *Xoo* and *Xoc* are encoded by *hrp* (hypersensitive response and pathogenesis) genes cluster, including *hrp*, *hpa* (hrp-assoicated) and *hrc* (*hrp* conserved) genes (Alfano and Collmer, 2004; Zou *et al*., 2006). The nine *hrp* genes (encoded proteins are shown in Table 1.1) of *Xanthomonas oryzae*, which are highly conserved in plant and animal bacterial pathogens, are designated as the *hrc* genes (Bogdanove *et al.*, 1996).

The expression of the *hrp* gene cluster is induced by contact with the plant or in minimal media that mimics the condition of the plant apoplast (Alfano and Collmer, 2004).

Substrates of TTSSs of *Xoo* and *Xoc* are the extracellular components (pilus, translocon and other uncharacterized parts) of the secretion apparatus, effectors (Section 1.4.3) and harpins (Section 1.5 for harpins) (Alfano and Collmer, 2004). Interactions between effectors of the TTSS and the plant result in resistance or susceptibility in pathogenesis (Bent and Mackey, 2007; Chisholm *et al.*, 2006; Jones and Dangl, 2006). The phenotype of TTSS is hypersensitive response in nonhost plant and pathogenesis in host plant (Alfano and Collmer, 2004; Zou *et al.*, 2006).

Although *Xoo* and *Xoc* are important rice pathogens, little work is published about *hrp* and *hrc* genes from these two bacteria. Studies of *X. campestris* species would help us understand the TTSSs of *Xoo* and *Xoc.* Well studied proteins of TTSS in *X. campestris* are HrpE, HrpF, HrcN, HpaA, HpaB and HpaC.

HrpE (9.7 kDa) was found to be the major component of *X. campestris* pv. vesicatoria Hrp pilus by the N-terminal sequencing of all the proteins purified from the Hrp pili and further HrpE-specific antibody labelling of the pilus (Weber *et al.*, 2005).

HrpF in *X. campestris*, secreted by the TTSS, forms the translocon, which is a pore-like structure that inserts into the host cell membrane for the translation of effectors. The N-terminus of HrpF has a signal sequence for secretion and its C-terminal hydrophobic region is the functional domain. *In vitro*, HrpF forms pores in planar lipid bilayers (Buttner *et al*., 2002).

HrcN in *X. campestris* is the ATPase of TTSS, which is thought to provide the energy for the secretion process (Lorenz and Buttner, 2009). However, in flagellar type III secretion, the proton motive force is recognized as the energy source for TTSS secretion (Paul *et al.*, 2008). The ATPase of the TTSS, which forms a ring structure, is located in the cytoplasm and associates with inner membrane protein HrcU from the TTSS (Pozidis *et al*., 2003; Lorenz and Buttner, 2009). Another function of the ATPase in the TTSS is to dissociate the effector and chaperone complex (Akeda and Galan, 2005; Lorenz and Buttner, 2009). HrcL in *X. campestris* interacts with and stabilizes HrpN; its homolog YscL in *Yersinia* is a negative regulator of the ATPase (Blaylock *et al.*, 2006; Lorenz and Buttner, 2009).

HpaB in *X. campestris* is thought to be a general TTSS chaperone (Buttner *et al.*, 2004). Generally, chaperones of the TTSS have a low molecular weight (about 15 kDa), low isoelectric points (<6) and a predicted amphipathic region in the C-termini (Alfano and Collmer, 2004). These chaperones interact with effectors and maintain them in a nonglobular state before secretion via passage through the narrow TTSS (Alfano and Collmer, 2004). HpaB interacts with several effectors, and promotes their secretion, but prevents the delivery of HrpF (translocon) (Buttner *et al*., 2004).

HpaC, which interacts with HrcU, acts as a substrate specificity switch protein of *Xanthomonas* TTSS (Lorenz *et al*, 2008 b). The substrate specificity switch of TTSS, which is the mechanism used by TTSS to secrete the pilus, translocon and effector sequentially, is well characterized in animal pathogenic bacteria. This mechanism is achieved through a conformational change of a cytoplasmic part of the inner membrane protein, Spa40 of *Shigella* (Deane *et al.*, 2008), YscU of *Yersinia* (Edqvist *et al.*, 2003; Sorg *et al.*, 2007) and EscU of EPEC (Zarivach *et al.*, 2008), which have an autocleavage property. In *X. campestris*, HrcU has a similar autocleavage property (Lorenz *et al*, 2008 b). HpaC inhibits the secretion of HrpB2, which is required for pilus assembly (Lorenz *et al*, 2008 b). In addition, both HpaC and HrpB2 interact with the C-terminal domain of HrcU, but not with the full length protein (Lorenz *et al*, 2008 b). Given that HpaC promotes secretion of the translocon and effector, HpaC presumably switches the secretion of HrpB2 to that of translocon and effector (Lorenz *et al*, 2008 b).

In addition, HpaA interacts with the C-terminal domain of HpaB. To achieve stepwise secretion of effector and pilus, binding of HpaA to HpaB was thought to prevent secretion of effectors during pilus assembly (Lorenz *et al*, 2008 a).

1.4.3 TTSS effectors of *Xoo* and *Xoc*

The effectors of phytopathogenic TTSSs are the Avr (avirulent) proteins, which are thus designated because they were detected through gain-of-function avirulence phenotypes (Alfano and Collmer, 2004), and the other class of proteins, including Hop (Hrp outer protein) in *Pseudomonas* (Alfano and Collmer, 2004), Xop (*Xanthomonas* outer protein) in *Xanthomonas* (Gurlebeck *et al*., 2006), and Pop

(*Pseudomonas* outer protein, as based on a previous genus designation) in *Ralstonia* (Arlat *et al.*, 1994).

Effectors of phytopathogenic TTSS are important virulence factors and suppress plant defenses (Alfano and Collmer, 2004; Kay and Bonas, 2009). Effectors of *Xoo* and *Xoc* include Avr proteins and Xops (Alfano and Collmer, 2004; Gurlebeck *et al.*, 2006; Kay and Bonas, 2009). The molecular function of most effectors from *Xoo* and *Xoc* is still unknown (Kay and Bonas, 2009).

Pathogens secrete Avr proteins into hosts that carry cognate R (resistence) proteins, and results in the resistance interaction, hypersensitive cell death response (HR) (section 1.5.1 for HR) (Alfano and Collmer, 2004; Cornelis and Van Gijsegem, 2000; Gabriel, 1999). However, if the host is without the cognate *R* gene, the secretion of Avr proteins into the host results in susceptibility and the pathogen invades the host successfully (Alfano and Collmer, 2004; Cornelis and Van Gijsegem, 2000). There is another kind of resistance, nonhost resistance (Heath, 2000b), in which the pathogen secretes an Avr protein into the nonhost and the Avr protein is perceived by an R protein from nonhost that induces nonhost resistance. An example of nonhost resistance is that of the *avrRxo1* gene from the rice pathogen *Xoc* that confers the nonhost defense reaction on maize with the resistance gene *Rxo1* (Zhao *et al.*, 2004; Zhao *et al.*, 2005).

AvrXa7, AvrXa10 and AvrXa21 are well studied effectors of *Xoo*. AvrXa7 and AvrXa10 are members of AvrBs3 family, which are targeted to the nucleus of the plant cell, where they modulate plant gene expression (Gurlebeck *et al.*, 2006; Yang *et al.*, 2000; Yang and White, 2004; Zhu *et al.*, 1998). Different members of the *avrBs3* family have diverse repeat numbers of 102–bp in the central repeat domain. *avrXa10* and *avrXa7* have 15.5 and 25.5 copies of this repeat domain, respectively (Zhu *et al.*, 1998).

AvrXa7 shows avirulence after injection into rice carrying *Xa7* and virulence in rice lacking *Xa7* (Yang and White, 2004). AvrXa7 has a C-terminal nuclear localization signal and acidic transcriptional activation domain, and central codon repeated domain (Yang and White, 2004). The central codon repeated domains of *avrXa7* and

avrXa10 determine their avirulence specificity to *Xa7* and *Xa10*, respectively (Zhu *et al.*, 1998). The binding of AvrXa7 to double stranded DNA was confirmed, which indicates AvrXa7 may interact with host DNA (Yang *et al.*, 2000).

1.5 Harpins

1.5.1 Harpins and HR

Harpins are secreted by TTSS of bacterial pathogens of plants but are different from the other effectors of TTSS (Alfano and Collmer, 2004). Harpins are heat-stable, glycine-rich proteins that induce a hypersensitive response (HR) when infiltrated into the intercellular space of nonhost leaves (Alfano and Collmer, 2004; Gurlebeck *et al.*, 2006; Zou *et al.*, 2006).

Several harpins have been reported: HrpN of *Erwinia amylovora* (Wei *et al.*, 1992), HrpZ of *P. syringae* (He *et al.*, 1993; Lee *et al.*, 2001), PopA of *Ralstonia solanacearum* (Racape *et al.*, 2005), HpaG of *Xanthomonas axopnpodis* pv. glycines (Kim *et al.*, 2004), Hpa1 of *X. oryzae* pv. oryzae (Zhu *et al.*, 2000) and XopA of *X. campestris* pv. vesicatoria (Noel *et al.*, 2002). These harpins have low sequence identity between each others. An example is HrpN, which has 13.6% sequence identity with HrpZ, 10.6% with PopA, 4.8% with HpaG, 5.8% with Hpa1 and 5.6% with XopA (Sequence alignment was performed by SIM at Expasy).

The importance of harpins lies in that it is the first protein reported to be an HR elicitor (Wei *et al.*, 1992). HR, analogous to the innate immune system found in animals, is a mechanism used by plants to prevent the spread of infection by microbial pathogens. The HR manifests as patches of localized cell death at the infection site, which limits the pathogen to the infection site (Greenberg, 1996; Heath, 2000a).

1.5.2 Harpin's beneficial function on plants

Harpins can activate ethylene, salicylic acid (SA) and abscisic acid (ABA) signal transduction, which are plant defense pathways, and thus have some beneficial

effects on the plant, such as increasing disease resistance, insect defense and plant growth (Dong *et al.*, 2005; Shao *et al.*, 2008).

Harpins induce the disease resistance after being sprayed on or expressed in the plant (Dong *et al.*, 1999; Shao *et al.*, 2008). HrpN, the harpin from *E. amylovora*, induces resistance to *P. syringae* pv. tomato DC3000 and *Peronospora parasitica* in Arabidopsis, after spraying on the plant (Dong *et al.*, 1999). In this induction, harpin acts through an endogenous plant defence SA (salicylic acid) signal transduction pathway (Dong *et al.*, 1999).

HrpN also activates the ethylene signalling pathway and thus inhibits aphid reproduction after spraying onto Arabidopsis and enhances Arabidopsis growth (Dong *et al.*, 2004). These two effects are dependent on the ethylene receptor gene and inhibition of ethylene perception also abolishes these two effects (Dong *et al.*, 2004).

In the other research, HrpN was found to induce drought tolerance in Arabidopsis through initiating the ABA signalling relevant gene expression and promoting stomatal closure (Dong *et al.*, 2005).

Harpins are widely used to engineer pathogen-resistance and in crop improvement. Expression of Hrf1, the harpin from *X. oryzae* pv. oryzae, in rice confers resistance to *Magnaporthe grisea* (Shao *et al.*, 2008) and in tobacco increases the resistance to tobacco mosaic virus, to the bacterial pathogen *Ralstonia solanacearum* and to the fungal pathogen *Alternaria alternata* (Peng *et al.*, 2004). The transgenic tobacco plants expressing *hrpN* have accelerated growth and develop enhanced resistance to *Botrytis cinerea*, which is a necrotrophic fungal pathogen (Jang *et al.*, 2006). HpaG, a harpin protein from *X. oryzae* pv. oryzicola, was found to increase yield and quality of green tea (Wu *et al.*, 2007).

1.5.3 Harpin binding sites in plant

Considering the important function of harpins in plants, there are a number of studies that indicate the target of harpin in plants, plant cell wall or plasma membrane and the target proteins of harpin were identified.

Plant cell wall or plasma membrane

$HrpZ_{Psph}$, the harpin of *P. syringae* pv. phaseolicola, was reported to bind to lipid membranes and induce ion-current fluctuations in planar lipid bilayers at concentrations as low as 2 nM, which indicates pore-forming acitivity of $HrpZ_{Psph}$ (Lee *et al.*, 2001). As a result, $HrpZ_{Psph}$ was thought to target plasma membranes.

PopA, the harpin of *Ralstonia solanacearum*, also binds to membrane lipids in a Ca^{2+}-dependent manner *in vitro* and forms Na^{+}-conducting pores (Racape *et al.*, 2005). *In vivo*, immunogold labelling of PopA locates this harpin to the plasma membrane of plants (Racape *et al.*, 2005).

In other research, $harpin_{Pss}$, the harpin of *P. syringae* pv. syringae, was localized in the plant cell wall by fluorescent signal. Extraction of Ca^{2+} and pectins from cell walls by a chelating agent, EGTA, blocked the binding of harpin to the cell walls (Hoyos *et al.*, 1996).

Harpin interacting proteins

A protein binding site located in HrpZ, the harpin of *P. syringae*, was reported (Li *et al.*, 2005). A library of random peptides was used to screen for HrpZ interacting peptides, which confirmed a consensus amino acid motif to be bound by HrpZ (Li *et al.*, 2005). This peptide binding domain was localized to the central region of HrpZ (Li *et al.*, 2005). Further study using antiserum raised against this HrpZ binding peptide recognize acidic proteins in bean, tomato, parsley and Arabidopsis, and HrpZ shows affinity for the protein from bean (Li *et al.*, 2005). However, the sequences of these proteins were not confirmed in this study.

Proteins from Arabidopsis (*Arabidopsis thaliana*), rice (*Oryza sativa*), and apple (*Malus*) have been identified that interact with HrpN, the harpin from *Erwinia amylovora* (Oh and Beer, 2007). HIPM (HrpN-interacting protein from *Malus*) was first identified through yeast two-hybrid screens using the gene for the HrpN protein as bait to screen a cDNA prey library from Gala apple (Oh and Beer, 2007). In addition, AtHIPM (*Arabidopsis thaliana* HIPM) and OsHIPM (*Oryza sativa* HIPM) were found in the genome databases of Arabidopsis and rice according to sequence of HIPM (Oh and Beer, 2007). HIPM, AtHIPM and OsHIPM are all small proteins, about 60 amino acids in length (Oh and Beer, 2007). They have a putative signal peptide at the N-termini and one transmembrane domain, which would locate them to the plasma membrane (Oh and Beer, 2007). In accordance with this prediction, HIPM and AtHIPM GFP fusion proteins were found to be localized to the plasma membrane (Oh and Beer, 2007). The N-terminus 198 amino acids of HrpN were found to be the functional domain for the interaction with HIPM (Oh and Beer, 2007).

AtHIPM was found to be a negative regulator of plant growth, as the *AtHIPM* knockout mutation in Arabidopsis exerts a positive effect on the growth of the aerial parts (top growth) (Oh and Beer, 2007). HrpN also loses its effect on the growth of Arabidopsis with *AtHIPM* knockout mutation (Oh and Beer, 2007). In addition, overexpression of AtHIPM reduces Arabidopsis growth (Oh and Beer, 2007). These findings indicate that HrpN inhibits the function of AtHIPM and thus enhances plant growth (Oh and Beer, 2007).

1.5.4 Harpin-like proteins

There is another class of harpin-like proteins, which have a harpin domain and another domain that has an alternate function (Kvitko *et al.*, 2007). HrpW of *P. syringae* pv. tomato and *E. amylovora* have an N-terminal domain that is similar to harpins, which is glycine rich and able to elicit the HR when the purified domain fragment is infiltrated into tobacco leaf, and a C-terminal domain homologous to pectate lyases from *E. carotovora*, *E. chrysanthemi* and *Bacillus subtilis* (Charkowski *et al.*, 1998; Kim and Beer, 1998). The pectate lyase domain (32.5% sequence identity with fungal pectate lyase PelC from *Nectria haematococca*) of HrpW of *P. syringae* pv. tomato has no pectate lyase activity, but could bind to

pectate which suggests that the target of HrpW could be in the plant cell wall (Charkowski *et al.*, 1998).

HopAK1 and HopP1 of *P. syringae* pv. tomato DC 3000 have a C-terminal enzyme-like domain, pectate lyase (56.1% sequence similarity to *Bacillus licheniformis* pectate lyase PelB) and lytic transglycosylase (HopP1 has three conserved sequence motifs which are predicted to be required for lytic transglycosylase activity), respectively, and an N-terminal harpin domain (HrpW-like domain, 45% similarity to HrpW from *P. syringae* pv. tomato) (Kvitko *et al.*, 2007). Together with HrpZ1 of *P. syringae* pv. tomato DC 3000, there are four harpins in this strain (Charkowski *et al.*, 1998; Kvitko *et al.*, 2007).

1.5.5 Harpin forming fibrils

The ability of harpin to form amyloid fibrils was initially reported in 2007 (Oh *et al.*, 2007). HpaG, the harpin of *X. axonopodis* pv. gylcines, was found to form β-sheet-rich fibrils in *hrp* induction minimal medium XVM2 (XVM2: 20 mM NaCl, 10 mM $(NH_4)_2SO_4$, 5 mM $MgSO_4$, 1 mM $CaCl_2$, 0,16 mM KH_2PO_4, 0.32 mM K_2HPO_4, 0,01 mM $FeSO_4$, 10 mM sucrose, 10 mM fructose and 0.03% casamino acid, at pH 6.7) or apoplastic fluid (Oh *et al.*, 2007). Fibrils formed by HpaG produce green birefringence after staining with Congo red (Oh *et al.*, 2007). Circular dichroism (CD) spectroscopic analysis of spherical oilgomers of HpaG shows an α-helix structure which transforms into a β-sheet after the fibrils form (Oh *et al.*, 2007). In addition, amyloidogenesis has been taken as the cause of HR, after the finding that HR-null mutants lack the ability to form fibrils (Oh *et al.*, 2007).

Other harpins, XopA from *X. campestris* pv. vesicatoria, HrpZ of *P. syringae* pv. syringae and HrpN of *E. amylovora*, also formed fibrils in XVM2 (Oh *et al.*, 2007).

1.6 Amyloid fibrils

Amyloid fibrils are formed during the process of fibrillar protein aggregation, in which the protein adopts an ordered-β structure (Chiti and Dobson, 2006; Fändrich, 2007).

In vivo, amyloid fibril aggregation induces human neurodegenerative diseases, e.g., Alzheimer's and Parkinson's disease (Petkova *et al.*, 2002) and nonneuropathic systemic amyloidoses, e.g., type II diabetes (Chiti and Dobson, 2006; Kajava *et al.*, 2005). It is thought that more than 100 different human pathological conditions are associated with amyloid fibril formation (Fändrich, 2007). Table 1.2 shows the main diseases and proteins or peptides involved.

Main fibril constituent protein or fragment	Disease
$A\beta_{40}$ peptide	Alzheimer's disease
huntingtin	Huntington's disease
α-synuclein	Parkinson's disease
human amylin	Type II diabetes

Table 1.2 A summary of the main diseases and the proteins or peptides involved (Stefani and Dobson, 2003).

Nonpathological amyloid fibrils have specific functional roles, e.g., curli from *E. coli* facilitates binding to host proteins; prion from *Saccharomyces cerevisiae* terminates mRNA translation; and spidroin from *Nephila edulis* forms the silk fibers of the web (Chiti and Dobson, 2006). Nature uses the high elasticity and persistence of amyloid fibrils to build natural materials (Kelly and Balch, 2003).

In vitro, several partially unfolded soluble proteins can form amyloid fibrils when they undergo a transition from a α helix to β sheet under conditions of high temperature, e.g. transthyretin (Ferrao-Gonzales *et al*., 2000); high pressure, e.g. truncated form of hamster prion protein ($SHaPrP_{90–231}$) (Torrent *et al.*, 2004; Torrent *et al.*, 2006); low pH, e.g. human prion protein and calcium-binding equine lysozyme (Gerber *et al*., 2008; Kumar *et al*., 2007; Malisauskas *et al*., 2003); or moderate

concentrations of organic solvents, e.g. α-synuclein and beta2-microglobulin (Chaudhary *et al*., 2008; Chiti and Dobson, 2006; Lee *et al*., 2008).

Besides these full-length proteins, there are several polypeptide segments of these fibril-forming proteins involved in amyloid fibril formation, e.g. $A\beta_{40}$ peptide associated with Alzheimer's disease, and human amylin relevant to type II diabetes. Amyloid fibril forming polypeptide chains are dramatically diverse in their sizes and sequences. The poly-amino acids from myoglobin that form amyloid fibrils *in vitro* are α helical in their native state (Fändrich *et al.*, 2001). Some poly-amino acids and short designed peptides are intrinsically unable to fold into globular conformations and revert into the alternative structural state, amyloid fibrils (Fändrich and Dobson, 2002; Lopez De La Paz *et al.*, 2002; Tjernberg *et al.*, 2002).

1.6.1 Common structure of amyloid fibrils

Several studies suggest that amyloid fibrillization is a multistep process that involves various intermediate forms, including spherical oligomers, protofibrils and mature amyloid fibrils (Glabe, 2006).

Spherical oligomers are an intermediate state in the pathway of fibril formation, which ranges from dimers up to particles of a million Dalton (Glabe, 2006), that have been observed by EM. These spherical oligomers, also called micelles, have a diameter of approximately 3-10 nm (Glabe, 2006). Protofibrils are thought to be curly and wormlike, have a thin diameter about 2-5 nm and consist of flat β-sheets with an overall long-range twist, which has minimal rotations (about 1-3°) between successive peptide strands (Jimenez *et al.*, 1999; Jimenez *et al.*, 2002; Uversky and Fink, 2004). Figure 1.2a shows the EM of apomyoglobin protofibrils. Mature fibrils consist of more than one protofibril wound around a core that may in some cases be hollow, which have a diameter 6-12 nm and a linear, straight and regular appearance (Uversky and Fink, 2004). A 3D reconstruction of an insulin amyloid mature fibrils is shown in Figure 1.2b.

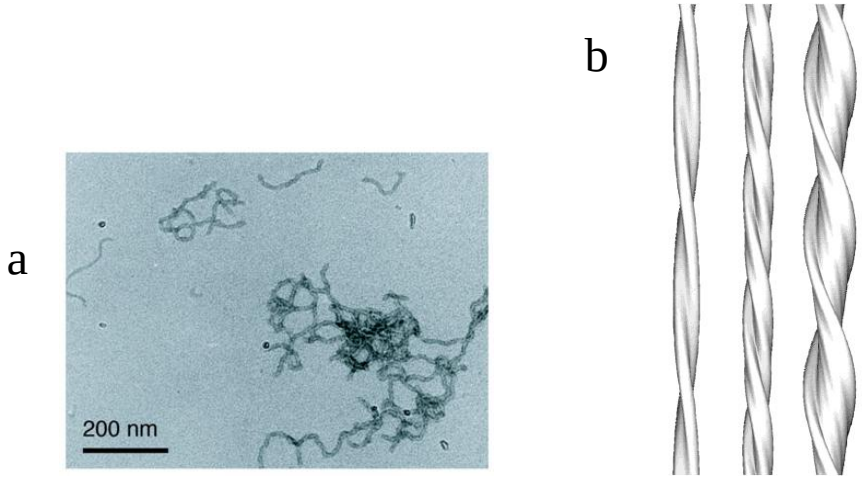

Figure 1.2 Electron micrograph of fibrils (a) Electron micrograph of apomyoglobin protofibrils (Fändrich *et al*., 2003). (b) 3-D reconstruction of insulin mature fibrils twisted from protofilaments. Left is twisted by a pair of protofilaments. Middle is twisted by four protofilaments. Right is twisted by six protofilaments. (Jimenez *et al*., 2002)

1.6.1.1 Structure models of $A\beta_{1\text{-}40}$ fibrils and amylin

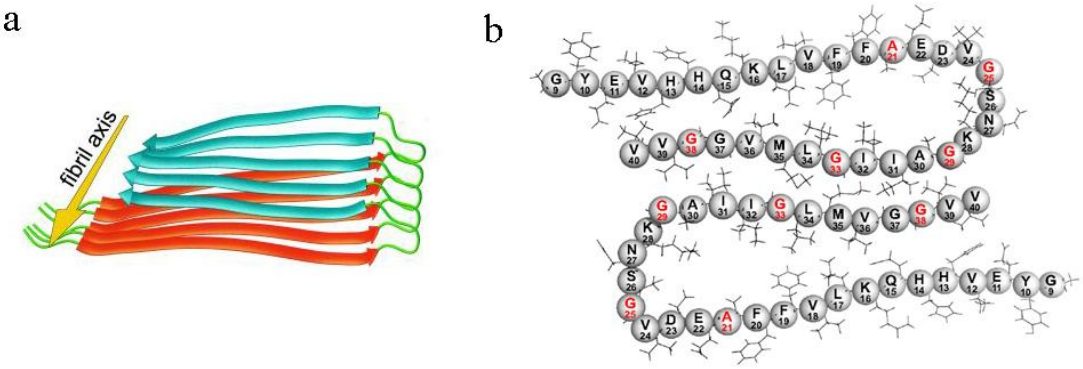

Figure 1.3 A structural model for $A\beta_{1\text{-}40}$ fibrils. (a) Schematic representation of a single molecular laryer. The yellow arrow indicates the direction of the long axis of the fibril. (Petkova *et al.*, 2002) (b) A cross section of two laterally displaced molecular layers of the $A\beta_{1\text{-}40}$ fibrils. The long axis of the fibril is perpendicular to the page. (Petkova *et al.*, 2002)

The Alzheimer's β-amyloid (Aβ) peptides are derived from partial proteolysis of the larger transmembrane protein, the β-amyloid precursor protein (Benzinger *et al.*, 2000). The Aβ fibril is a hydrogen-bonded, parallel β-sheet (Figure 1.3a) (Benzinger *et al.*, 1998). A structural model for $A\beta_{1\text{-}40}$ has been suggested, based on solid-state NMR, that a single protofilament is composed of two fundamental units (Figure 1.3b) (Petkova *et al.*, 2002). Every fundamental unit is a double-layered β-sheet structure,

which is formed by residue 12-24 and 30-40 (Petkova *et al.*, 2002). The mature amyloid fibril formed by $A\beta_{1-40}$ peptide consists of two protofilaments (Sachse *et al.*, 2008).

Human amylin, a 37 amino acid long peptide, produced by cleavage from a pro-amylin precursor protein, forms amyloid fibrils and is associated with type 2 diabetes (Kajava *et al.*, 2005). An amylin structural model has been proposed by Kajava, *et al*. (Figure 1.4) (Kajava *et al.*, 2005). In this model, three β-strands consisting of residues 12-17, 22-27 and 31-37 form a serpentine core and the first eight residues form a disulfide-bonded loop (Kajava *et al.*, 2005). Three amylin protofilaments (Figure 1.4b) coil to form fibrils with a left-handed coiling (Kajava *et al.*, 2005).

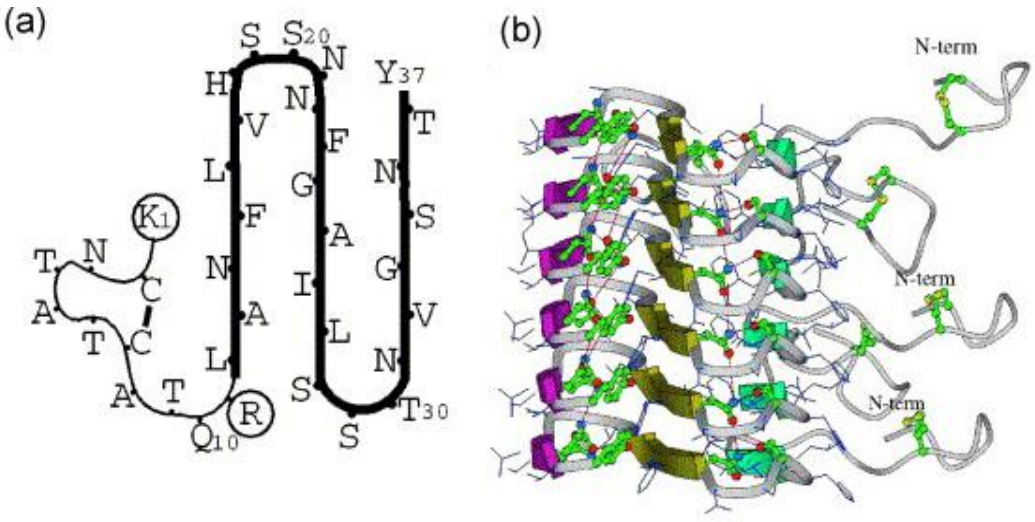

Figure 1.4 Amylin structure model. (a) Diagram of the proposed β-serpentine fold for human amylin. The model has three β-strands. (b) The protofilament model of human amylin. The three β-strands of the serpentine are marked by arrows with different colors (blue, yellow and purple). Ladders formed by H-bonding of Asn22, -31 and -35, Ser19 and Tyr37 are shown by red broken lines. (Kajava *et al.*, 2005)

1.6.1.2 Atomic structure of fibril forming segments

The availability of microfocus beamlines at the European Synchrotron Radiation Facility and Swiss Light Source allowed the crystal structure analysis of microcrystals formed by fibril forming segments, which range from 4 to 7 residues in length (Nelson *et al.*, 2005; Sawaya *et al.*, 2007).

The atomic structure of GNNQQNY, a fibril-forming segment from the yeast Sup35, presents that its fundamental unit is a pair of β-sheets, which are formed by unspecific van der Waals interactions of interdigitating side chains from each β-sheet, named 'steric zipper' by the authors (Figure 1.5) (Nelson *et al.*, 2005). Each pair of β-sheets is formed from parallel β-strands by hydrogen-bonds (Nelson *et al.*, 2005). The interface between two sheets of a β-sheet pair only involves van der Waals interaction without water and thus is a dry interface. In contrast to the dry interfaces, the wet interfaces between pairs of β-sheets are lined with water molecules, which hydrate the polar side chains (Figure 1.5b).

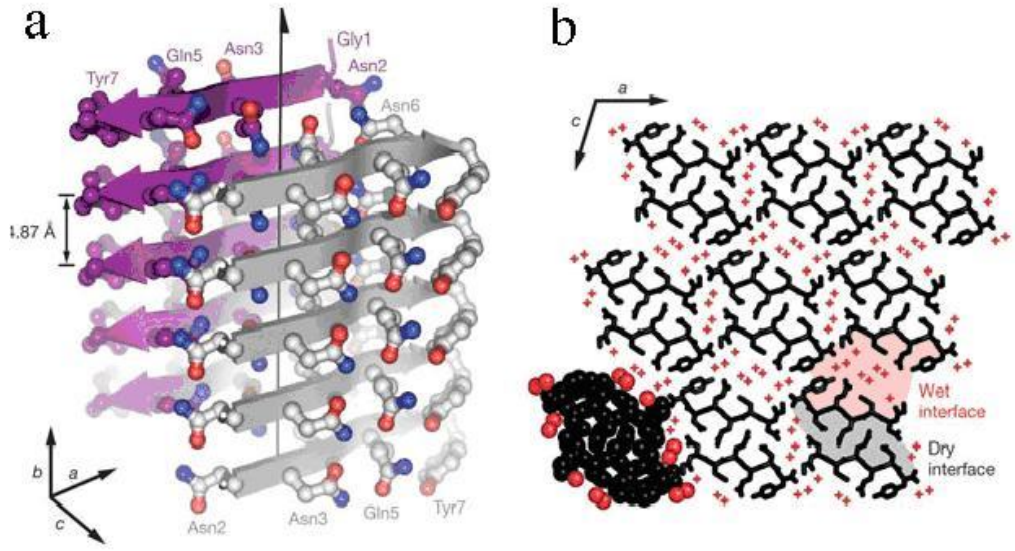

Figure 1.5 Structure of GNNQQNY. (a) The pair-of-sheets structure, showing the backbone of each β-strand as an arrow, with side chains protruding. The dry interface is between the two sheets, with the wet interfaces on the outside surfaces. (b) The GNNQQNY crystal packing viewed down the sheets (from the top of panel a, along the b axis). Red crosses indicate the water molecule. The dry interface is shown in grey and the wet interface is shown in pink. (Nelson *et al.*, 2005)

Further studies of atomic structures of fibril-forming segments, NNQQ from yeast prion Sup35, VQIVYK from tau (a microtubule binding protein in Alzheimer's disease), GGVVIA and MVGGVV from amyloid-β, LYQLEN and VEALYL from insulin, SSTSSA from RNase, and SNQNNF from PrP, reveal similar β-sheet pairs and steric zippers formed by the interactions between the residue side chains of mating β-sheets, which might be a general characteristic in amyloid structures (Sawaya *et al.*, 2007).

1.6.2 Mechanisms of amyloid fibril formation

A possible mechanism for amyloid fibril formation, nucleation and growth, has been proposed (Chiti and Dobson, 2006; Collins *et al.*, 2004; Serio *et al.*, 2000; Vestergaard *et al.*, 2007). The intermolecular contacts of specific segments of the protein form a nucleus, which is a slow reaction and the least stable intermediate (Chiti and Dobson, 2006; Vestergaard *et al.*, 2007). Following a lag phase for nucleation, there is a rapid exponential growth phase in which there is further association of either monomers or oligomers within the nucleus (Chiti and Dobson, 2006; Collins *et al.*, 2004; Vestergaard *et al.*, 2007). Fragmentation of already formed fibrils, taken as seeds, increases the reaction of nucleation by circumventing the beginning of nucleus formation (Stohr *et al.*, 2008).

1.6.3 Pathogenicity of amyloid fibrils

Initally, amyloid fibrils were taken as the species responsible for cell toxicity and death. However, recent studies provide evidences that the intermediate state, the soluble amyloid oligomers, is the main cytotoxic species (Chiti and Dobson, 2006).

Soluble amyloid oligomers of different amyloidogenic proteins and peptides were reported to have a common structural motif (Kayed *et al.*, 2003). In this publication, the antibody produced by rabbit vaccination with Aβ peptides not only specifically recognizes the oligomeric state of Aβ, but the soluble oligomers among all other types of amyloidogenic proteins and peptides, regardless of sequence, such as islet amyloid peptide, ploylglutamine, lysozyme and human insulin (Kayed *et al.*, 2003). Since the protein function is determined by the three-dimensional structure, the common structure of different amyloidogenic proteins and peptides implies that they also share a common pathological function and act on the same primary target of cells (Kayed *et al.*, 2003). The plasma membrane is assumed to be the primary target of the amyloid oligomer (Kayed *et al.*, 2003).

In explanation of the pathogenicity or toxicity of soluble oligomers or fibrils, several mechanisms, including membrane disruption, ion channel forming and

permeabilization of membrane, have been proposed (Engel *et al.*, 2008; Kayed *et al.*, 2004; Quist *et al.*, 2005).

Kayed *et al.*, 2004 found that soluble oligomers from diverse amyloids (Abeta40 of Alzheimer disease, α-synuclein of Parkinson disease, IAPP of type II diabetes, polyglutamine of Huntington disease and prion [106-206] of prion disease) that increase lipid bilayer conductance independent of the sequence (Kayed *et al.*, 2004). In their study, the increasing conductance is conformation-specific and no channel or pore is formed.

Quist *et al.*, 2005, showed that amyloid molecules form the ion channels, including Aβ of Alzheimer disease, α-synuclein of Parkinson disease, amylin of Type II diabetes, in membrane by AFM (Quist *et al.*, 2005).

However, Engel *et al.*, 2008 reported the human islet amyloid polypeptide (IAPP) damaged the membrane through the fibril growing on the membrane (Engel *et al.*, 2008). In this study, the kinetic profile of IAPP-induced membrane leakage matches that of IAPP fibril formation, which correlates the membrane damage with fibril growth. Furthermore, seeding increased fibril formation and also membrane damage. Insulin, the inhibitor of IAPP fibril growth, protects against IAPP-induced membrane damage.

In summary, the pathogenicity of amyloid fibrils, or their precursor oligmers, might lie in their effect on the plasma membrane, either disrupting the membrane or via the formation of ion channels in the membrane.

1.7 Hpa1

The Food and Agriculture Organization (FAO) of the United Nations pointed out that there are still 77 food-deficit countries all over the world (Crop prospects and food situation, No. 4, November 2009, FAO). Rice is the most important food for a large part of the world's human population and its bacterial pathogen *Xoc* induces rice loss of up to 50% (Gnanamanickam *et al.*, 1999). Thus, the management of *Xoc* to improve the rice yield is one practical way to provide more food.

A TTSS is used by *Xoc* to translocate effector proteins into host rice and is thus responsible for its pathogenicity (Alfano and Collmer, 2004; Zou *et al*., 2006). An understanding of the molecular mechanism of the TTSS of *Xoc* and its role in pathogenicity could provide a basis for the management of *Xoc* to bring about a decrease in the loss in rice yield. Hpa1, the harpin of *Xoc*, is secreted by the TTSS and induces HR in nonhost tobacco (Zou *et al*., 2006). Although Hpa1 is a substrate of the TTSS, the pathogenicity of Hpa1 in host is still enigmatic. We sought to elucidate the structure and function of Hpa1 in order to further our understanding of its pathogenic role.

Recently, HpaG, the harpin of *X. axonopodis* pv. glycines, was reported to form amyloid fibrils (Oh *et al*., 2007). The aggregation of amyloid fibrils *in vivo* is associated with about 100 human pathological conditions (Fändrich, 2007). Hpa1 has high sequence identity (59.7%) with HpaG; and so we sought to test whether Hpa1 assembles into amyloid fibrils as does HpaG? Assuming Hpa1 formed amyloid fibrils, we aim to address the following questions: (i) what are the conditions for amyloid fibril assembly of Hpa1; (ii) is there a segment or motif present within Hpa1 responsible for fibril assembly; (iii) what is the function of Hpa1 fibrils in conferring pathogenicity?

Part II Regulators of MDR transporter

1.8 Multi-drug resistance (MDR)

Although the development of resistance against antimicrobials is due to natural selection in response to naturally occurring environmental sources, the abuse of antibiotics in the clinic has resulted in an immense selective pressure and emergence of antibiotic resistance (Harrison and Svec, 1998). Multi-drug resistant (MDR) bacteria can survive in the presence of potentially lethal doses of structurally diverse drugs that now threaten to compromise effective chemotherapy. The emerging global crisis of MDR has led to an urgency in the development of new therapeutic approaches to circumvent resistance mechanisms (Harrison and Svec, 1998; McKeegan *et al*., 2004). Extensive study and understanding of the molecular mechanisms underlying the development of MDR could provide clues in developing new inhibitors to combat resistant bacteria.

The mechanisms used by MDR bacteria to acquire resistance to antimicrobial agents are summarized in the following three types (Walsh, 2000).

1) Drug modification, e.g. production of β-lactamases for hydrolysis of the β-lactam ring.

2) Modification of the cellular target, e.g. changes in fluoroquinolone binding sites of DNA gyrase resulting in resitance to ciprofloxacin.

3) Pumping out the antibiotic e.g. drug efflux pumps.

Generally, drug efflux pumps consist of an inner membrane protein and a cytoplasmic membrane fusion protein, acting with an outer membrane protein to extrude drugs from cells (Borges-Walmsley *et al.*, 2003; Zgurskaya and Nikaido, 2000). MDR transporters can be divided into six families: the ATP binding cassette (ABC) transporters, which couple the hydrolysis of ATP to drug efflux; the major facilitator superfamily (MF); resistance nodulation division (RND) family; the drug/metabolite efflux (DME); small multidrug resistance transporters (SMR) family;

and multidrug and toxic compound extrusion (MATE) family (Borges-Walmsley *et al.*, 2003; Kumar and Schweizer, 2005). MF, SMR, RND and DME family are proton-driven antiporters and MATE tranporters are Na^+-driven transporters (Borges-Walmsley *et al.*, 2003; Kumar and Schweizer, 2005). Figure 1.6 shows five well-characterised families of multidrug efflux pump.

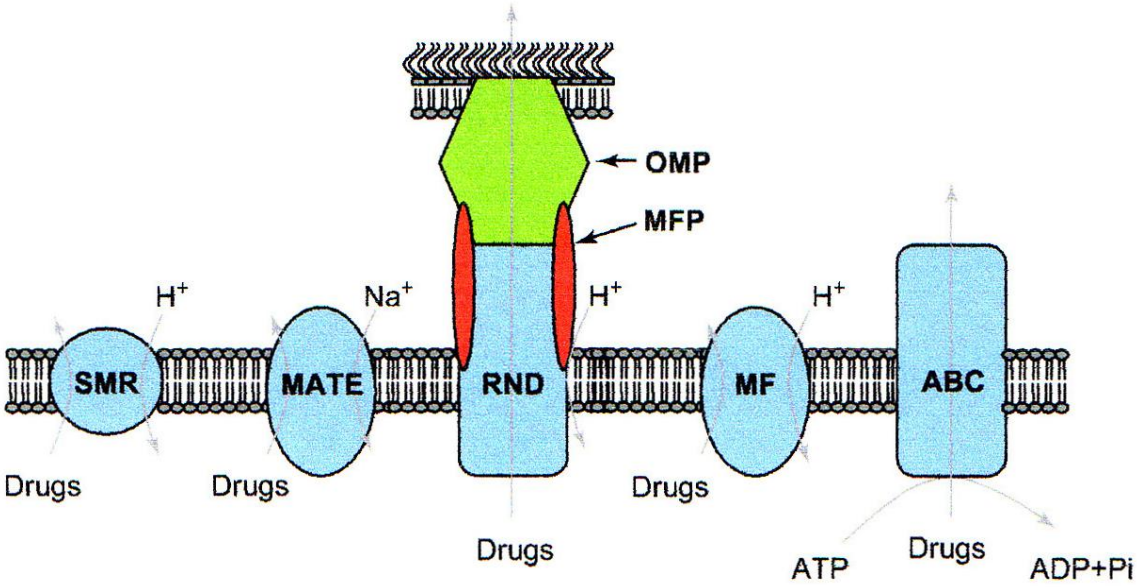

Figure 1.6 Five well-characterised families of multidrug efflux pump SMR family transports are proton-driven antiporters and have 4 TMS (transmembrane spanning helices); MATE family transports are Na^+-driven transporters; RND family transports are proton-driven antiporters and have 12 TMS and MF family transports are proton-driven antiporters and have 12 TMS. ABC transporters are powered by ATP hydrolysis. (McKeegan *et al.*, 2004).

1.9 Transcriptional regulation of multidrug transport systems

Excessive expression of bacterial MDR transporters could be deleterious, because this could cause the physical disruption of the membrane integrity or unwanted export of essential metabolites (Schumacher *et al.*, 2001; Schumacher and Brennan, 2002). The transcriptional regulation of MDR genes has been found in proton-motive force dependent efflux pumps, the major facilitator superfamily (MF) and resistance nodulation division (RND) family (Schumacher *et al.*, 2001; Schumacher and Brennan, 2002). However, SMR family and partial RND and MF family pump genes express constitutively, which reflects unknown physiological roles for the unregulated pumps in normal cellular metabolism (Schumacher and Brennan, 2002).

In addition, two-component regulatory systems have also been characterized in regulation of MDR genes, in which a membrane-linked kinase senses the signal, and a corresponding response regulator affects the outcome (Schumacher *et al.*, 2001; Schumacher and Brennan, 2002).

The regulators of bacterial multidrug transport systems belong to one of four regulatory protein families, the AraC, MarR, MerR, and TetR families, the assignment of which is based on the similarities detected within the DNA-binding domains of the regulator (Schumacher and Brennan, 2002). The transcriptional regulation of MDR transporter acts at a local or global level (Schumacher and Brennan, 2002). Extensively studied local regulators of drug transporter are *E. coli* TetR, repressor of tetracycline efflux; *Bacillus subtilis* BmrR, activator of Bmr pump; and *Staphylococcus aureus* QacR, repressor of QacAB pump. Well characterized global regulators are *E. coli* MarA, the global activator of the AcrAB-TolC pump; and *N. gonorrhoeae* MtrA, the global activator of the MtrCDE pump.

Considering that transcriptional regulatory proteins bind many of the diverse antimicrobials that are also substrates of the pumps they regulate, the study of cytosolic regulatory proteins will not only provide understanding of the regulation mechanism of MDR transportion, and thus provide a strategy in overcoming MDR, but could also reveal the drug recognition and binding of regulators, which could be targets for drug design to overcome antibiotic-resistant bacteria.

1.10 TetR family of transcriptional repressors

TetR family transcriptional repressors are widely distributed among bacteria and involved in the regulation of multidrug resistance pumps, catabolic pathways, the biosynthesis of antibiotics, osmotic stress, and the pathogenicity of Gram-negative and Gram-positive bacteria (Ramos *et al.*, 2005). They are also involved in the adaptation to complex and changing environments (Ramos *et al.*, 2005).

Members of the TetR family exhibit a high degree of sequence similarity at the helix-turn-helix (HTH) DNA binding domain, but low sequence similarity in the signal sensing domain, which indicates the differences in the function of this family (Ramos *et al.*, 2005). It is proposed that members of the TetR family function in a similar

manner: the binding of an inducer molecule to the C-terminal signal sensing domain induces a conformational change in the conserved DNA-binding domain, resulting in the release of the repressor from the operator, allowing transcription of the regulated downstream genes (Grkovic *et al.*, 2001; Ramos *et al.*, 2005)

1.10.1 TetR

The broad-spectrum antibiotic Tc (tetracycline) binds to the small ribosomal subunit and thus interrupts polypeptide chain elongation (Buck and Cooperman, 1990). The tetracycline repressor TetR, regulates the expression of TetA, which acts to export the tetracycline-magnesium complex, $[MgTc]^+$, and itself, by binding to specific DNA operators (Grkovic *et al*., 2001; Hinrichs *et al.*, 1994; Kisker *et al.*, 1995; Orth *et al.*, 1998a). There are two adjacent inverted repeats, named *tet* operators O_2 and O_1, which overlap the *tetA* and *tetR* promoters. The binding of TetR to operator O_2 represses *tetA* alone and to operator O_1 represses both the *tetA* and *tetR* genes. TetR has a fourfold-higher affinity to operator O_2 than to operator O_1 (Grkovic *et al*., 2001; Kisker *et al*., 1995; Orth *et al*., 1998a).

Upon binding of $[MgTc]^+$, TetR changes its conformation and dissociates from the operators, which results in the expression of TetR and TetA and subsequently the export of $[MgTc]^+$ by TetA (Hinrichs *et al*., 1995). The affinity of TetR for $[MgTc]^+$ is greater than that of $[MgTc]^+$ to ribosomes, subsequently ensuring *tetA* expression and $[MgTc]^+$ export before the inhibition of protein synthesis (Orth *et al*., 1998b).

TetR monomer has 10 α-helices. Helices α2 and α3 constitute the helix-turn-helix (HTH) motif for DNA binding, which is connected to the regulatory domain, helices α5- α10, through helix α4 (Ramos *et al.*, 2005; Hinrichs *et al.*, 1994; Orth *et al.*, 2000). The dimerization of TetR is achieved by the interaction of α8 and α10 with the symmetry-related α8’ and α10’ (Hinrichs *et al*., 1994; Kisker *et al.*, 1995).

1.10.1.1 TetR and $[Mg\text{-}Tc]^+$ complex structure

The crystal structures of the class D TetR in complex with $[Mg\text{-}7HTc]^+$ (tetracycline) and $[Mg\text{-}7ClTc]^+$ (7-chlorotetracycline, the hydrogen atom at C-7 is replaced by Cl) were determined (Hinrichs *et al.*, 1994; Kisker *et al.*, 1995). The TetR homodimer

binds two tetracycline-Mg^{2+} complexes in binding tunnels within the regulatory domains of TetR. α helices 4 to 8 and α8' and α9' (a prime refers to the second subunit of the dimer) form the first Tc binding pocket, and α helices 4' to 8' and 8 and 9 form the second site (Orth *et al.*, 1999).

The interactions between TetR and Tc-Mg include hydrogen bonding, hydrophobic interactions and Mg^{2+} coordination (Hinrichs *et al.*, 1994; Kisker *et al.*, 1995; Orth *et al.*, 1999). The functional groups of Tc involved in hydrogen bonding and Mg^{2+} coordination determine the antibiotic activity of Tc, as modifications of them abolish the antibiotic activity (Hinrichs *et al.*, 1994). In detail, Mg^{2+} is octahedrally coordinated by the chelating ketoenolate group O-11/O-12 of Tc, N^{ε} of His-100, and by three water molecules. Two of these water molecules are hydrogen bonded to the carboxylate of Glu-147' (Figure 1.7) and the other one forms a hydrogen bond to the hydroxyl group O^{γ} of Thr103. In addition, the Nε of His-64 and NH of Gln-116 form hydrogen bonds with Tc amide oxygen in position 2 and negatively charged oxygen in position 3. The O-3 and N-4 of the Tc are bridged to the amide side chain of Asn-82 by hydrogen bonds. The phenyl ring of Phe-86 forms an aromatic hydrogen bond with hydroxyl group O-121 of Tc. (Hinrichs *et al*., 1994; Orth *et al.*, 1999).

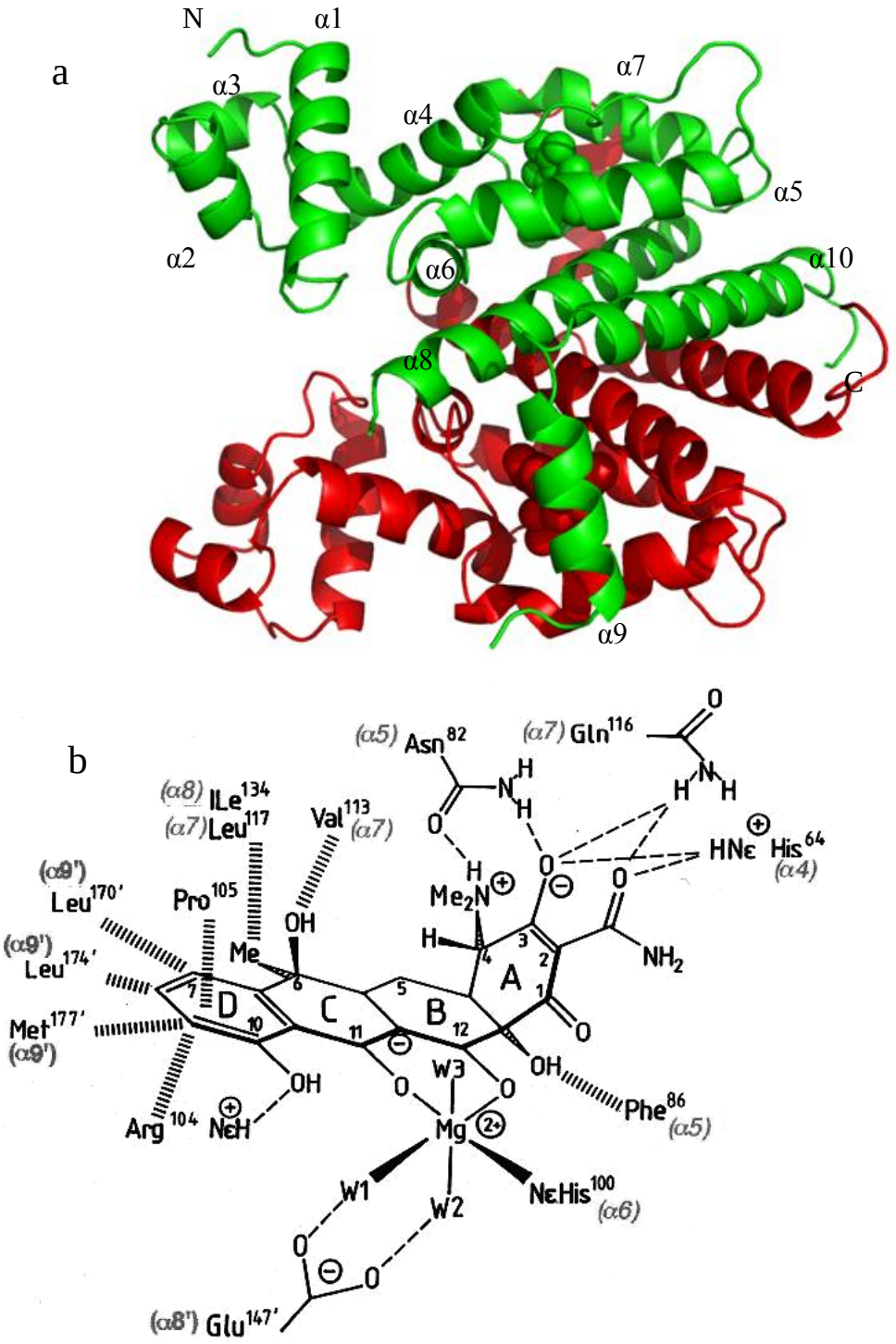

Figure 1.7 Structure of TetR in complex with [Mg-Tc]$^+$ (a) Ribbon drawing of the TetR/Mg-7ClTc dimer (PDB code: 2TRT), one complex in green, the other in red (Kisker *et al.*, 1995). The figure was prepared using PyMOL (DeLano, 2002). (b) Chemical structure of tetracycline and schematic representation of the interaction between tetracycline and TetR. Hydrogen bonds are represented by dashed lines; hydrophobic interactions are shown by hashed lines. W1, W2 and W3 are water molecules in the octahedral coordination shell of Mg^{2+} and Me represent methyl. Charges are marked (+) and (-). (Hinrichs *et al.*, 1994)

In the interaction with $[Mg\text{-}Tc]^+$, the side chains of TetR were divided into three categories (Orth *et al.*, 1999). Group I consists of His64, Asn82, Phe86 and Gln116, which are located at the far end of the binding tunnel. Functional groups of Tc ring A form hydrogen bonds with the side chains of these residues. Group II comprises Val113, Leu131, Ile134, Leu170', Leu174' and Met177', which form nonpolar van der Waals contacts to the hydrophobic part of $[Mg\text{-}Tc]^+$. Group III consists of His100, Thr103 and Glu147', which are involved in direct or water-mediated Mg^{2+} coordination (Orth *et al.*, 1999).

The comparison of structures of $[TetR]_2$ (TetR dimer, inducer-free), $[TetR\text{-}7ClTc]_2$ (TetR dimer complexed with two 7ClTc without Mg), [TetR-7ClTc]·[TetR-Mg7ClTc] (TetR dimer complexed with one 7ClTc and one Mg7ClTc) and $[TetR\text{-}Mg7ClTc]_2$ (TetR dimer complexed with two Mg7ClTc) shows the binding of $[Mg\text{-}Tc]^+$ to TetR in sequential steps (Orth *et al.*, 1999). The first step of $[Mg\text{-}Tc]^+$ binding is the insertion of $[Mg\text{-}Tc]^+$ into the binding tunnel and results in hydrogen bonding between ring A of Tc and group I residues. The second is the rotation of Tc around ring A, which produces the hydrophobic contacts and positions the chelated Mg^{2+} appropriate for binding to His100. (Figure 1.7b) (Orth *et al.*, 1999). There are two other amino acid residues, Thr103 and Glu147', involved in binding Mg^{2+}. The binding of Mg^{2+} to Thr103 (the first amino acid residue of α6 C-terminus) forces its side chain to shift by 2.5 Å (Orth *et al.*, 1999). Subsequently, α6 unwinds to adopt a β turn conformation and α4 performs a pendulum-like motion. Therefore, it is Mg^{2+} that initiates helix unwinding in TetR induction (Orth *et al.*, 1999).

1.10.1.2 TetR and its bound DNA

The crystal structure of the class D TetR bound with its 15 bp operator DNA, which overlaps the promoters for *tetA* and *tetR*, shows the HTH motifs of TetR in contact with two major grooves in B-form DNA (Figure 1.8) (Orth *et al.*, 2000; Grkovic *et al.*, 2001). These two major grooves are widened to 14-14.5 Å, compared with the canonical B-DNA 11.7 Å (Figure 1.8) (Orth, *et al.*, 2000). Another characteristic of TetR bound with its operator DNA is the bend of each half operator DNA, which is caused by kinking at base pair 2 from TetR and compensating by bending of base

pairs 3-6 to TetR , which results in the almost parallel ends of the 15-mer DNA (Orth, *et al*., 2000).

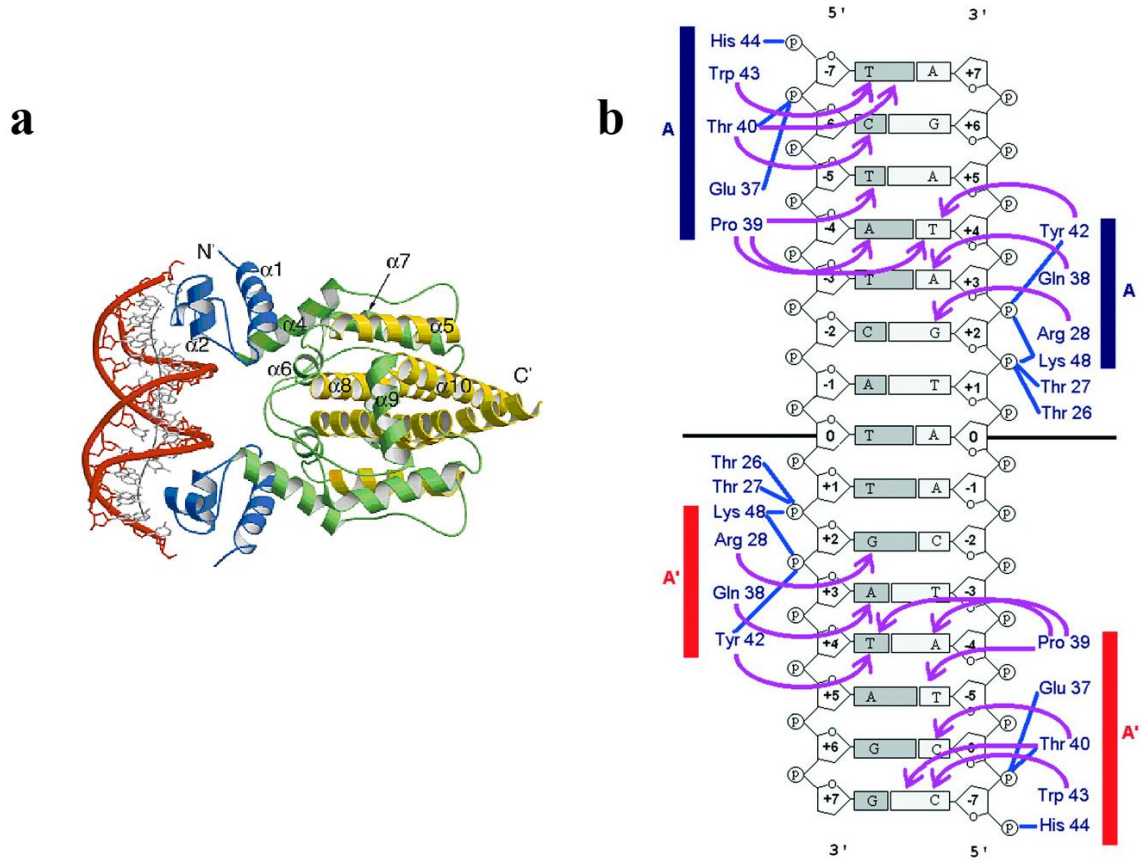

Figure 1.8 Structure of the TetR-*tetO* complex. (a) Ribbon representation of the overall structure of the TetR-*tetO* complex. α-helices of the homodimeric TetR are labelled in one monomer. The helices that form the DNA binding domain are colored blue; the helices that form the rigid scaffold are colored yellow, the rest of the helices that undergo conformational changes after the binding of inducer are colored green. (b) Schematic representation of the interactions of TetR dimer with its 15 bp operator. The interactions between specific nucleotides and polypeptides shown by arrows and those between phosphate backbones and polypeptides indicated by blue lines. (Grkovic *et al.*, 2001; Orth *et al.*, 2000)

The interaction of TetR with operator DNA is shown in Figure 1.8. The central three pairs are taken as the spacer and do not contribute to the protein-DNA interaction. The TetR monomer A binds the main strand from positions –4 to –7 and contacts the complementary strand from operator positions +4 to +2. The symmetric monomer A' binds the main strand from positions +2 to +4 and the complementary strand from positions –4 to –7. The specific contacts between the side chains of TetR and bases in the operator DNA are A3-Gln38 and G2-Arg28 by bidentate hydrogen bonding, and

T4-Pro39 and T5-Tyr42 by van der Waals interactions. Helix α3 (from Gln38 to His44) is the main element responsible for sequence-specific recognition. Lys48 from α4, out of the HTH motif, also establishes contacts with the target DNA region.

1.10.1.3 The induction mechanism of TetR

A structural comparison of induced (Mg-Tc bound) and non-induced TetR (DNA bound) found the center-to-center separation of recognition helices α3 and α3' in the operator complex changes from 36.6 Å to 39.6 Å after Mg-Tc binding. In explanation of the induction mechanism of TetR, signal transduction between the operator-binding interface and Mg-Tc binding site was proposed. This process is initiated from the shift of helix α6 in its C-terminal direction by 1.5 Å and the conformational change of its C-terminal turn to a type II β-turn (Orth *et al.*, 2000). In concert, α8 is extended by one turn in its C-terminus and the N-terminal turn of α7 adopts a 3_{10}-helical conformation on induction (Orth *et al.*, 1998b).

These changes force the central part of α4 to shift in the same direction, as the van der Waals contact between α4 and α6. Figure 1.9 shows the insertion of Mg-Tc into the binding tunnel to initiate the pendulum like motion of the N-terminus of α4. This motion of α4 and α4' (a prime refers to the second unit of the dimer) shifts the N-terminal DNA-binding domain apart, increases the separation of the recognition helices α3, α3' and causes the dissociation of the TetR/operator complex (Orth *et al.*, 2000).

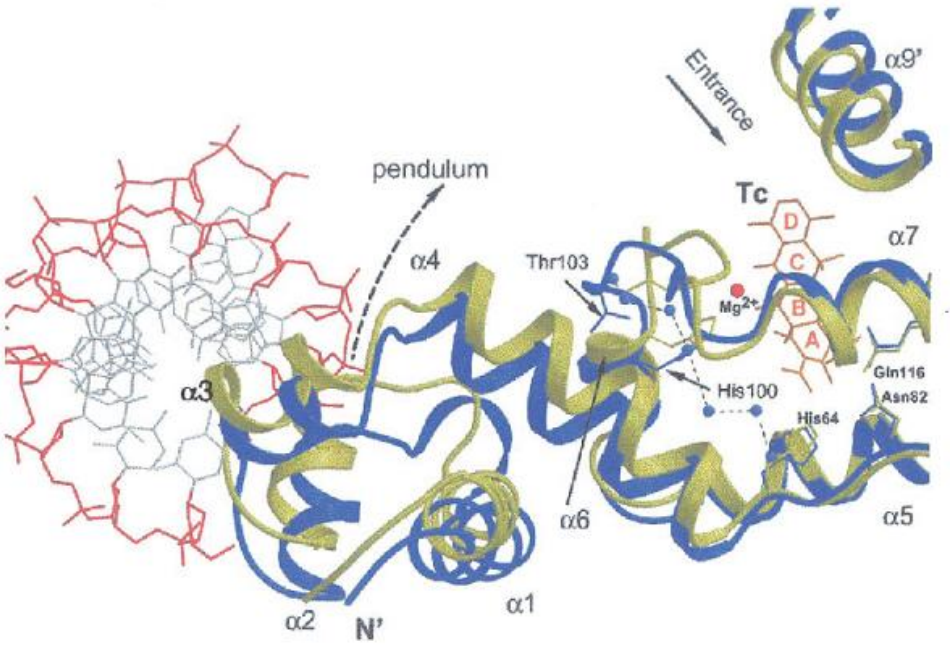

Figure 1.9 The conformational changes of TetR associated with [Mg-Tc]$^+$ binding Comparison of TetR in induced (yellow) and DNA-bound form (blue). The DNA phosphate-ribose backbone is shown in red, base in grey, Tc in orange and Mg^{2+} in red, the water molecules that constitute the water zipper in the induced conformation as blue spheres, which locks the DNA binding domain in a conformation unable to bind to the operator. (Grkovic *et al.*, 2001; Orth *et al.*, 2000)

1.10.1.4 TetR peptide inducer

Besides Tc and its derivatives, a 16-residue peptide (WTWNAYAFAAPSGGGS), called Tip (transcription inducing peptide), was found to mimic Tc, to induce TetR in *E. coli*, when fused to the N or C terminus of thioredoxin (Klotzsche *et al*., 2005; Luckner *et al.*, 2007). Tip was identified from a phage display library. Tc could displace the peptide Tip from the TetR-Tip complex, indicating that there is competition between Tip and Tc for TetR binding (Klotzsche *et al*., 2005).

The crystal structure of the Tip-TetR complex revealed that four residues (Trp1, Thr2, Trp3 and Asn4) of Tip occupy the Tc binding pocket (Figure 1.7b and Figure 1.10a), eight amino acids interact with residues to the surface of TetR and the other four residues are not visible in the electron density maps (Luckner *et al*., 2007). As there is an absence of Mg^{2+} in the structure of Tip-TetR, the indole nitrogen of Trp1 from Tip forms a hydrogen bond with the carbonyl oxygen of Thr103 of TetR. Tip

residues Thr2 and Asn4 form polar interactions with TetR residues Glu147', Asp148' and His 151' (Luckner *et al*., 2007) (Figure 1.10a).

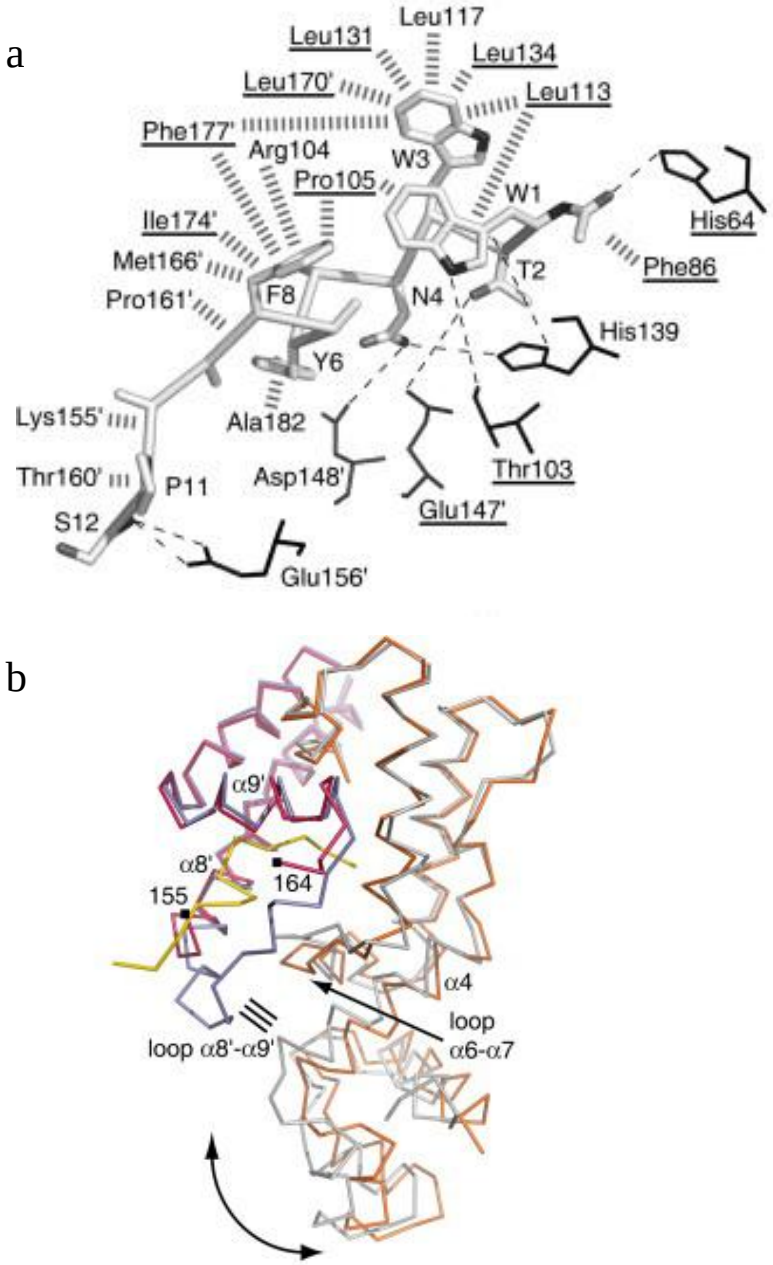

Figure 1.10 The structure of the Tip-TetR complex (a) Interactions occurring between TetR and Tip. Ionic interactions (dashed line) and van der Waals interactions (parallel lines) are marked. Tip residues are labeled with the single-letter code; the three-letter code is used for TetR residues. (b) Superposition of Tip-induced TetR and uninduced TetR. Tip-induced TetR is shown in gray and red, while uninduced TetR in yollow and brown. The parallel lines hight intersubunit interactions that are unique to the Tip-TetR complex. (Luckner *et al*., 2007).

The binding of Tip to TetR also repositions its DNA-binding domain in analogy to that of Tc by the pendulum-like motion of helix α4 (Section 1.10.1.3). However, the

repositioning of helix α4 is achieved by direct intersubunit interaction between loop α8' to α9' and the beginning of helix α4, different to the conformational changes of the C-terminal turn of α6 and the N-terminal turn of α7 in the induction by Tc (Luckner *et al*., 2007) (Figure 1.10b).

1.10.2 QacR

The *Staphylococcus aureus* QacR binds to an operator DNA and negatively regulates *qacA* transcription (Grkovic *et al.*, 1998). QacA is a multidrug transporter and confers resistance to a broad range of antimicrobial agents. QacR is a member of the TetR family but shows a very low overall sequence identity (13.8%) with TetR (Sequence alignment was performed by SIM at Expasy). In contrast to ten helices of TetR, QacR is 23 residues shorter than TetR (these 23 residues are corresponding to α10 in TetR), and has nine helices: α1(3-18), α2(25-32), α3(36-42), α4(46-71), α5(75-88), α6(96-108), α7(110-136), α8(145-162) and α9(168-185), which play different functions during the binding of DNA and drugs (Schumacher *et al.*, 2001 and 2002).

1.10.2.1 DNA binding mechanism of QacR

The first three helices act as a three-helix bundle DNA-binding domain (helix-turn-helix motif) and helices 4 through 9 are responsible for drug binding and dimerization (Schumacher *et al.*, 2002). Although QacR and TetR are members of TetR family, they bind DNA in different modes. The QacR/dsDNA complex consists of two QacR dimers and one 28 bp operator, and the two dimers are found to dock onto the two successive major grooves of the cognate DNA (Figure 1.11) (Schumacher *et al.*, 2002).

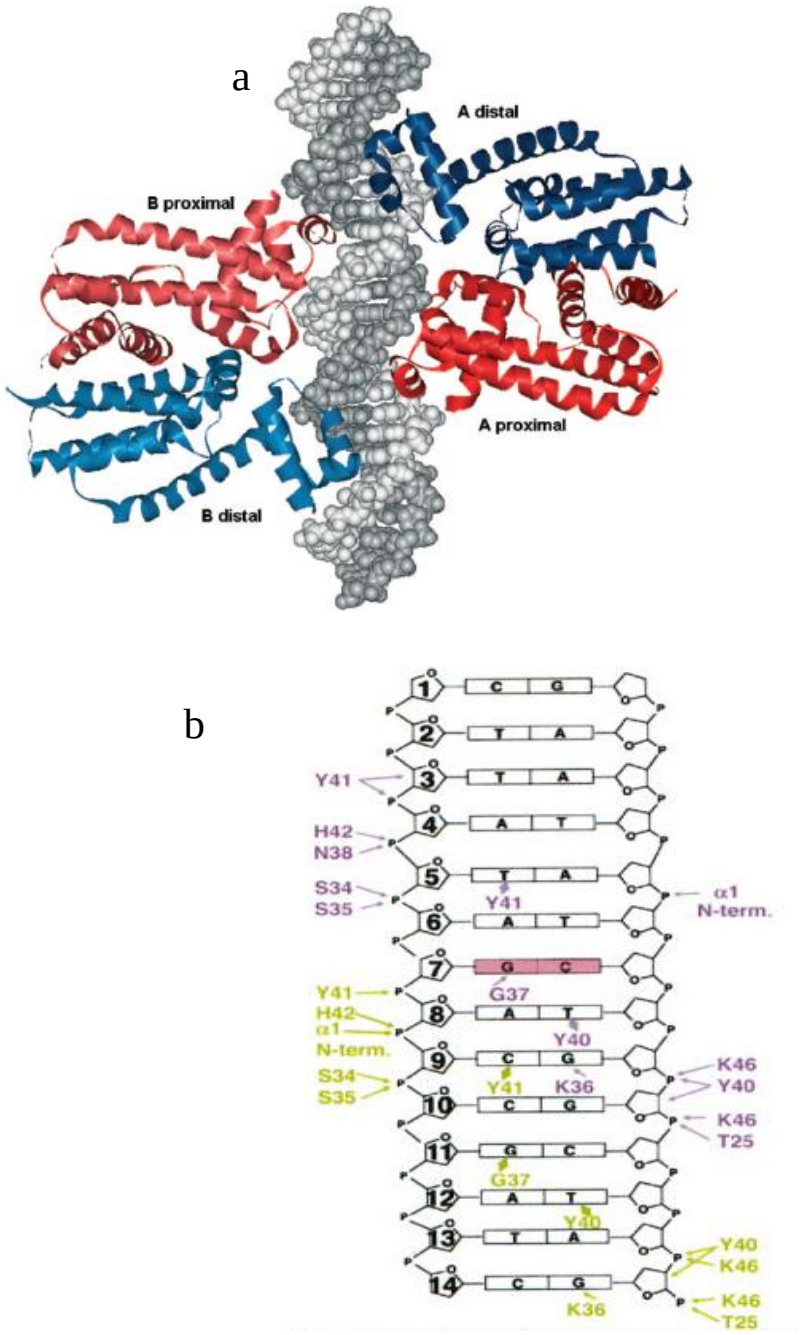

Figure 1.11 Structure of QacR bound to its cognate DNA duplex. (a) Ribbon representation of the two QacR homodimers bound to target DNA. The monomers of each dimer are designated as distal (blue) or proximal (red). (b) Schematic showing QacR-DNA half-site contacts. The yellow and purple subunits are from different dimers. Nucleotide G7 is the location of the *qacA* transcription start site and this GC pair is shaded in purple (Grkovic *et al.*, 2001; Schumacher *et al*., 2002).

QacR binds its operator cooperatively, which is mediated by unwinding of the DNA. The unwinding of operator DNA bound by QacR is reflected by two characteristics. The DNA oligonucleotide bound by QacR has a twist of 32.1° and 11.2 bp per turn

pitch, which are 34.3° and 10.5 bp per turn in canonical B-DNA. In addition, the center-to-center distances between the recognition helices of each QacR dimer (the distance between amide nitrogens of Gly37) expands to 37 Å, in contrast to 34 Å for proteins that bind the consecutive major grooves of B-DNA. It is proposed that the binding of the first dimer, an energetically costly step, locks the 28 bp operator DNA into an unwound conformation, which is ready for the binding of the second QacR dimer (Schumacher *et al*., 2002).

The two monomers of QacR dimer at each side of the operator DNA recognize different bases and have been taken as distal and proximal monomers, depending on the distances to the dyad (Schumacher *et al*., 2002) (Figure 1.11a). Proximal monomers make base-sepecific interactions with the 28 bp operator, while distal monomers make several base and phosphate contacts (Figure 1.11) (Schumacher *et al*., 2002). Two QacR dimers have 16 base and 44 phosphate contacts with the 28 bp dsDNA. The central six base pairs provide the appropriate spacing for QacR and the addition to or removal of two base pairs from this 6 bp spacer abolishes QacR binding. In addition, the four base pairs at the two ends of the DNA duplex could function as over hang bases for the crystal package, as there is no contact between them and QacR.

1.10.2.2 Drug binding sites of QacR

QacR binds different monovalent and bivalent cationic lipophilic compounds, which are also substrates of the efflux pump QacA (Murray *et al.*, 2004; Schumacher *et al.*, 2001; Schumacher *et al.*, 2004). According to the structures of QacR bound to six drugs individually (Rhodamine 6G, R6G; Ethidium Et; Dequalinium, Dq; Crystal Violet, CV; Malachite Green, MG; and Berberine, Be), the drug-binding pocket of QacR was divided into two sites: the Et pocket and the R6G pocket (Schumacher *et al.*, 2001).

Drug binding induces a coil-to-helix transition of residues Thr89-Tyr93 that results in the expulsion of Tyr92 and Tyr93 from the hydrophobic interior of the protein to the solvent and the formation of the expansive drug-binding pocket, which plays an important function in drug binding (Schumacher *et al.*, 2001). Tyr92 and Tyr93 also stabilize the drug-binding pocket of QacR when no drugs are bound to QacR

(Schumacher *et al.*, 2001). These functions of Tyr92 and Tyr93 are in agreement with the concept that aromatic residues are critical in drug binding and essential for the construction of the drug binding pocket (Schumacher *et al*., 2004).

The coil-to-helix transition triggered by drug binding elongates the C-terminus of α5 by a turn, and thus relocates α6 and its tethered DNA-binding domain. Similar to TetR drug induction, upon drug binding, α4 has a pendulum motion and the center-to-center distance of the recognition helices increases to 48 Å from 37 Å of the DNA-bound form.

The positively charged ethyl ammonium groups of drugs are neutralized by negatively charged glutamate: Glu90 in the QacR-R6G complex; Glu57, Glu58 and Glu120 in the QacR-Dq complex; Glu90 and Glu120 in QacR-CV complex and QacR-MG complex; Glu57 and Glu58 in QacR-Be complex; and Glu120 in QacR-Et complex serves this function (Schumacher *et al.*, 2001).

In the crystals of the QacR-diamidine complex, a novel drug charge neutralization was proposed (Murray *et al.*, 2004): not only is glutamate involved in the neutralization of positively charged drugs, but the oxygen atoms of a carbonyl and side chain also serve the same function (Murray *et al.*, 2004).

In the ternary QacR-Pf-Et compex, Pf is still bound in the R6G pocket, and protein-drug contacts are similar to those in QacR-Pf binary complex, with stacking against the aromatic side chains of residue Trp61 and Tyr103, hydrogen bonding with Gln96 and Thr89, and ionic interactions with the side chains of residues Glu57 and Glu58. However, Et slides into a new position, close to the binding sites of QacR-Et binary complex. In the new location, Et interacts with Pf through van der Waals interactions. Figure 1.12 shows the structures of QacR-Pf-Et and QacR-R6G.

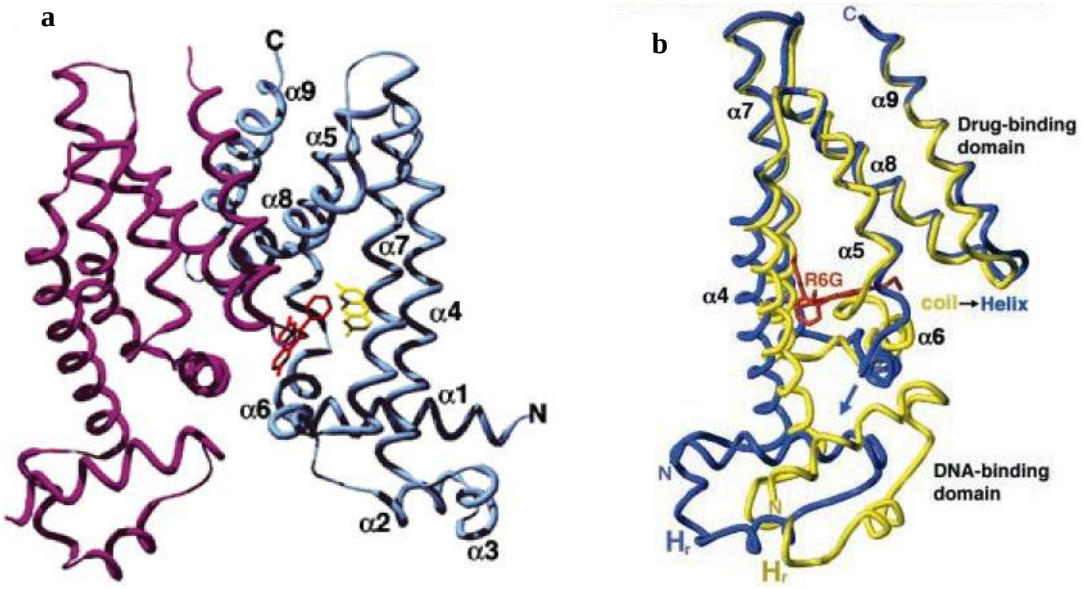

Figure 1.12 The structure of the ternary QacR-pf-Et and QacR-R6G
a: A ribbon diagram of the QacR-pf-Et ternary complex; the nine helices are numbered and the pf and Et are presented as yellow and red sticks respectively. b: The superimposition of QacR DNA-bound conformation (yellow) and QacR drug binding conformation (blue). The coil-to-helix transition is illustrated. The location of rhodamine 6G (red) in the drug-bound structure is indicated, as are α4 to α9, the HTH recognition helix (H_r), and the N and C termini of the protein (Schumacher and Brennan, 2002; Schumacher *et al.*, 2002).

In the TetR family repressors of multidrug efflux pumps, besides the structures of QacR and TetR, the crystal structures of AcrR, CmeR and SmeT have been determined. Furthermore, EthR is a well studied regulator in the TetR family and its structure provides a new clue to develop drugs for the therapy of tuberculosis (Frenois *et al.*, 2004); MtrR is a regulator of the MtrCDE efflux pump in *Neisseria gonorrhoeae*, but could act as a global regulator (Folster and Shafer, 2005; Folster *et al.*, 2007).

1.10.3 AcrR

AcrR, the transcriptional repressor of AcrAB multidrug efflux pump in *E. coli*, has a three helix DNA-binding domain, and a diverse C-terminal drug binding domain, forming the ligand-binding sites (Li *et al.*, 2007). The AcrAB pump, which belongs to the RND efflux pump family, acts with the outer membrane protein TolC, to assemble a tripartite drug efflux pump and thus expels antibacterial agents (Touze *et al.*, 2004). The α2 and α3 of AcrR form a typical helix-turn-helix motif, which is well conserved among members of the TetR family (Li *et al.*, 2007). The

dimerization of AcrR involes mainly α8 and α9. The C-terminal drug binding domain of AcrR forms a large internal cavity for drug binding located at the center of the binding pocket (Li *et al.*, 2007). Figure 1.13 shows a ribbon diagram of the AcrR homodimer.

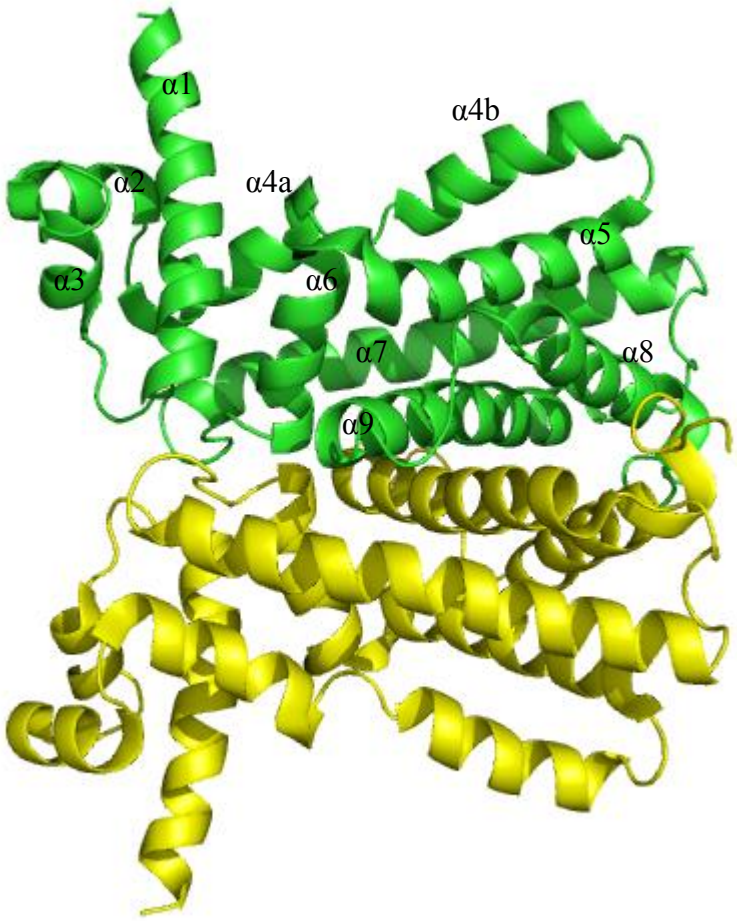

Figure 1.13 Ribbon diagram of the AcrR homodimer (PDB code: 2QOP) generated by crystallographic symmetry (Li *et al.*, 2007). The nine helices are numbered. The figure was prepared using PyMOL (DeLano, 2002).

1.10.4 CmeR

CmeR, a member of TetR transcriptional regulator family, represses the transcriptional expression of CmeABC in *Campylobacter jejuni* (Cagliero *et al.*, 2007; Gu *et al.*, 2007; Lin *et al.*, 2005a and b). The CmeABC pump, a RND type efflux pump, functions in the export of antimicrobial agents and bile resistance, which is essential for Campylobacter colonization of the animal intestinal tract (Lin *et al.*, 2005a and b). The cyrstal structure of CmeR revealed that the N-terminal DNA

binding domain and C-terminal drug binding domain are similar to other members of the TetR family (Gu *et al.*, 2007). However, one of the critical characteristics for DNA binding in this family, the HTH motif usually consists of α2 and α3, is found to be deficient in α3 in CmeR (Gu *et al.*, 2007). The expected α3 region forms a random coil, rather than an helix (Gu *et al.*, 2007). The C-terminal drug binding domain of CmeR encompasses helices 4-10 (Gu *et al.*, 2007). Helices 6, 8, 9 and 10 contribute to the dimerization of CmeR. There is a large tunnel-like cavity in the C-terminal drug binding domain of CmeR, which is about 20 Å long (Gu *et al.*, 2007). Figure 1.14 shows a ribbon diagram of the AcrR homodimer.

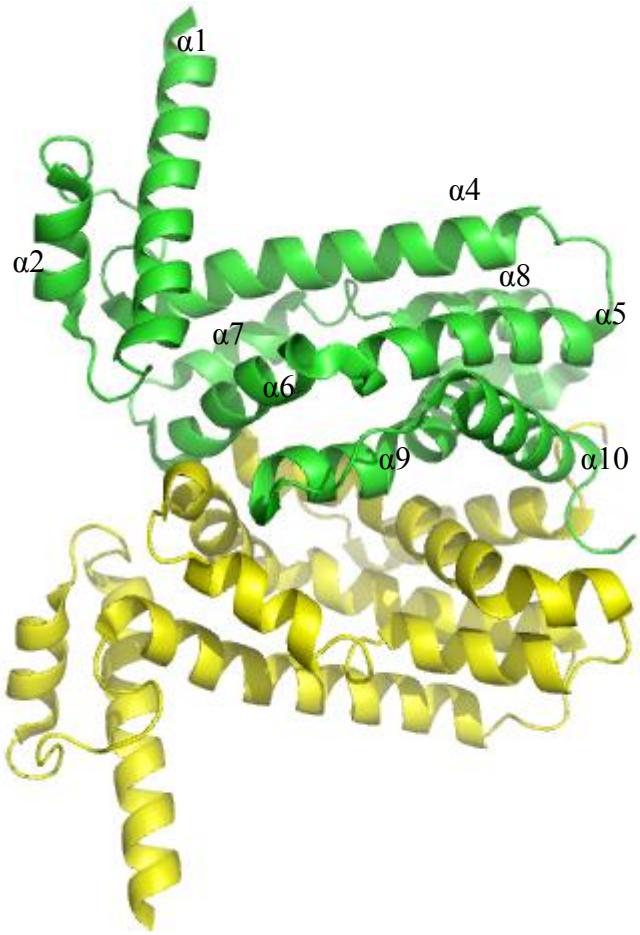

Figure 1.14 Ribbon diagram of the CmeR dimer (PDB code: 2QCO) generated by crystallographic symmetry (Gu *et al.*, 2007). The ten helices are numbered. The figure was prepared using PyMOL (DeLano, 2002).

1.10.5 SmeT

SmeT is the repressor of the multidrug efflux pump SmeDEF in *Stenotrophomonas maltophilia* (Hernandez *et al.*, 2009; Sanchez *et al.*, 2002). Similar to other members of TetR family, SmeT has an N-terminal HTH DNA binding domain and a C-terminal dimerization and ligand binding domain (Hernandez *et al*., 2009). The two subunits of the SmeT dimer in the crystal are different (Hernandez *et al*., 2009). There is an unknown ligand occupying the ligand pocket in subunit A but no putative ligand for subunit B (Hernandez *et al*., 2009). The binding of the unknown ligand in subunit A stabilizes its N-terminus, whereas in subunit B the DNA-binding domain is almost completely disordered (Hernandez *et al*., 2009). Figure 1.15 shows a ribbon diagram of the SmeT dimer. DNase I footpringting assays show SmeT binds to a 28-bp pseudopalindromic region, which overlap the promoters of *smeT* and *smeDEF*, indicating the function of SmeT in simultaneously regulating *smeT* and *smeDEF* transcription (Hernandez *et al*., 2009).

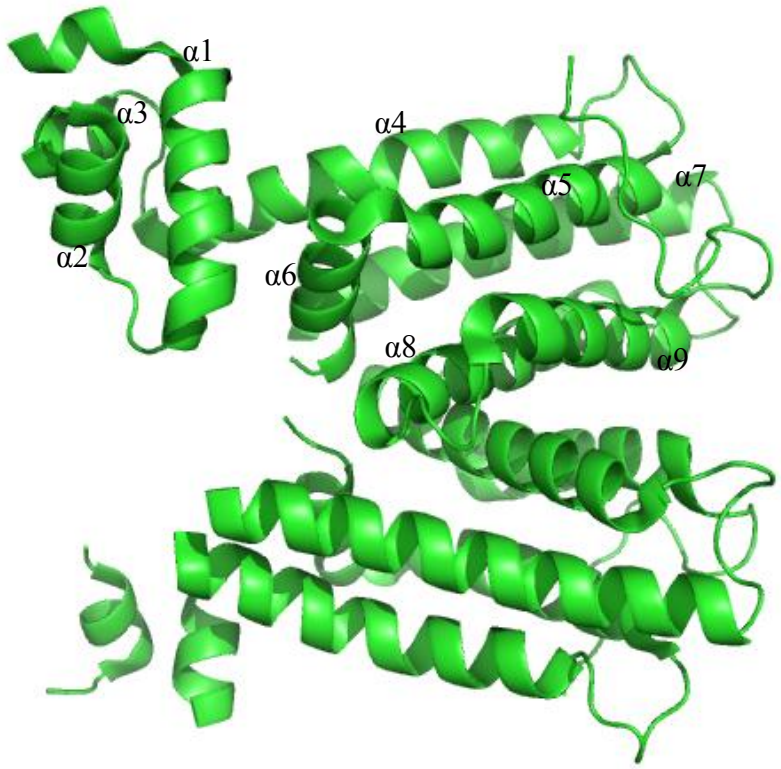

Figure 1.15 Ribbon diagram of the SmeT dimer (Hernandez *et al*., 2009; PDB code: 2W53). The nine helices are numbered. The figure was prepared using PyMOL (DeLano, 2002).

1.10.6 EthR

EthR, a member of TetR transcriptional regulator family, binds the *ethA* promoter region and inhibits the expression of *ethA* in *Mycobacterium tuberculosis* (Dover *et al.*, 2004). EthA is a FAD-containing enzyme that catalyses two steps in the activation of ethionamide (ETH), which is the major antituberculosis drug, and thus the repression of *ethA* expression by EthR affects the therapy of tuberculosis by ETH (Dover *et al.*, 2004; Engohang-Ndong *et al.*, 2004; Frenois *et al.*, 2004). EthR exists as a dimer in solution. Unlike QacR, TetR and other regulators in TetR family, EthR binds cooperatively to the 55bp operator as octamer (Engohang-Ndong *et al.*, 2004). The octamerization of EthR requires the presence of the operator DNA (Engohang-Ndong *et al.*, 2004). The crystal structure of EthR expressed and purified from *E. coli* shows EthR is unexpectedly bound with hexadecyl octanoate (HexOc), which provides a new clue to develop drugs for the therapy of tuberculosis (Frenois *et al.*, 2004). Figure 1.16 shows a ribbon diagram of the EthR dimer.

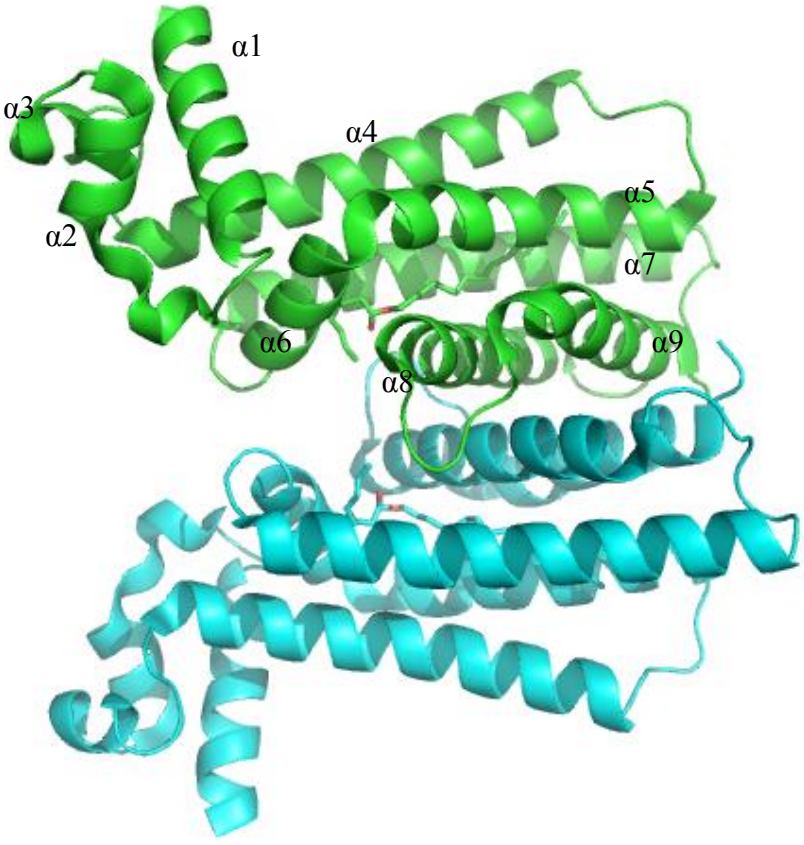

Figure 1.16 Ribbon drawing of the EthR dimer (Frenois *et al.*, 2004; PDB code: 1U9N) generated by crystallographic symmetry. The nine helices are numbered and the ligand HexOc is shown in a stick model. The figure was prepared using PyMOL (DeLano, 2002).

1.10.7 MtrR

MtrR, a member of TetR transcriptional regulator family, represses the transcription of the MtrCDE efflux pump in *Neisseria gonorrhoeae* (Hoffmann *et al.*, 2005; Lucas *et al.*, 1997). The MtrCDE pump, an RND family export pump, confers the resistance of gonococci to several antimicrobials. The intergenic sequence between the *mtrR* and *mtrC* genes is bound by MtrR was confirmed by gel mobility shift and DNase I footprint assays (Lucas *et al.*, 1997). In the DNA binding assay, higher salt (200 mM NaCl) affected the binding affinity, compared with lower salt 100 mM NaCl (Hoffmann *et al.*, 2005).

MtrR also indirectly regulates the *farAB*-encoded efflux pump, which confers *N. gonorrhoeae* resistance to fatty acids (Lee *et al.*, 2003). The FarAB pump consists of the FarA membrane fusion protein and the FarB cytoplasmic membrane transporter protein, which act with the outer membrane channel MtrE (Lee *et al.*, 2003). The FarAB pump is regulated by the transcriptional repressor FarR, a member of the MarR family (Lee *et al.*, 2003). MtrR was reported to bind to the FarR promoter and repress the expression of FarR (Lee *et al.*, 2003). Thus, MtrR would positively regulate the FarAB pump through inhibition of the expression of the FarR repressor (Lee *et al.*, 2003).

In addition, MtrR was reported to regulate *ponA*, which encodes penicillin-binding protein 1, the *pilMNOPQ* operon, which encodes components of the type IV pilus secretion system, and *mtrF*, which encodes MtrF that acts in conjunction with the MtrCDE pump to confer gonococci resistance to certain drugs, indicating MtrR could act as a global regulator (Folster and Shafer, 2005; Folster *et al.*, 2007).

1.10.8 VceR

Vibrio cholerae is the causative agent of cholera, which is characterized by a severe watery diarrhea, through colonizing the small intestine and producing cholera toxin (Faruque *et al*., 1998). Multi-drug resistant *V. cholerae*, which were first reported in 1980, has been a leading cause of cholera outbreak in the following two decades (Glass *et al*., 1980; Faruque *et al*., 1998). The active expulsion of antibiotics, catalyzed by efflux pumps, is an important resistance mechanism in *V. cholera*

(Faruque and Nair, 2008) and consequently the study of these efflux pumps and their regulation could contribute to combating multidrug resistant *V. cholerae*.

The *vceCAB* genes of *V. cholerae* encode a tripartite drug pump that consists of an inner-membrane protein (IMP) VceB, a periplasmic membrane fusion protein (MFP) VceA and an outer-membrane protein (OMP) VceC, which is a homologue of the EmrAB/TolC multiple-drug resistance transporter found in *E. coli* (Borges-Walmsley *et al.*, 2005; Federici *et al.*, 2005; Woolley *et al.*, 2005).

VceR, which belongs to the TetR family of transcriptional regulators, negatively regulates the *vceCAB* operon, by binding to a 28 bp inverted-repeat within the *vceR-vceC* intergenic region (Borges-Walmsley *et al.*, 2003). Using size-exclusion chromatography (SEC) and dynamic light-scattering, VceR was shown to bind the *vce* promoter as a tetramer. It is thought that VceR binds the *vce* promoter in a similar manner to the binding of QacR to the *qacA* promoter, which binds a pair of homodimers to a 28 bp inverted repeat within the promoter.

The role of the *vceR-vceABC* operon in conferring antibiotic resistance has been established from several studies. Knocking-out *vceR* in *V. cholerae* increased the resistance of the cells to CCCP (carbonyl cyanide m-chlorophenyl-hydrazone) and deoxycholate (Alatoom, *et al*., 2007). On the other hand, a plasmid carrying the *vceAB* genes conferred resistance to CCCP, DOC, rifampicin, erythromycin, nalidixic acid and chloramphenicol in *E. coli*. The repressor VceR also binds CCCP that is the substrate of the *VceCAB* pump, inducing its release from the *vceCAB* promoter and allowing expression of the VceABC pump (Borges-Walmsley *et al.*, 2005). Figure 1.17 shows the the *vceCAB* operon and the *vceR-vceC* intergenic region.

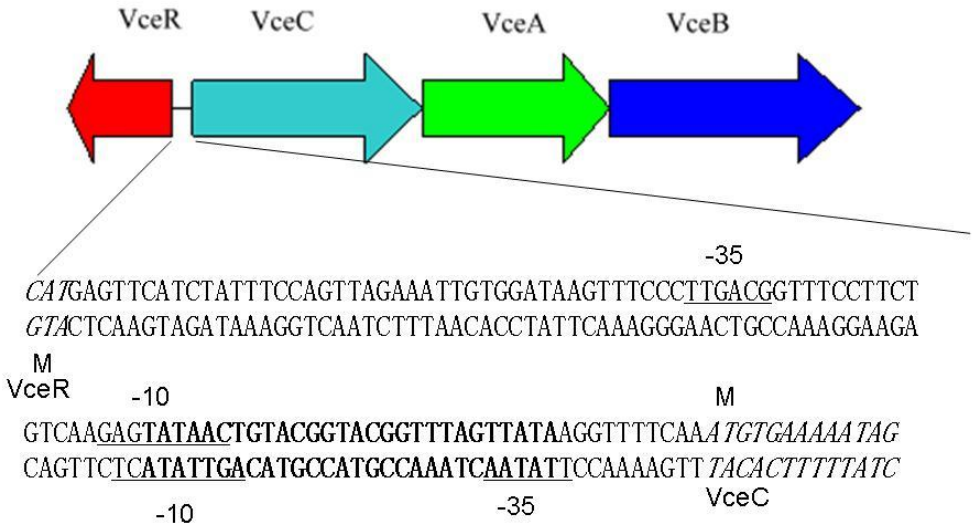

Figure 1.17 Schematic representation of the *vceRCAB* operon. The 120 bp intergenic region is shown with *vceR* and *vceC* genes italicised. Predicted transcription signals are underlined and marker -35 and -10 with transcript initiation. 28bp duplex bound by VceR is indicated in bold (Borges-Walmsley *et al.*, 2005).

Our knowledge of the repression and derepression mechanism of TetR family has largely come from structural studies of individual proteins and the TetR/DNA and QacR/DNA complexes (described in Section 1.20). In spite of the overall structural similarity of TetR and QacR, the induction mechanism and the mode of DNA recognition varies greatly in the TetR family. TetR binds as a dimer to a 15 bp inverted repeat, whilst QacR binds as a pair of dimers to a 28 bp inverted repeat. There would be value in determining the structure for additional members of the family, to obtain further information on the mechanism of operation. VceR shares low sequence identity with QacR (17.7%) and TetR (14.7%); and consequently the determination of the VceR/DNA complex structure could expand our understanding of the transcriptional repression mechanism in the TetR family. In addition, this complex structure could also reveal the drug binding domain of VceR, which has not been determined. Furthermore, the structure of the VceR/DNA complex might be useful in the design of small molecules to switch-off the expression of the drug pump as a strategy in combating drug resistance in *V. cholerae*.

Chapter 2 Material and Method

2.1 Computational methods

Adobe Photoshop was used for modification of diagrams/illustrations. Vector NTI Advance 10 (Invitrogen), was used for the analysis, and design of oligonucleotides and for the construction of alignments of DNA and protein sequences for comparison.

The National Center for Biotechnology Information (NCBI, http://www.ncbi.nlm.nih.gov) was used as a resource for structural, functional and comparative analysis of genomes. The Protein Data Bank (http://www.RCSB.org) was used as a resource for protein structures.

A secondary structure prediction server, NPS@ HNN secondary structure prediction (http://npsa-pbil.ibcp.fr/cgi-bin/npsa_automat.pl?page=/NPSA/npsa_hnn.html) was used to predict the secondary structure.

2.2 Media, antibiotics and reagents

General chemical reagents such as salts with analytical purity grade were acquired from Sigma (UK). Detergents n-dodecyl-β-D maltoside (DDM) and 10% Triton were purchased from Calbiochem. Reductive reagents Tris hydroxypropyl phosphine (THP) was purchased from Novagen and dithiothreitol (DTT) was purchased from Melford.

2.2.1 Bacterial medium

The following bacterial media were prepared as described below and sterilised by autoclaving at 121^{o}C for 20 min.

Luria-Bertani medium	
Tryptone (Oxoid)	10 g
Yeast extract (Oxoid)	5 g
NaCl	10 g
dH_2O	To 1000 ml

Luria-Bertani agar	
LB medium	1 litre
Agar (Merck)	15 g

2X YT broth	
Tryptone (Oxoid)	16 g
Yeast extract (Oxoid)	10 g
NaCl	5 g
dH_2O	To 1000 ml

SOC medium	
Tryptone (Oxoid)	4 g
Yeast extract (Oxoid)	1 g
NaCl	0.117 g
KCl	0.0373 g
dH_2O	To 200 ml
After autoclaving, the following components were added:	
1 M $MgCl_2 \cdot 6H_2O$	2 ml
1 M $MgSO_4$	2 ml

2.2.2 Antibiotics

Antibiotic stock solutions			
Antibiotic	**Concentration**	**Working concentration**	**Manufacturer**
Carbenicillin disodium	100 mg/ml in dH_2O	100 µg/ml	Melford laboratories
All antibiotics were filter-sterilised, with a 0.2 µm filter, and stored in 1 ml aliquots at -20^{o}C			

2.2.3 Reagents

Reagent stock solutions		
Reagent	**Concentration**	**Manufacturer**
IPTG	1 M in dH_2O	Melford laboratories
IPTG	200 mg/ml in dH_2O	Melford laboratories
X-gal	20 mg/ml in N,N' – dimethylformamide (DMF)	Melford laboratories
L-arabinose	20% in dH_2O	Sigma
IPTG and L-arabinose were filter-sterilised, with a 0.2 µm filter, and stored in 1 ml aliquots at -20^{o}C		

2.3 Bacterial strains and plasmids

The bacterial strains and plasmids used in this study are listed in Table 2.1. Cryogenic stocks were generated by mixing 800 µl of an overnight culture with 200 µl of sterile 80% glycerol in sterile 2 ml cryogenic vials and stored at -80^{o}C. Samples were retrieved by scraping and streaking a small amount of the frozen stock, with a sterile loop, and then plating onto solid growth medium for incubation at 37^{o}C overnight.

Table 2.1 Bacterial strains

Strain	Key feature(s)	Source/Reference
E. coli NovaBlue (DE3)	*end*A1 *hsd*R17 ($r_{k12-}m_{k12+}$) *sup*E44 *thi*-1 *rec*A1 *gyr*A96 *rel*A1 *lac* [F'*pro*A^{+}B^{+} *lac*I^{q}ZΔM15::Tn*10*(tet^{R})]; for cloning, plasmid preps	Novagen
E. coli BL21 (DE3)	F^{-} *omp*T *hsd*S_B($r_B^{-}m_B$) *gal dcm met* (DE3); for protein expression	Novagen
XL10-Gold	Tet^{R} Δ (*mcr*A) 183 Δ (*mcr*CB-*hsd*SMR-*mrr*) 173 *end*A1 *sup*E44 *thi*-1 *rec*A1 *gyr*A96 *rel*A1 *lac* Hte [F' *pro*AB *lacl*^{q}ZΔM15 Tn10 (Tet^{R}) Amy Cam^{R}]^{a}	Stratagene

Table 2.2 Plasmids

Plasmid	Key feature(s)	Source/Reference
pGEM-T easy	Ampicillin resistance; for TA cloning	Promega
pET21a(+)	N-terminal T7-tag and C-terminal His_6-tag; For protein expression; Ampicillin resistance.	Novagen
VceR-His_6-pET21a(+)	*vceR* ligated with pET21a(+) using *Nde*I and *Xho*I restriction endonuclease sites with C-terminal His_6-Tag, for VceR-His_6 expression	Borges-Walmsley *et al.*, 2005

2.4 Cloning genes to pGEM-T easy vector

2.4.1 DNA amplification by PCR (polymerase chain reaction)

PCR (polymerase chain reaction) was used to amplify genes from genomic DNA or to certify inserted genes in plasmids used in this study. Primers (Table 2.2) were designed with restriction endonuclease sites and synthesized by Invitrogen. Usually, primers were reconstituted in distilled water to a concentration of 50 pmol/µl.

Table 2.3 The oligonucleotides for PCR used in this study.

Oligonucleotide	Sequence
*Nde*I- *hpa1* Forward*	**CAT ATG** AAT TCT TTG AAC ACA CAA TTC GGC
*Xho*I- *hpa1* Reverse	**CTC GAG** CTG CAT CGA TCC GCT GTC GTT CG
*Nde*I-163-414-*hpa1* Forward	**CAT ATG** CAG CCG AAC AAA AAT GCT GAG GAA GG
*Xho*I-1-158-*hpa1* Reverse	**CTC GAG** GCC ATT CTC CTT CCC GGC CTG CTG

*Note: Sequences in bold indicate restriction endonuclease sites.

PCR was carried out according to the manual of the product providers. A typical reaction composition is given below.

Master mix Component	Volume (µl)	Final concentration
10xPCR Buffer (containing 15 mM $MgCl_2$)	5	1x
dNTP mix (10 mM of each)	1.5	200 µM of each dNTP
F primer	1	50 pmol/µl
R primer	1	50 pmol/µl
HotStar Taq DNA Polymerase (Qiagen)	0.5	2.5 units/reaction
Distilled water (dH_2O)	41	-
Colony DNA	Variable	≤1 µg/reaction
Total volume	**50**	-

A thermal cycler (Eppendorf mastercycler gradient) was programmed for the PCR reaction as follows:

Cycle	Temperature	Time
Activation of HotStar Taq DNA polymerase	95^{o}C	15 min
Denaturation	94^{o}C	1 min
Annealing	58^{o}C	1 min
Extension	72^{o}C	50 sec
Number of cycles	34	
Final extension	72^{o}C	10 min
Hold	4^{o}C	Indefinitely

The amplified DNA samples were stored at -20^{o}C.

2.4.2 Gel electrophoresis

For positive identification of the DNA, 10 µl of the amplified DNA plus 2 µl of a 6x DNA loading buffer, together with a 1 kb DNA marker (Invitrogen) was loaded on a 1% agarose gel containing ethidium bromide and electrophoresed for 35 minutes at 120 volts. The gel was visualised on a UV transilluminator (Gene, BioImaging System, Syngene) equipped with a camera to capture an image of the gel.

DNA Gels

1% Agarose gel	
Laboratory grade agarose	1%
Ethidium bromide	0.004%
1x TAE buffer	100%

DNA Buffers

1x TAE buffer	
Tris-HCl	4.84 g
Acetic acid	1.142 ml
0.5 mM EDTA	2 ml
dH_2O	To 1000 ml

6x DNA loading buffer	
Bromophenol blue	0.025 g
100% Glycerol	3 ml
dH_2O	7 ml

2.4.3 Gel extraction of DNA

The DNA was excised from the gel and 300 µl buffer QG from QIA quick gel extraction kit was mixed with it. After 10 min incubation at 50^{o}C, dissolved gel was loaded to QIAquick spin column and centrifuged for 1 min. 0.75 ml buffer PE was added to QIAquick column and centrifuged for 1 min. Finally, 50 µl buffer EB (10 mM Tris-Cl, pH 8.5) was used to elute the DNA from the column.

2.4.4 Ligation into pGEM-T easy vector (Promega)

All components were added, in order as listed below, to a 0.5 ml microcentrifuge tube. The ligation mixture was stored at 4^{o}C overnight (for maximum transformants) for transformation the following day.

Component	Volume (μl)
2 x Ligation buffer	7.5
pGEM-T easy vector	1.5
PCR product	4.5
T_4 DNA ligase	1.5
	Total Volume = 15 μl

2.4.5 Preparation of chemically competent *E. coli*

A chemical method for the induction of competence in *E. coli* is described as follows. A single colony was used to inoculate 5ml liquid LB medium and incubated overnight at 37^{o}C with 225 rpm rotary agitation. A millilitre of overnight culture was used to inoculate 50 ml of pre-warmed liquid LB medium in a 250 ml flask. The cells were incubated at 37^{o}C with 220 rpm rotary agitation until an optical density at 600 nm (OD_{600}) of 0.5 was reached. The culture was cooled on ice for 5 minutes, harvested at 4,000×*g* for 5 minutes at 4^{o}C and the supernatant carefully discarded. The bacterial cell pellet was resuspended in 30 ml cold, sterile TFB1 buffer and the suspension kept on ice for 90 minutes. The cells were harvested at 4,000×*g* for 5 minutes at 4^{o}C, and the supernatant discarded. The cell pellet was resuspended in 2 ml cold TFB2 buffer and kept on ice for a further 45 minutes. Following this incubation period, competent cells were harvested furthermore as described previously and resuspended in 2 ml cold TFB2 buffer. Aliquots of 50 μl were transferred to 1.5 ml microcentrifuge tubes and flash frozen in a dry ice/ ethanol bath. Chemically competent cells were stored at -80^{o}C.

TFB1 buffer – 100 mM rubidium chloride, 50 mM manganese chloride, 30 mM potassium acetate, 10 mM calcium chloride, 15% glycerol, pH 5.8.
TFB2 buffer- 10 mM MOPS, 10 mM rubidium chloride, 75 mM calcium chloride, 15% glycerol, pH 6.8.

2.4.6 *E. coli* strain NovaBlue transformation

4 μl of the pGEM-T-gene ligation mixture was added to a 50 μl aliquot of NovaBlue competent cells (prepared as section 2.4.5). The transformation mixture was incubated on ice for 30 min, a 42^{o}C water bath for 50 seconds, and incubated on ice

for a further 2 min. 250 µl of SOC medium was added to the cells and incubated at 37^{o}C with 250 rpm shaking for 90 minutes. 100 µl of cells were spread onto LB/carbenicillin (LB/Carb) medium (plus IPTG [200 mg/ml] and X-gal [20 mg/ml]) and incubated at 37^{o}C overnight.

Plates from the above transformation were stored at 4^{o}C for 3 hours to allow the blue/white colour in the colonies to fully develop. Blue colonies contained active galactosidase whilst the white colonies were thought to harbour the recombinant plasmids. Nine white colonies were re-streaked onto an LB/Carb plate and incubated at 37^{o}C overnight for PCR identification of positive recombinants the following day.

2.4.7 Purification of plasmid DNA [pGEM-T-easy-gene]

Overnight cultures of *E. coli* NovaBlue were harvested by centrifugation (Jouan CR3i centrifuge) at 4,000 rpm for 10 minutes at 4^{o}C. Plasmid DNA was prepared as instructed in the QIA prep® Miniprep Handbook. The eluted plasmid DNA was stored on ice or at -20^{o}C.

10 µl of the pGEM-T-easy-gene plasmid was sent to the University of Durham (DBS Genomics) to ensure sequence integrity. The sequencing result was aligned with the original gene sequence using Vector NTI Advance 10 (Invitrogen).

2.5 Subcloning of desired genes into pET21a(+) for protein expression

2.5.1 Restriction enzymes digestion of pGEM-T-easy-gene and pET21a (+)

The components, as listed below, were added to a 0.5 ml microcentrifuge tube and incubated at 37^{o}C for 3 hours. The restriction endonuclease I and restriction endonuclease II (Promega) were then heat inactivated at 65^{o}C for 15 min. The samples were stored at 4^{o}C.

pGEM-T-easy-gene	
Component	**Volume (μl)**
dH_2O	4.5
10x Buffer	5
Bovine serum albumin (BSA)	0.5
Restriction endonuclease I	2.5
Restriction endonuclease II	2.5
pGEM-T-gene	25
Total volume = 40 μl	

pET21a(+)	
Component	**Volume (μl)**
dH_2O	15.5
10x Buffer	5
BSA	0.5
Restriction endonuclease I	2
Restriction endonuclease II	2
pET21a(+)	25
Total volume = 50 μl	

2.5.2 Identification and purification of DNA and linear pET21a (+)

Performed as described in sections 2.4.2 and 2.4.3.

2.5.3 Ligation of pET21a(+) and desired DNA

All components were added, in order as listed below, to a 0.5 ml microcentrifuge tube. The ligation mixture was stored at 4^oC for 12 hours (for maximum transformants) for transformation the following day.

Component	**Volume (μl)**
10 x Ligation buffer	1.5
pGEM-T easy vector	1.5
PCR product	4.5
T_4 DNA ligase	1.5
Total volume = 15 μl	

2.5.4 *E. coli* strain NovaBlue transformation with pET21a (+)-gene

Performed as described in section 2.4.6 with the following changes:

5 µl of pET21a(+)-gene was added to 150 µl of competent *E. coli* NovaBlue cells (prepared as section 2.4.5); 1 ml of SOC medium was added following heat shock and no blue/white selection was required.

2.5.5 Analysis of putative pET21a (+)-gene colonies by PCR

Performed as described in sections 2.4.1 and 2.4.2

2.6 Site directed mutagenesis

The *in vitro* site directed mutagenesis experiments in this thesis were performed as described using the QuikChange site-directed and multi site-directed mutagenesis system (Stratgene). The mutagenic primers were designed to incorporate a centrally located desired point mutation in specific amino acid sites (Table 2.4).

Table 2.4 Mutagenic oligonucleotides used for site directed mutagenesis.

Oligonucleotide	**Sequence**
hpa1-C47S Forward*	5'-CTGGACCAGTTGCTG**AGC**CAGCTCATCCAGGCCCTG -3'
hpa1-C47S Reverse	5'-CAGGGCCTGGATGAGCTG**GCT**CAGCAACTGGTCCAG-3'
vceR-C148S-Forward	5'-TGTGGTTCATTGAAAGAG**AGC**GATCCTTGGATCGCC-3'
vceR-C148S-Reverse	5'GGCGATCCAAGGATC**GCT**CTCTTTCAATGAACCACA-3'
vceR-C138S-C142S-Forward	5'-GTCGCTACATTA**CGT**CGCAAATTG**AAA**GCGGTTCAC TGAAAGAG-3'
vceR-C138S-C142S-Reverse	5'-CTCTTTCAGTGAACCGC**TTT**CAATTTGCG**ACG**TAATGT AGCGAC-3'
vceR-H156R-Forward	5'-CCTTGGATCGCCGCCATG**AGA**TTCAAAGCGTTGCTA-3'
vceR-H156R-Reverse	5'-TAGCAACGCTTTGAA**TCT**CATGGCGGCGATCCAAGG-3'

*Note: Sequences in bold indicate mutation sites.

Mutant strand synthesis reaction was carried out according to the manual of the kit. A typical reaction composition is given below.

Master mix Component	**Volume (μl)**	**Final concentration**
10x reaction buffer	5	1x
dNTP mix	1	200 μM of each dNTP
F primer	1.25	2.5 ng/μl
R primer	1.25	2.5 ng/μl
PfuTurbo DNA polymerase	1	0.05 units/reaction
dsDNA template	X μl (5-50 ng)	-
Distilled water (dH_2O)	Variable	
Total volume	**50**	-

A thermal cycler (Eppendorf mastercycler gradient) was programmed for mutagenesis reaction as follows:

Cycles	**Temperature**	**Time**
1	95 ^oC	30 seconds
12-18	95^oC	30 seconds
	55^oC	1 min
	68^oC	1 minute/kb of plasmid length

Dpn I restriction enzyme was added to the mutagenesis reaction to digest the parental supercoiled dsDNA. The *Dpn* I-treated DNA was transformed into XL1-Blue supercompetent cells for site-directed mutagenesis or XL1-Gold supercompetent cells for multi site-directed mutagenesis. The desired mutation was sequenced for the final usage.

2.7 Protein expression, purification and visualization

2.7.1 Expression of cloned genes in *E. coli* BL21 (DE3)

A single colony from a freshly streaked plate was picked and inoculated into 100 ml LB broth containing the appropriate antibiotic(s) in a 250 ml flask. The cells were grown in an orbital shaker at 37 ^oC, 220 r.p.m. overnight. One litre of prewarmed 2×YT broth (with antibiotic) in a 2 litre baffled flask was inoculated with 5 ml of the overnight cultures. 6 litres of the cells were grown in an orbital shaker at 37 ^oC, 220

rpm. The cells were induced at mid log phase (approx. A_{600}=0.5-0.6) with 0.5 mM IPTG. The temperature was dropped to 30 ^{o}C and the growth was continued with shaking at 200 rpm for 5 hours for soluble proteins or overnight for membrane proteins. The cells were harvested by centrifugation and stored as a frozen pellet at -80 ^{o}C or continued with purification.

2.7.2 Purification of His_6-tagged proteins by Ni-NTA affinity chromatography

Frozen cell pellets were typically resuspended with 200 ml buffer (25 mM Tris-HCl, 300 mM NaCl, pH7.5). One EDTA-free protease inhibitor tablet (Roche Molecular Biochemicals) was added to inhibit protease activity. The cells were lysed by mechanical disruption in a constant cell disruption system (Constant Systems Ltd) at a pressure of 27 kpsi two times. The cell lysate was fractionated into membrane and soluble components by high-speed ultracentrifugation at 43,000 rpm for 1 hour (Beckman Ti-50 rotor). For membrane proteins, the membrane pellet was resuspended in buffer A and solubilised using 1% DDM. High-speed ultracentrifugation at 43,000 rpm for 1 hour (Beckman Ti-50 rotor) was performed to separate the soluble protein-detergent complex from membrane lipids.
The soluble component or soluble protein-detergent complex was, after high-speed ultracentriguation, loaded onto a Ni-NTA column (GE Healthcare). The column was washed with buffer containing 50 mM imidazole to remove contaminant proteins. The protein was eluted with buffer containing 500 mM imidazole.

2.7.3 Purification of recombinant proteins by gel filtration chromatography

Gel filtration chromatography was used to purify the proteins, initially purified by Ni-NTA affinity chromatography. HiLoad 16/60 Superdex 200 prep grade and HiLoad 16/60 Superdex 75 prep grade columns (GE Healthcare) were used in this study.

The column was equilibrated with three column volumes of dH_2O at 30 cm/h (1 ml/min), and three column volumes of buffer at 30 cm/h (1 ml/min). The sample was injected into the column and eluted with 1.5 column volumes of buffer. Purified samples were collected on a fraction collector (GE Healthcare) for SDS-PAGE

analysis. After purification, the column was washed with 2 column volumes of dH_2O and then with 2 column volumes of 20% ethanol for long storage. All buffers and water were filter-sterilised, with a 0.22 µm filter, and degassed.

2.7.4 Ion-exchange chromatography

Ion-exchange chromatography was also used to purify proteins and performed using an AKTA purifier (GE Healthcare). A HiTrap Q HP 5 ml column (GE Healthcare) was utilised in this study. The column was stored with 20% ethanol. Firstly, the column was rinsed with five column volumes of dH_2O and then equilibrated with start buffer to change sample buffer into start buffer. Samples were pumped into the column and washed with 3 column volumes of start buffer. A NaCl gradient elution was performed with start buffer and elution buffer. Proteins were monitored by UV 280 nm and collected for SDS-PAGE analysis. All buffers and water were filter-sterilised, with a 0.22 µm filter and degassed.

2.7.5 SDS-PAGE

All SDS-PAGE (Sodium dodecyl sulfate polyacrylamide gel electrophoresis) experiments were performed using the NuPAGE® Novex pre-cast gels and XCell *SureLock* mini-cell (Invitrogen). The NuPAGE® LDS sample buffer (4X) (Invitrogen) was used for preparing samples for denaturing gel electrophoresis with the NuPAGE® gels. SeeBlue® prestained standard (Invitrogen) was added to the gels to indicate the molecular weight of the proteins. After electrophoresis in MES buffer, gels were incubated in a staining container containing 100 ml of staining buffer and gently shaken for 30 minutes at room temperature on an orbital shaker. The stain buffer was decanted and the gel was rinsed once with deionized water. Then the gel was placed in a staining container with 100 ml of destain buffer and gently shaken at room temperature on an orbital shaker until the desired background was achieved.

MES buffer	
MES	9.76 g
Tris-base	6.05 g
SDS	1 g
EDTA	0.29 g
Add dH_2O to	1 L

Protein staining solutions

Coomassie blue stain buffer	
Acetic acid	33%
Methanol	33%
dH_2O	33%
Coomassie brilliant blue R-250	0.1%

Destain buffer	
Acetic acid	10%
Methanol	10%
dH_2O	80%

2.7.6 Western blotting

Transfer buffer		Wash buffer	
Glycine	2.9 g	1 M Tris-HCl, pH 7.5	10 ml
Tris base	5.8 g	5 M NaCl	30 ml
Methanol	200 ml	Tween 20	1 ml
SDS	0.37 g	dH_2O to	1000 ml
dH_2O to	1000 ml		

The protein samples were run with SeeBlue markers (Invitrogen) on NuPAGE® Novex pre-cast gels. The gel was soaked in the methanol-transfer buffer for 15-30 minutes. The blotting cassette holds the gel and the PVDF membrane (Polyvinylidene fluoride, 0.2 µm, Bio-Rad) while a nylon sponge and of the Whatman chromatography paper (3 MM) on both sides provide complete contact within the gel sandwich. The cassette was inserted vertically into the blotting tank.

The blotting tank was topped up with transfer buffer and electroblotted at 170 mA for 1 hour. Then the blotted gel was stained with coomassie blue stain buffer (section 2.7.5) to confirm successful transfer. The PVDF membrane was transferred to 25 ml of blocking buffer (wash buffer plus 3% BSA) in a square Petri dish, the PVDF

membrane was blocked for 90 minutes at room temperature with gentle agitation, and then was stored at a 4 ^{o}C overnight. The PVDF membrane was washed three times with wash buffer at room temperature, for five minutes each time. The PVDF membrane was incubated with the first antibody (1:3000 dilution) in 25 ml fresh blocking buffer (wash buffer plus 0.5% BSA and 8 µl monoclonal antipolyhistidine antibody, Sigma) at room temperature for 1 hour. The PVDF membrane was rinsed in wash buffer three times, for 10 minutes each time, and incubated with the second antibody (1:3000 dilution) in 25 ml fresh blocking buffer (wash buffer plus 0.5% BSA and 8 µl goat anti-mouse IgG- AP [Alkaline Phosphatase conjugate], Sigma) at room temperature for 1 hour. The PVDF membrane was rinsed in wash buffer three times, for 10 minutes each time. The PVDF membrane was transferred to a sheet of cling film and 2 ml substrate (Immun-Star™ AP substrate, Bio-Rad) was added. The PVDF membrane was wrapped with the film and left on bench for 5 minutes. The PVDF membrane was transferred to between two sheets of plastic and taped around four sides in an autorad cassette. In the dark room, a sheet of X-ray film was inserted and left for 1 minute. An XO Graph imaging systems compact X4 film processor was used to fix and develop the X-ray film.

2.7.7 Protein dialysis

Slide-A-Lyzer® dialysis cassettes (Pierce) were utilized in this study to change the protein buffer. Different cassette volumes of 0.1-0.5 ml, 0.5-3 ml or 3-15 ml were selected according to the sample volume. The protein samples were collected with a syringe and injected into hydrated cassettes, which were left in dialysis buffer with gentle stirring at 4 ^{o}C for 2 hours. This procedure was repeated after changing the buffer once. Finally, the samples were recovered from the dialysis cassettes.

2.7.8 Protein concentrating

The protein samples were concentrated using the disposable ultrafiltration device Vivaspin concentrators (Viva Science). The samples were pipetted into the concentrators and spun (Beckman, Avanti™ J-20 XP, JA-10 rotator, 15 ml tube adaptor) at low speed (usually 3000 g). Then the samples were recovered from the

bottom of the concentrating pocket with a pipette, once the desired concentration was achieved.

2.7.9 Protein concentration determination

The BCA™ protein assay kit (Pierce) was used to determine the protein concentration. The 'test tube procedure' for this kit (Pierce) was adopted according to the instructions, which was summarized as follows. 0.1 ml of each standard and unknown protein sample and 2 ml of the reagent were added to each tube and mixed well. The tubes were incubated at 37°C for 30 minutes and the 562 nm absorbance measurement of each standard and protein sample was performed. A standard curve was prepared by plotting the average 562 nm measurement for each BSA standard vs. its concentration in μg/ml. Then the standard curve was used to determine the protein concentration of each unknown sample.

2.8 Analytical gel filtration chromatography

The analytical gel filtration chromatography column Superdex 200 PC 3.2/30 column (GE Healthcare), and high and low molecular weight gel filtration kits (GE Healthcare) were used to determine the molecular weight of proteins. To determine the M_r of proteins, a calibration curve was constructed (Microsoft Office Excel 2003), using bovine serum albumin (62.9 kDa), ovalbumin (46.7 kDa), catalase (213 kDa) and adolase (182 kDa) as standards for a plot of the log of the M_r of the standards *versus* K_{av}. The K_{av} values of the protein standards were calculated as follows:

$K_{av} = (V_e - V_o)/(V_t - V_o)$,
V_e = elution volume for the protein
V_o = column void volume
= elution volume for blue dextran 200 (From high and low molecular weight gel filtration kits)
V_t = total bed volume, 2.4 ml for Superdex 200 PC 3.2/30 column

After purification, the column was rinsed with 3 column volumes of dH_2O and then with 2 column volumes of 20% ethanol for long storage. All buffers and water were filter-sterilised, with a 0.22 µm filter, and degassed.

2.9 Peptide synthesis

Peptide 1 (H_2N-ISEKQLDQLLCQLIQALL-COOH) and peptide 2 (H_2N-ASPLTQMLMNIVGEILQAQ-COOH) used in the study were synthesized, purified and analysed by mass spectrometry by Genscript corporation (China).

2.10 Transmission electron microscopy

Transmission electron microscopy (TEM) was used to study fibril formation. Purified protein or synthesized peptides were diluted to a low concentration; 10 µl samples were loaded onto a carbon-coated grid (Agar scientific, UK) and incubated at RT for 1 min. After drying, 1% uranyl acetate solution was used as stain, and loaded to carbon-coated grids for 30 sec. Prepared samples were displayed under a transmission electron microscope (TEM-H7600, Hitachi) at an accelerating voltage of 100 keV.

2.11 Circular dichroism spectroscopy

Circular dichroism (CD) spectroscopy was used to study the secondary structure of proteins. The spectra of prepared samples and the corresponding blanks were recorded between 190 and 260 nm on a spectropolarimerter (Jasco J-810) using quartz cells with a 2 mm path length at 27 ^{o}C. After the subtraction of the appropriate blank, binominal smoothing was carried out within the Jasco Spectra analysis program. The resulted spectra were analysized by program Selcon3 via Dichroweb (Whitmore and Wallace, 2004). The protein reference set (dataset 4 from Dichroweb) was used.

2.12 Congo red (CR) binding and chemical cross-linking

A Congo red binding assay was carried out as described previously (Oh *et al*., 2007). Congo red (Sigma) was prepared in a buffer of 20 mM Tris-HCl pH 8.5, and 20 mM NaCl. Absorbance spectra in the region between 400 and 700 nm were recorded for a 100 µM Hpa1 fibril and 20 µM Congo red mixture and for Cong red using a Jasco V-550 spectrophotometer.

Proteins were dialyzed against the cross-linking buffer (20 mM Na_2HPO_4, pH 8.5, 100 mM NaCl) for 6 h. DSP (Dithiobis [succinimidyl propionate]) or EGS (EthylGlycol bis [succinimidyl succinate]) was added to a final concentration of 0.5 mM. After incubation for 30 min at 37 ^oC, 1 M Tris pH 8.5 was added to a concentration of 20 mM to stop the reaction. The effect of Ca^{2+} and *E. coli* liposomes on the oligomerization of Hpa1-His_6 was tested, in the presence of 2 mM $CaCl_2$ and 0.1 mg *E. coli* liposome, respectively and together. The samples were loaded onto a 12% SDS-PAGE gel and stained with coomassie brilliant blue.

2.13 Liposome disruption assay

1 ml of 10mg/ml *E. coli* polar lipid extract (Avanti®, component: phosphatidylethanolamine, phosphatidylglycerol, cariolipin) was dried under the steam of nitrogen to form a thin film. The dried lipid was rehydrated in 1ml of MES buffers (20 mM MES, 20 mM NaCl, pH 6.5) by vortexing. The lipid was heated to 50 ^oC for complete rehydration. The lipid was further passed through the extruder (Avanti®) with 400 nM polycarbonate membrane filter (Whatman®) at 50 ^oC to produce unilamellar vesicles. 100 µM purified soluble Hpa1, N-terminal truncated Hpa1 and peptide 2 were incubated with 500 µl 5 mg/ml liposomes, respectively, for 6 h at room temperature.

For membrane protein reconstitution into membrane, 10% Triton X-100 (Calbiochem®) was added to the liposome with a final molarity of 1.5 mM. 100 µl of 0.4 mg/ml protein sample was added to 1 ml of 2 mg/ml destabilized liposomes to give a final lipid to protein ratio of 50:1 (w/w) and incubated with shaking at 25 ^oC for 15 min. 40 mg Bio-bead SM-2 absorbent (Bio-Rad®) was added to the protein and liposome solution and shook at 25 ^oC for 30 min. The solution was removed and transferred to a 1.5 ml micro-centrifuge tube containing 80 mg Bio-beads and

incubated at 25 ^{o}C for 60 min with shaking. This step was repeated and incubated at 4 ^{o}C overnight. The proteoliposomes were pelleted by centrifugation at 43000 rpm at 4 ^{o}C for 1 hour and resuspended in 0.5 ml phosphate buffer.

Liposomes disrupted by soluble Hpa1, N-terminal truncated Hpa1 and peptide 2, and the resuspended proteoliposome of Hpa1 and C47S were displayed under a transmission electron microscope (TEM-H7600, Hitachi) at an accelerating voltage of 100 keV by the negative staining with a 1% uranyl acetate solution on carbon-coated grids (Agar scientific, UK) (section 2.10).

For sucrose gradient centrifugation, a 500 µL sample (protein-liposome mixture) was mixed with 3.5 ml 70% (w/w) sucrose and subsequently by overlaying 6.5 ml 55% and 2 ml 10% sucrose solution onto the protein-liposme-sucrose mixture. Centrifugation was performed in a Beckman SW55 rotor at 32 000 r.p.m. for 16 h at 4 ^{o}C. Fractions were collected from the 70% and 10% sucrose layers and aliquots were separated by 12.5% SDS/PAGE. The bands were detected with coomassie blue staining.

2.14 Protein crystallization

The purified, concentrated and quantified protein was submitted to crystallization trials. The screening was performed by Screenmaker from Innovadyne. 85 µl crystallization buffer was transferred into a reservoir and two sitting drops were set up, 200 nl complex plus 100 nl precipitating solution and 100 nl complex plus 100 nl precipitating solution.

Kits used for VceR/dsDNA co-crystallization screen:
(1) Cryo I & II from Emerald
(2) JCSG-plus from Molecular Dimensions
(3) The PEGs suite from Qiagen
(4) Clear strategy screen from Molecular Dimensions

For crystallization condition optimization, the experiments were set up manually according to the hanging drop vapour diffusion method, using a 24 well plate (24

crystallization buffer wells) with 24 crystallization supports (six protein wells for holding crystallization buffers and proteins), or the sitting drop vapour diffusion method using a 24 well plate with bridge and cover slip. All the buffers and precipitants were purchased from Sigma, Fluka and Hampton. An additive kit was obtained from Hampton.

Crystallization solution (0.5ml) was pipetted to the bottom of the plate well. 1µl protein sample and 2 µl crystallization buffer were mixed and the mixture was transferred to the protein well of the crystallization support. The crystallization support was screwed into place above the well from which the crystallization buffer was taken. The crystallization trial plates were incubated at 20 ^{o}C, 18 ^{o}C or 4 ^{o}C (Cooled Incubators, Rumed®) for two weeks or longer, depending on the growth rate of crystals. Stereo zoom microscope (Leica, MZ125) was used in this study to observe the crystals. A digital camera (Nikon, coolpix 4500) was used to take photos of crystals.

An additive screen kit (Hampton Research) was utilized to search for additives to improve the crystal shape and/or quality. This kit evaluates the factors of multivalent cations, salts, amino acids, dissociating agents, linkers, polyamines, chaotropes, co-factors, reducing agents, polymers, chelating agent, carbohydrates, polyols, non-detergents, amphiphiles, detergents, osmolyte and organic agents (Hampton Research). 0.3 µl of each additive from the kit was added into the crystallization drops, consisting of 1 µl protein and dsDNA mixture and 2 µl reservoir buffer. After incubation at 4 ^{o}C for 4 weeks, all 96 drops with 96 additives from the kit were compared to find out the suitable additives for the VceR/dsDNA crystallization.

2.14.1 Selenomethionine protein over-expression and purification for phasing

The medium (medium base, nutrient mix, methionine solution and selenomethinone solution) was purchased from Molecular Dimensions and prepared as described in the instructions from the product.

One colony was inoculated into a 100 ml culture containing L-methionine and incubated at 37 ^{o}C in a shaking incubator over night. The cells were pelleted, washed

3 times in 100 ml of sterile water and resuspended in 1 ml sterile water. 1 L medium containing selenomethionine was inoculated with 1 ml resuspended cells and incubated with shaking until an OD600 of 0.5 was reached. IPTG was added and cells were incubated for a further 6 hours before cell harvest. The purification of selenomethionine VceR follows the protocol in section 2.7.2 and 2.7.3.

2.14.2 Oligonucleotides for VceR co-crystallization

The oligonucleotides (Table 2.5) used for VceR co-crystallization were ordered from MWG and Sigma. Oligonucleotides were delivered as lyophilised powder. Before use, oligonucleotides were dissolved in annealing buffer (10 mM Tris-HCl, pH 7.5, 50 mM NaCl, 1 mM EDTA, 10 mM $MgCl_2$). Complementary pairs of oligonucleotides were mixed, heated to 95 ^{o}C for 5 minutes and cooled down overnight in a heat block. All oligonucleotide duplexes used in VceR co-crystallization are summarized in Table 2.5.

Table 2.5 The oligonucleotide duplexes used for VceR/DNA co-crystallization

P56	5'–AGTATAACTGTACGGTACGGTTTAGTTATA–3' 3'–TCATATTGACATGCCATGCCAAATCAATAT-5'
P56-1	5'- TATAACTAAACGGTACGGTTTAGTTATA-3' 3'- ATATTGATTTGCCATGCCAAATCAATAT-5'
P56-2	5'- TATAACTGTACGGTACGGTACAGTTATA-3' 3'- ATATTGACATGCCATGCCATGTCAATAT–5'
P56-3	5'- TATAACTGTACGGTACGGTTTAGTTATA-3' 3'- ATATTGACATGCCATGCCAAATCAATAT-3'
P56-4	5'- AGTATAACTGTACGGTACGGTTTAGTTATAA-3' 3'- TTCATATTGACATGCCATGCCAAATCAATAT -5'
P56-5	5'- AGTATAACTGTACGGTACGGTTTAGTTATA -3' 3'-TTCATATTGACATGCCATGCCAAATCAATATT–5'
P56-6	5'- TATAACTGTACGGTACGGTTTAGTTATAAG-3' 3'-CTATATTGACATGCCATGCCAAATCAATAT -5'
P56-7	5'-AGTATAACTGTACGGTACGGTTTAGTTATAA -3' 3' TCATATTGACATGCCATGCCAAATCAATATT-5'
P56-28	5'- TATAACTAAACGGTACCGTTTAGTTATA-3' 3'- ATATTGATTTGCCATGGCAAATCAATAT-5'
P56-27	5'-TATAACTAAACGGTACCGTTTAGTTAT-3' 3'-ATATTGATTTGCCATGGCAAATCAATA-5'
P56-26	5'-ATAACTAAACGGTACCGTTTAGTTAT-3' 3'-TATTGATTTGCCATGGCAAATCAATA-5'
P56-24	5'-TAACTAAACGGTACCGTTTAGTTA-3' 3'-ATTGATTTGCCATGGCAAATCAAT-5'

2.14.3 Data collection

At the beginning of this work, crystals were tested at the laboratory of Professor Rick Lewis, Institute for Cell and Molecular Bioscience, the Medical School, Newcastle University, using the in-house diffractometer. All data sets were collected by Dr. Santina Russo (SLS) and Dr. Ehmke Pohl (Department of Chemistry, Durham University) at the Swiss Light Source (SLS) using X10SA (Pohl *et al*., 2006), X06D and X06SA; and Diamond Light Source using beamline 102.

Several cryo-solutions (glycerol, saturated salt, PEG and sucrose) were screened to find the appropriate cryo-condition for crystal freezing in liquid nitrogen. To optimize the soaking time, seconds to minutes or sequential transfer of crystals from

low concentration of cryo-solution to a high one were tested. The rotation method was used in data collection. A typical data collection had a 1-2 second exposure time at the SLS or 10 second at the DLS, 0.5° or 1° per frame which is dependent on the survival of crystals from radiation damage.

2.14.4 Data processing

The HKL2000 program package (Denzo, Scala) (Otwinowski and Minor, 1997) was used to process data. The site definition containing the X-ray detector and camera information (the detector name, the goniostat misalignment, direction of rotation, detector orientation, X-ray beam properties) was obtained from the DLS or SLS beamlines. The autoindexing in Denzo was used to find the lattice system and refine the unit cell, beam and detector parameters. Each set of frames was integrated to obtain the intensity of each reflection. The diffraction intensities were scaled and symmetry-related reflections were merged to a reduced dataset of unique reflections.

The fluorescence emission spectrum of the Se-VceR/DNA crystals or VceR/Br-DNA crystals was used to show the presence of Se or Br in the crystals and to select the wavelengths for MAD experiments. The f' and f'' values for Se and Br at peak, inflection point and high energy remote were obtained from http://skuld.bmsc.washington.edu/scatter/AS_form.html. Xprep (Bruker AXS, Madison, USA) was used to assess the anomalous signal of MAD (Multiple-wavelength anomalous diffraction) or SAD (single-wavelength anomalous diffraction) data sets, and produce the input files for substructure determination. ShelxD (Schneider and Sheldrick, 2002; Sheldrick, 2008) was used to locate the heavy atom positions. The resolution cutoff in ShelxD is determined by finding where the correlation coefficient between the signed anomalous differences for two wavelengths falls below about 30%. Several parameters in ShelxD were used to indicate a good solution, most importantly CC (correlation coefficient between observed and calculated *E* values). Usually, for MAD, a CC of 40 to 50% indicates a good solution.

2.14.5 Structure solution

The .sca files from HKL2000 were converted to mtz format in ccp4i by Scalepack2mtz, which were merged into one .mtz file by CAD in ccp4i (Collaborative computational project, Number4, 1994) with columns containing native and three wavelength data sets. The phases were calculated by Sharp (Bricogne *et al*., 2003), using 12 Se atom sites from ShelxD as input. The high energy remote data set was used as the reference for scaling, and the default setting of Sharp was used. Solvent flattening (54%) was run after phasing by DM (Cowtan, 1994). Coot (Emsley and Cowtan, 2004) was used to show the electron density map and build the model manually. To obtain an initial poly-alanine model, the combination of position of Se sites within the secondary structures (predicted by the HNN secondary structure prediction method; Whitmore and Wallace, 2004) was used to fit each helix into the obtained electron density manually. For the DNA model, 11 bp duplex of B-DNA from Coot was manually modelled on the electron density map.

Chapter 3 Amyloid fibril formation by Hpa1 from *Xanthomonas oryzae* pv. oryzicola

In this chapter, I report the construction, expression and purification of Hpa1, harpin of *X. oryzae* pv. oryzicola. The ability of Hpa1 to form fibrils at different pHs was tested. The secondary structure transition during the fibril assembly was studied by CD spectroscopy. The fibrils formed by Hpa1 were found to damage the liposomes made from extracted *E. coli* lipids.

3.1 Cloning, overexpression and purification of Hpa1

3.1.1 Cloning of *hpa1* into pET21a expression vector

The *hpa1* gene was amplified by PCR from genomic DNA of the *X. oryzae* pv. oryzicola (provided by Prof. Gongyou Chen, Nanjing agricultural University, Nanjing, China) with primers *Nde*I-*hpa1* Forward and *Xho*I-*hpa1* Reverse (Table 2.2). Figure 3.1 shows the successful amplification of *hpa1* (Lane 1), which is consistent with the predicted size of 414 bp. The amplified *hpa1* gene was extracted and purified from the agarose gel and ligated into the commercial T-A propagation vector, pGEM-T Easy (section 2.4.3 and 2.4.4). The ligation mixture was transformed into chemically competent *E. coli* NovaBlue (section 2.4.6). Positively identified recombinant clones were used in the following expression vector sub-cloning procedure. Plasmid DNA purified from recombinant colonies was digested with *Nde*I and *Xho*I to confirm the presence of inserted DNA. After restriction enzyme digestion of the vector with *Nde*I and *Xho*I, the resulting *hpa1* fragment was ligated into pET21a generating a construct to express the *hpa1* gene with a C-terminal His_6-tag. The successful constructs were sequenced and aligned with sequence of *hpa1* from Genebank (ACCESSION AY875714 REGION: 940-1353). The construct was transformed into *E. coli* strain BL21(DE3) for Hpa1 overexpression.

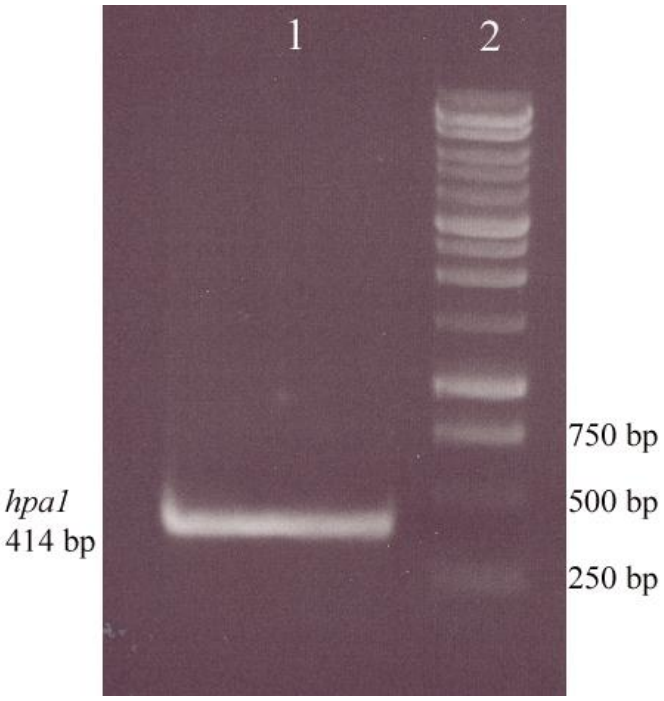

Figure 3.1 PCR amplification of *hpa1* gene from *X. oryzae* pv. oryzicola strain RS105. Lane 2 shows a molecular weight (M_r) marker. Lanes 1 shows individual PCR amplification reaction.

3.1.2 Over-expression of Hpa1-His_6

Expression of Hpa1 from pET21a results in a fusion of the Hpa1 protein to a His_6-tag at the C-terminus and is referred to as Hpa1-His_6.

Bacterial cultures were prepared as described in section 2.2.1, incorporating 100 μg/ml carbenicillin. The protocols for protein expression were as described in section 2.7. At an OD_{600} of 0.5-0.6, Hpa1- His_6 from BL21(DE3) was induced with 0.5 mM IPTG at 25^{o}C with 120 rpm rotary agitation for 5 hours. The cells were harvested, resuspended in buffer A (20 mM Tris-HCl pH 8.5, 300 mM NaCl, 10% glycerol) and stored at -80 ^{o}C for purification.

3.1.3 Purification of soluble and membrane faction Hpa1-His_6

The soluble fraction containing Hpa1-His_6 from 4 litres of culture was obtained by differential centrifugation (Section 2.7.2) and purified by metal affinity chromatography using Ni^{2+} agarose (Section 2.7.2). The packed column was washed with 10 ml of 20 mM Tris-HCl pH 8.5, 300 mM NaCl, 10% glycerol, 50 mM

imidazole. Hpa1-His_6 was eluted from the column using buffer A containing 500 mM imidazole.

Hpa1-His_6 purified by metal affinity chromatography was loaded onto a gel filtration column, Hiload 16/60 superdex 200 column (GE Healthcare), pre-equilibrated with 3 column volumes (CV) of buffer A, for further purification. Figure 3.2 shows the elution chromatogram of Hpa1-His_6 on a Hiload 16/60 superdex 200 prep grade size-exclusion column. Hpa1 has low UV280 absorbance as there is no Trp or Tyr in Hpa1 (Calculated extinction coefficient of Hpa1 at 280 nm is 120 $cm^{-1}M^{-1}$). Figure 3.3 shows the efficiency of expression and purification of Hpa1-His_6 on an SDS-PAGE gel. The calculated molecular weight of Hpa1-His_6 is 14682.45 Da (Vector NTI, Invitrogen). However, on the SDS-PAGE gel, the migration of the protein band (Figure 3.3A 2-3 lanes) is around the 20 kDa standard of the SeeBlue protein marker (Lane 1). His_6-tag western blot (Section 2.7.6) was used to confirm the identification of expressed Hpa1-His_6. Figure 3.3B lanes 1 and 2 show the western blot signals of Hpa1-His_6 and its dimer.

The mass spectrum was determined by positive ion electrospray with up-front liquid chromatographic separation in the Chemistry Department, Durham University. The experimental mass is 14698 Da and the theoretical mass is 14682 Da calculated from the empirical formula of Hpa1-His_6. The difference of 16 Da between these two values might originate from the gaining of protons in ionization, or other adduct (possibly an oxygen atom), or the average mass from isotopic C^{12} and C^{13}.

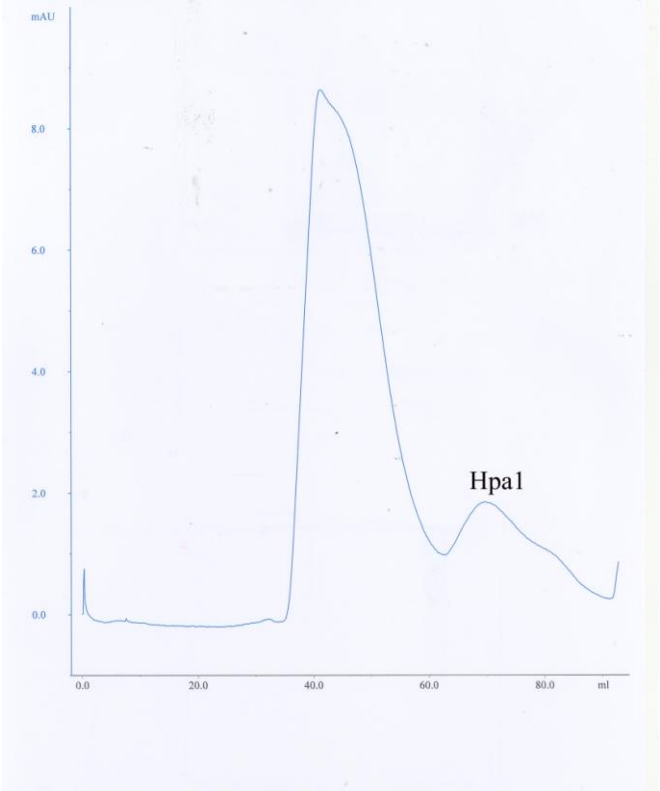

Figure 3.2 The elution chromatography profile of Hpa1-His$_6$ from a Hiload 16/60 superdex 200 gel filtration column. The peak with about 40 ml elution volume is the aggregation of Hpa1 or the contaminated proteins.

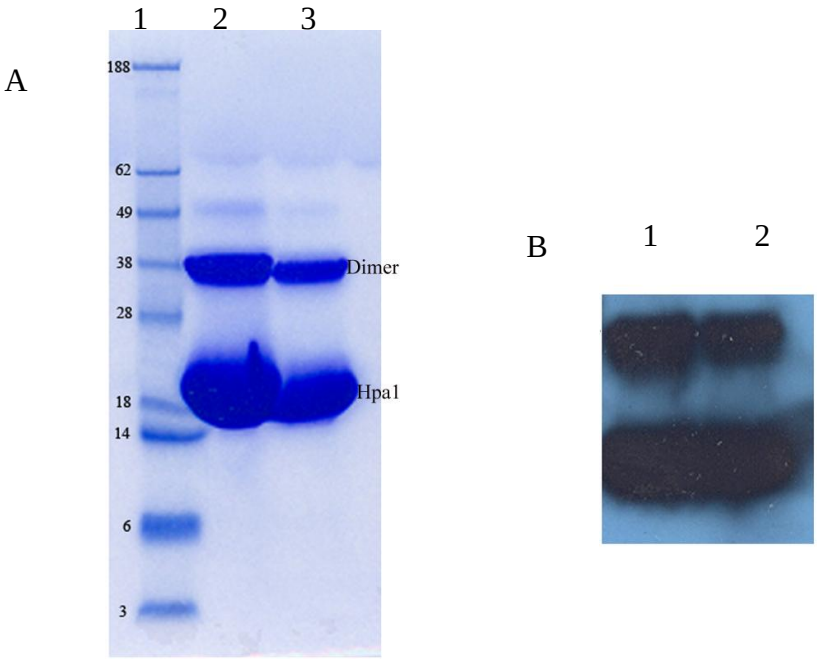

Figure 3.3 SDS-PAGE and Western blot of Hpa1-His$_6$. (A) Lane 1 is a protein molecular weight (M_r) marker. Lanes 2 and 3 show Hpa1-His$_6$ on a SDS-PAGE gel. (B) Lanes 1 and 2 are the signals for Hpa1- His$_6$ in a western blot corresponding to lane 2 and 3 in A, respectively.

To test whether over-expressed Hpa1-His_6 could bind to *E. coli* membrane in, the membrane pellet was resuspended in buffer A (20 mM Tris-HCl, pH 8.5, 300 mM NaCl, 10% glycerol) and solubilised using 1% DDM (n-dodecyl-β-D maltoside, Calbiochem, UK). High-speed ultracentrifugation at 220,000 g for 60 min was performed to separate soluble protein-detergent complex from membrane lipids. The soluble protein-detergent complex was further purified by affinity chromatography using a 1-ml HiTrap chelating column (GE Healthcare) immobilized with Ni^{2+} equilibrated with buffer B (20 mM Tris-HCl, pH 8.5, 300 mM NaCl, 10% glycerol, 0.1% DDM). The column was washed with 50 mM imidazole added to buffer B, and the bound protein was eluted with 500 mM imidazole in buffer B.

Ion-exchange chromatography (Section 2.7.4) was used to further purify the membrane fraction Hpa1-His_6. The buffer of Hpa1-His_6 was changed into starting buffer (20 mM Tris-HCl, pH 8.5, 50 mM NaCl, 10% glycerol, 0.1% DDM) using a desalting column (GE Healthcare). The HiTrap Q HP 5 ml column (GE Healthcare) stored in 20% ethanol was washed with 5 CVs of degassed water, and then equilibrated with starting buffer. Hpa1-His_6 was loaded onto the HiTrap Q HP 5ml column and washed with 3 CV of starting buffer. A NaCl gradient elution was performed with start buffer and elution buffer (20 mM Tris-HCl, pH 8.5, 500 mM NaCl, 10% glycerol, 0.1% DDM). The protein peaks were collected and analyzed by on an SDS-PAGE gel. Figure 3.4A lane 3 shows the membrane fraction Hpa1-His_6 after the ion-exchange chromatography. A His_6-tag western blot (Section 2.7.6) was used to confirm the identity of the expressed membrane fraction Hpa1-His_6 (Figure 3.4B lane 2)

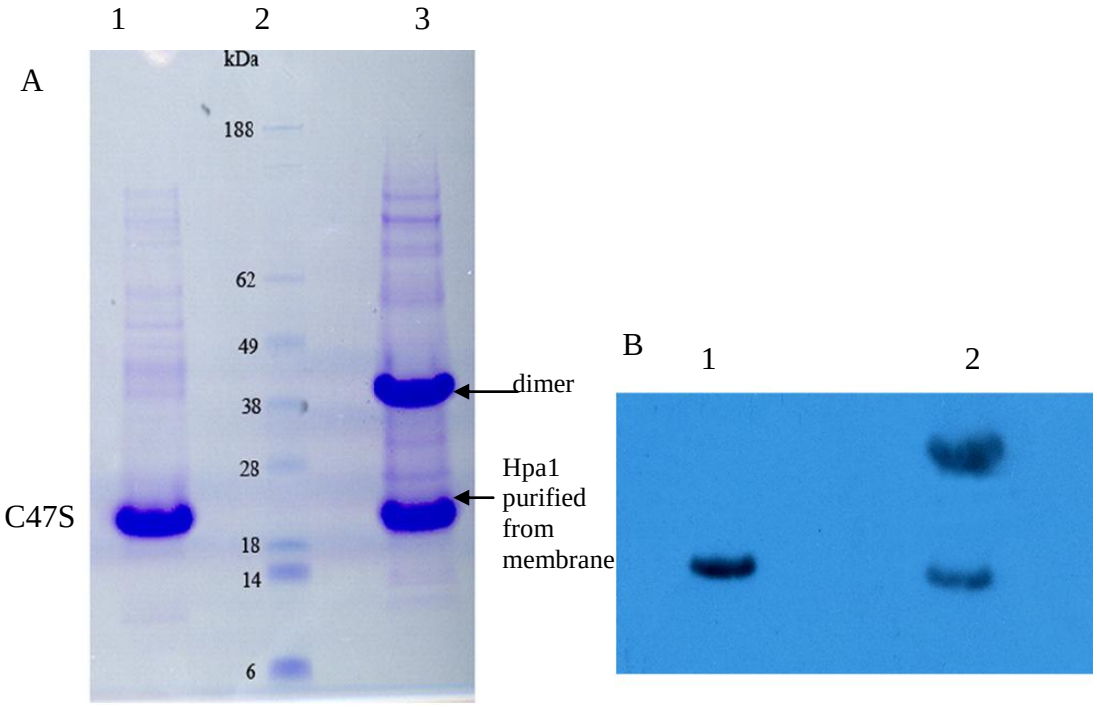

Figure 3.4 SDS-PAGE and western blot of Hpa1-His$_6$ and C47S purified from *E. coli* membrane. (A) Lane 1 is Hpa1 derivative C47S; Lane 3 is Hpa1-His$_6$ purified from membrane; Lane 2 is a molecular weight marker. (B) Lane 1 is the western blot signal for C47S corresponding to lane 1 in A; Lane 2 is the signal for Hpa1-His$_6$ from the membrane in a western blot corresponding to lane 3 in A.

3. 2 Analytical size exclusion chromatography of soluble Hpa1-His$_6$

Analytical size exclusion chromatography (SEC) (Section 2.8) was used to determine the molecular weight of soluble Hpa1-His$_6$. The buffer composition used for all experiments (including for the molecular weight standards) was 20 mM Tris-HCl pH 8.5, and 100 mM NaCl. The column was pre-equilibrated with 1 CV of water and then 2 CV of buffer prior to all chromatographic elution. Dextran blue 2000 (GE Healthcare) was applied to the column prior to the protein standards to determine the void volume (V_o) of the column. bovine serum albumin (62.9 kDa), ovalbumin (46.7 kDa), catalase (213 kDa) and adolase (182 kDa) (GE Healthcare) were dissolved in buffer at 5 mg/ml, injected into the Superdex 200 PC 3.2/30 column (GE Healthcare) and eluted with 1 column volume of buffer to get the elution volumes of these proteins (Table 3.1). Figure 3.5 shows that after purification Hpa1-His$_6$ is not a single species and that the maximum species has the elution volume 1.53±0.02 ml.

The K_{av} of Hpa1-His_6 and each protein standard were calculated as in Section 2.8. The K_{av} values for the protein standards were plotted on a logarithmic scale against the corresponding M_r and a line of best fit was drawn (Figure 3.6). The molecular weight of Hpa1-His_6 was calculated according to this curve, which is 142.3 kDa (Table 3.1), suggesting that Hpa1-His_6 could be a decamer.

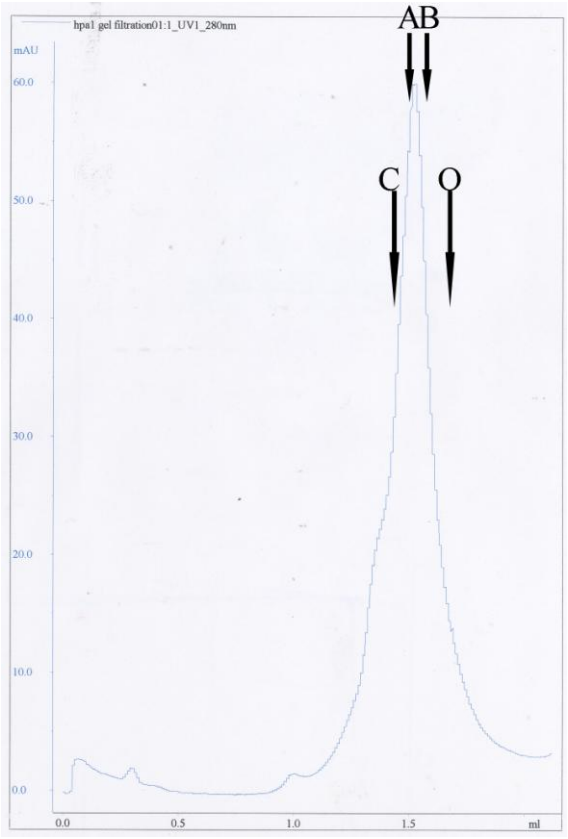

Figure 3.5 The elution chromatography of Hpa1-His_6 from a superdex 200 PC 3.2/30 gel filtration column (Molecular weight determination of Hpa1-His_6) A=aldolase (182 kDa), B= bovine serum albumin (62.9 kDa), C= catalase (213 kDa), O= ovalbumin (46.7 kDa).

Protein	Molecular Weight	Elution Volume*	K_{av}
Aldolase	182 kDa	1.49±0.02 ml	0.3228
Catalase	213 kDa	1.44±0.02 ml	0.2861
Bovine Serum Albumin	62.9 kDa	1.59±0.02 ml	0.3962
Ovalbumin	46.7 kDa	1.69 ±0.02 ml	0.4695
Hpa1-His_6	142.3 kDa	1.53±0.02 ml	0.3521
Blue Dextran	More than 2000 kDa	1.05±0.02 ml	0

Table 3.1 Molecular weights and elution volumes of standard proteins and Hpa1-His_6. * errors estimated from the calibration curve (data not shown), 0.02 ml= 6 kDa.

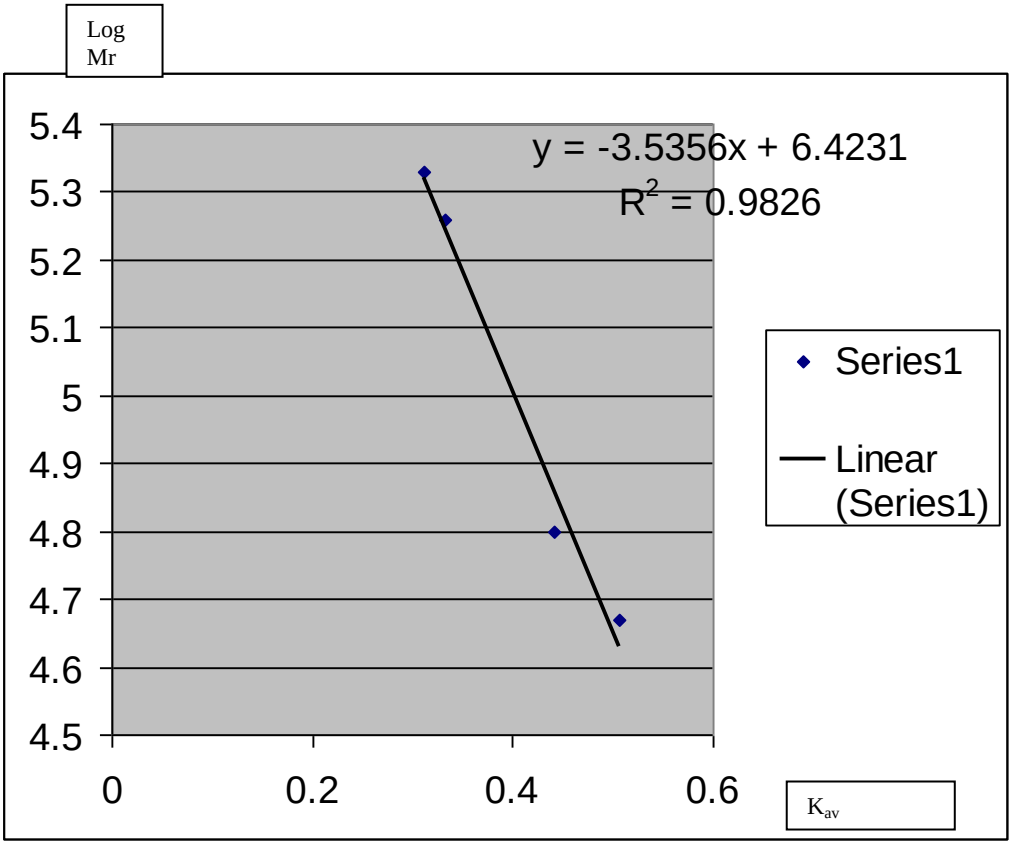

Figure 3.6 The log of the M_r of the standards *versus* K_{av} calibration curve.

3.3 Overexpression and purification of Hpa1 derivative C47S

Harpins share several characteristics, such as a low isoelectric point, enrichment for glycines, and a lack of cysteine residues (Charkowski *et al*., 1998). Hpa1, similar to other harpins, has a low isoelectric point of 4.06, and high percent of glycines of 13.5% (calculated by Vector NTI). However, there is one cysteine residue in Hpa1. To study the function of this residue, the mutation of the cysteine to serine (C47S) was performed to determine if cysteine cross linking was essential for correct protein folding in Hpa1. The QuikChange multi site-directed mutagenesis system (Stratgene) was employed for *in vitro* site directed mutagenesis experiments.

Site directed mutagensis of Hpa1-His_6 was performed as described in Section 2.6. The mutagenic primers *hpa1*-C47S Forward and *hpa1*-C47S Reverse were used as detailed in Table 2.4. The pET21a-*hpa1* ds-DNA was used as the template. Mutant strand synthesis using PCR was achieved with an extension time of 6 minutes. The clones were sequenced to confirm the desired mutant. The correct clones were transformed into BL21(DE3) for overexpression.

We attempted to purify Hpa1 C47S from the soluble fraction; however, no C47S was found in the soluble fraction. The membrane fraction of C47S was purified as membrane fraction Hpa1-His_6 in section 3.1.3. His_6-tag western blot (Section 2.7.6) was used to confirm the correct expression of the membrane fraction C47S. Figure 3.4A lane 1 shows the purification of C47S from *E. coli* membranes. Figure 3.4B lane 1 shows the western blot of C47S. The discussion of Hpa1 derivative C47S is given in section 3.9.2.

3.4 Amyloid fibrils formation of Hpa1-His_6 at acidic pHs

The Type III-dependent harpins from plant pathogenic bacteria, HpaG from *X. axonopodis*, HrpN from *E. amylovora* and HrpZ from *P. syringae* pv. syringae were found to form amyloid fibrils in XVM2, the hrp induction minimal medium (Oh *et al.*, 2007). Hpa1 has 59.7% sequence identity with HpaG, 17.2 % with HrpN, and 14.5 % with HrpZ.

In this study, the amyloid fibril formation of soluble Hpa1-His_6 was tested at different pHs. The purified Hpa1-His_6 in buffer (20 mM Tris-HCl pH 8.5, 300 mM NaCl), was concentrated and diluted into buffers at pH 8.5 (20 mM Tris-HCl, 50 mM NaCl), pH 8.0 (20 mM Tris-HCl, 50 mM NaCl), pH 7.5 (20 mM Tris-HCl, 50 mM NaCl), pH 7.0 (20 mM MES, 50 mM NaCl), pH 6.5 (20 mM MES, 50 mM NaCl), and pH 6.0 (20 mM MES, 50 mM NaCl) in 40 μM, respectively. Samples were screened by TEM immediately after dilution for the Hpa1-His_6 fibrils in each buffer (Figure 3.7 A and D, 3.8 A and D, 3.9 A and D).

Our TEM studies revealed that purified Hpa1-His_6 is prone to aggregate in buffers at pH 8.5 and 8.0 (Figure 3.9 A and D). After incubation of Hpa-His_6 at each buffer for 1 day at room temperature (RT), the morphology of Hpa1-His_6 in each buffer was observed under TEM. Hpa1-His_6 forms ribbon fibrils with a 10 nm width at pH 6.0 and pH 6.5 after 1 day incubation at RT (Figure 3.7 B and E); however, at pH 7.0, 7.5, 8.0 and 8.5 (Figure 3.8 B and E, 3.9 B and E) no fibrils formed .

After a 12 day incubation at RT, the Hpa1-His_6 at each pH was observed again under TEM. Ribbon fibrils formed by Hpa1-His_6 after 1 day incubation in pH 6.0 and pH 6.5 were expected to form twisted fibrils after the long incubation time. However, there was no difference found between fibrils of 1day incubation at pH 6.0 and 6.5 and those after 12 days incubation (Figure 3.7 C and F).

After 12 days incubation at RT, Hpa1-His_6 aggregated at pH 7.5 (Figure 3.8 F) and pH 8.0 (Figure 3.9 C).

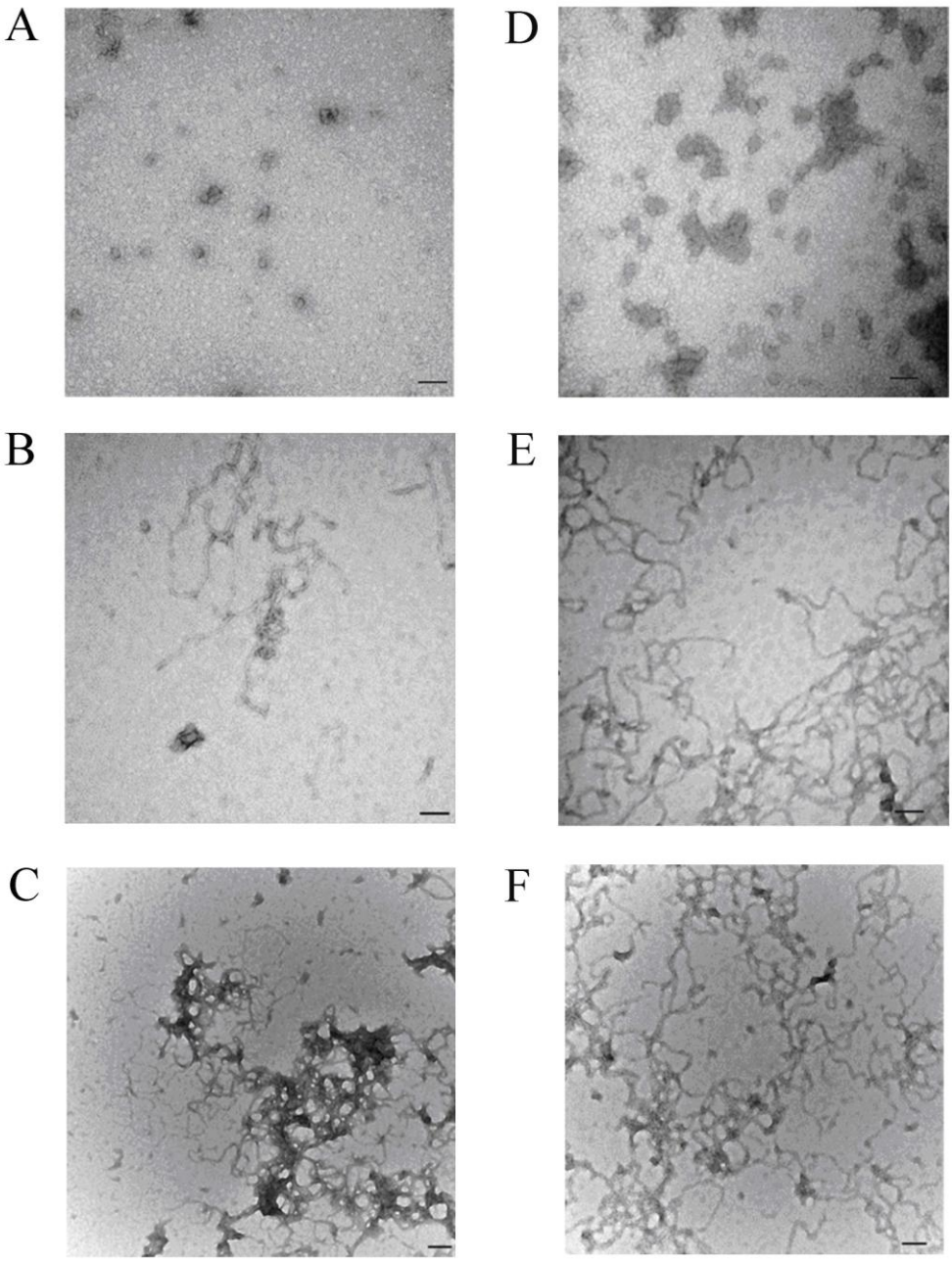

Figure 3.7 Amyloid fibrils formed by Hpa1 at pH 6.0 and 6.5. (A), (B) and (C) show 40 µM of Hpa1-His_6 in buffer 20 mM MES, pH 6.0, 50 mM NaCl, 0 day, 1 day and 12 days respectively. (D), (E) and (F) show 40 µM of Hpa1-His_6 in buffer 20 mM MES, pH 6.5, 50 mM NaCl, 0 day, 1day and 12 days respectively. The time point 0 day is defined as the moment immediately following dilution of the protein in each buffer. (Scale bar = 100 nm)

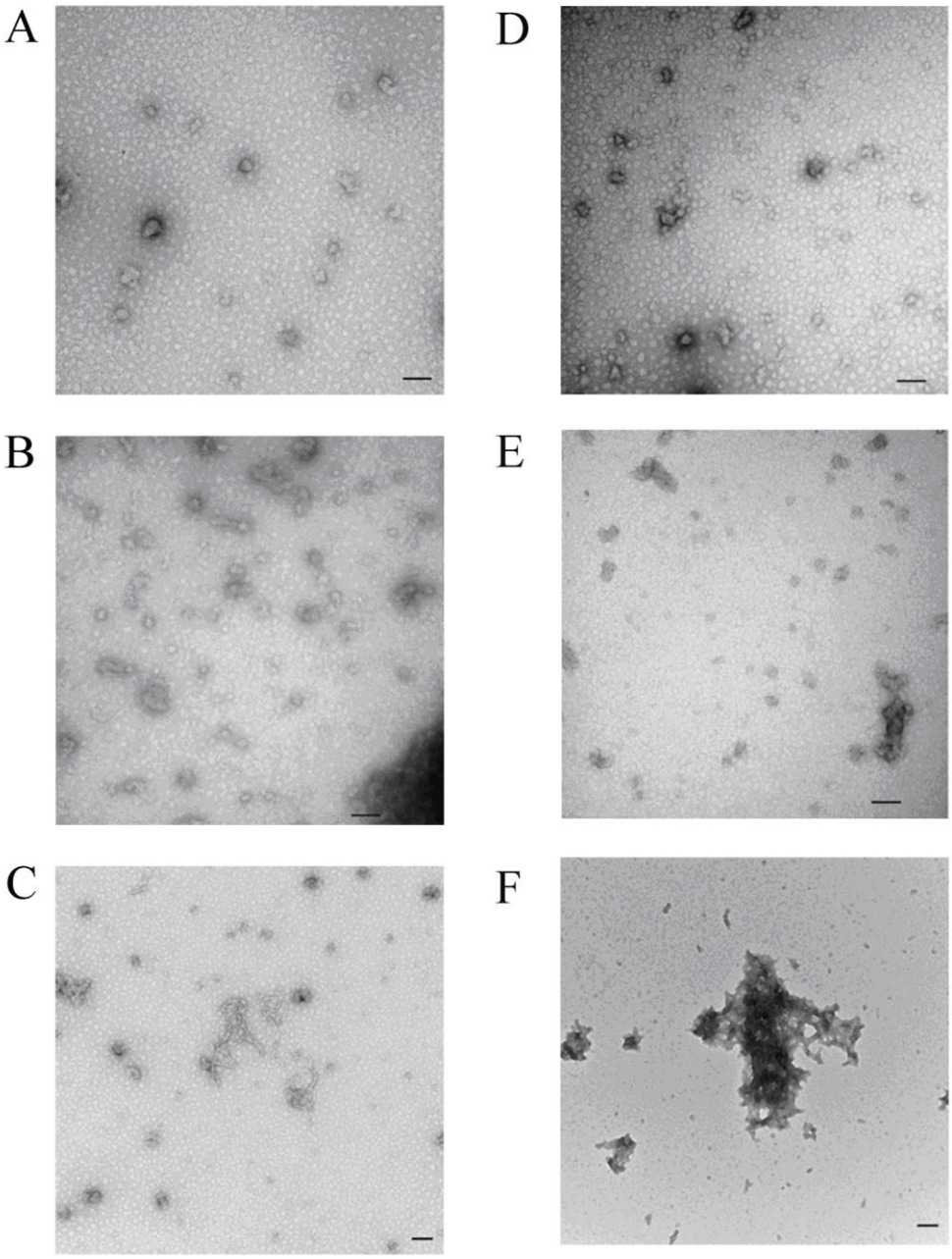

Figure 3.8 TEM analysis of Hpa1 at pH 7.0 and 7.5. (A), (B) and (C) show 40 µM of Hpa1-His_6 in buffer 20 mM Tris-HCl, pH 7.0, 50 mM NaCl, 0 day, 1 day and 12 days respectively. (D), (E) and (F) show 40 µM of Hpa1-His_6 in buffer 20 mM Tris-HCl, pH 7.5, 50 mM NaCl, 0 day, 1day and 12 days respectively. The time point 0 day is defined as the moment immediately following dilution of the protein in each buffer. (Scale bar = 100 nm)

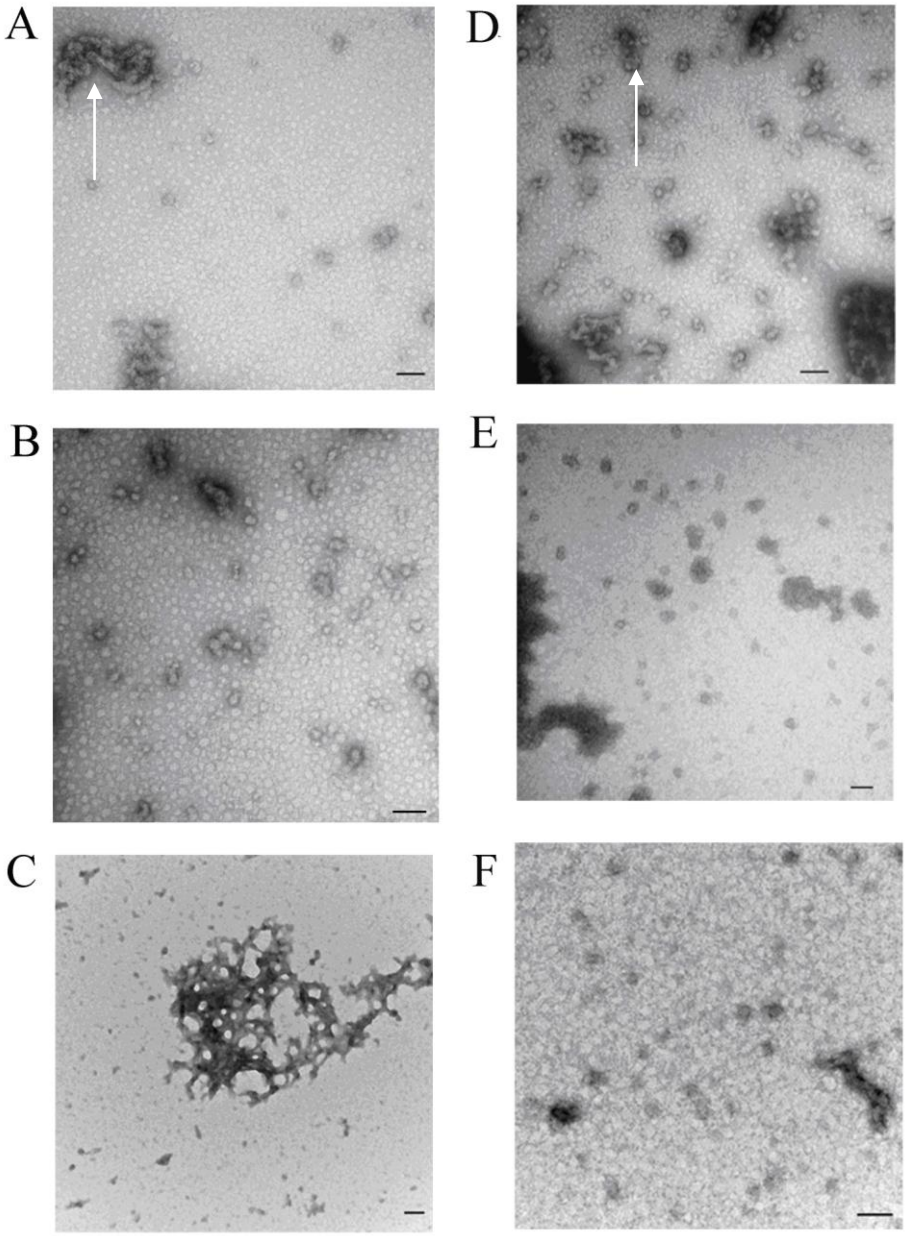

Figure 3.9 TEM analysis of Hpa1 at pH 8.0 and 8.5. (A), (B) and (C) show 40 µM of Hpa1-His_6 in buffer 20 mM Tris-HCl, pH 8.0, 50 mM NaCl, 0 day, 1 day and 12 days respectively. (D), (E) and (F) show 40 µM of Hpa1-His_6 in buffer 20 mM Tris-HCl, pH 3.5, 50 mM NaCl, 0 day, 1 day and 12 days respectively. The time point 0 day is defined as the moment immediately following dilution of the protein in each buffer. Arrows show the aggregation of Hpa1. (Scale bar = 100 nm)

To determine whether the fibrillar form of Hpa1 is amyloid, a Congo red binding assay was performed: 40 µM Hpa1-His_6 was diluted in buffer 20 mM MES, pH 6.5, 50 mM NaCl and incubated at RT for 1 day to form fibrils. 20 µM Congo red was dissolved in the same buffer. The absorbance spectrum of Congo red from 400 to 700 nm was recorded as a control (Figure 3.10 dotted line). 20 µM Congo red was then mixed with 40 µM fibrils formed by Hpa1-His_6 and the absorbance spectrum of Congo red from 400 to 700 nm was recorded again (Figure 3.10 solid line). The binding of Hpa1 fibrils to Congo red causes a maximum absorbance shift of Congo red from 495 nm to 516 nm (Figure 3.10), which indicates that the Hpa1 fibrils are amyloid fibrils.

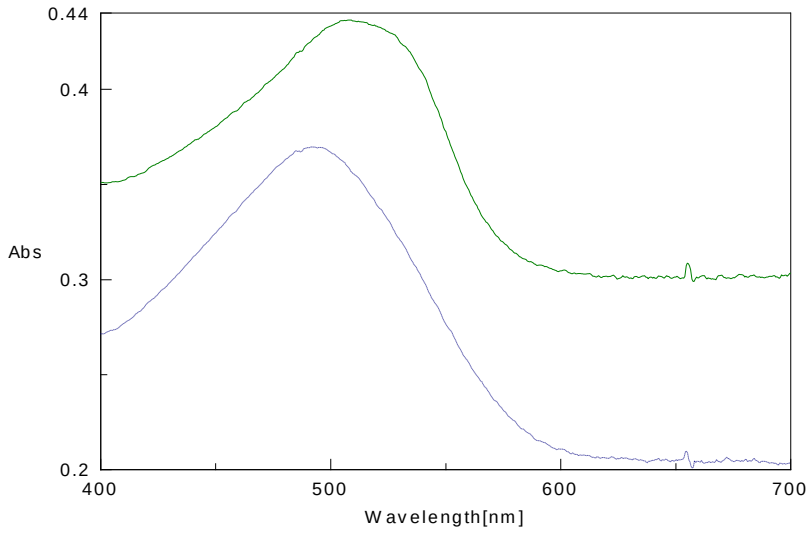

Figure 3.10 Congo red binding of Hpa1-His_6 fibrils. Absorbance spectrum of the CR solution in the absence (dotted line) and presence (solid line) of Hpa1-His_6 fibrils.

3.5 Chemical cross-linking of Hpa1-His_6

In order to show the oligomeric state of Hpa1-His_6, cross-linking experiments were undertaken. Cross-linkers are chemical reagents used to conjugate molecules together by a covalent bound. Hpa1-His_6 crosslinking *in vitro* was performed using DSP and EGS, with 12 Å and 16.1 Å spacer arms, and analyzed by gel electrophoresis.

The buffer of purified Hpa1-His_6 was exchanged into 20 mM Na_2HPO_4, 100 mM NaCl, pH 8.5, prior to crosslinking. An EGS solution was freshly prepared in DMSO. The protein sample and EGS solution were mixed and left at room temperature for 1 hour. The reactions were terminated by adding 1M Tris buffer. The samples were then analysed on a 4-12% SDS-PAGE gel. Figure 3.11 shows approximately seven bands, corresponding to the different oligomeric states of Hpa1.

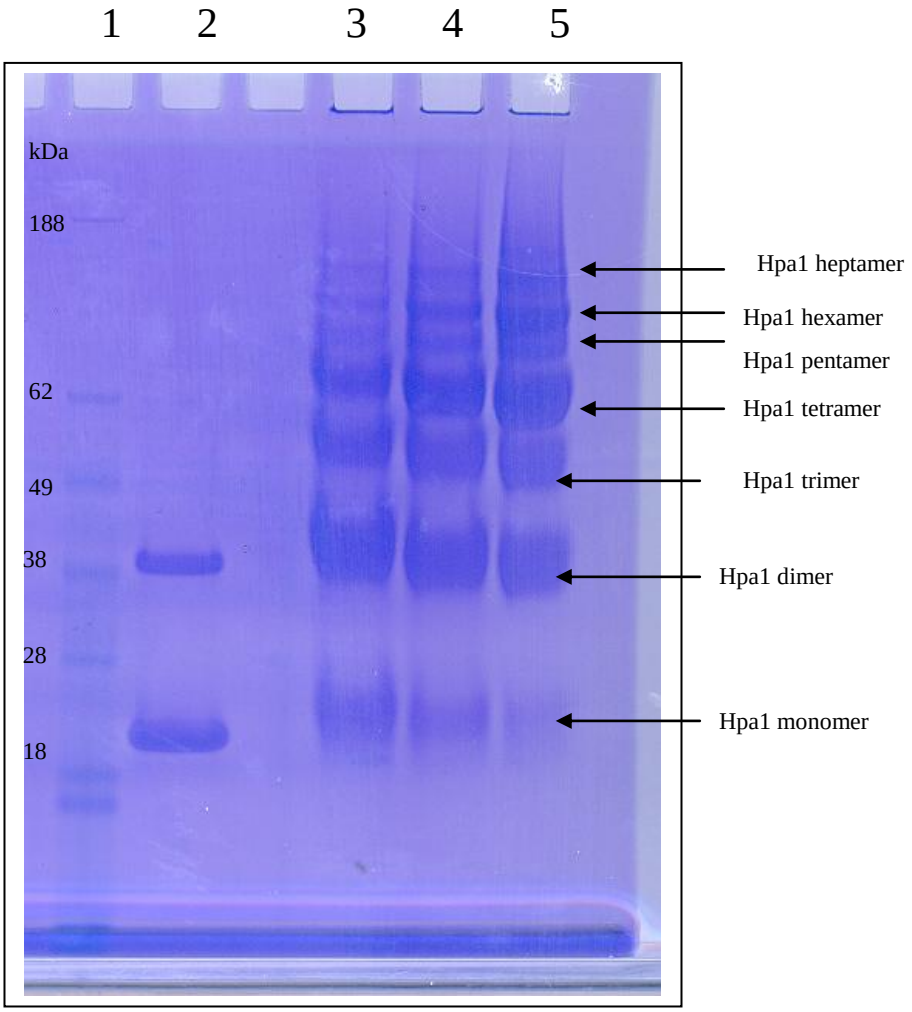

Figure 3.11 Chemical cross-linking of Hpa1-His_6
Lane 1: A protein molecular weight (M_r) marker
Lane 2: 1 mg/ml Hpa1-His_6 in buffer 20 mM $NaHPO_4$, 100 mM NaCl, pH 8.5
Lane 3-5: 1 mg/ml Hpa1-His_6 in buffer 20 mM $NaHPO_4$, 100 mM NaCl, pH 8.5, crosslinked with 8 mM, 16 mM and 30 mM EGS, respectively, at 37 ^oC, for 30 mins.

PopA, a harpin-like protein from the bacterial plant pathogen *R. solanacearum*, was thought to be a Ca^{2+}-dependent lipid binding protein, for which Ca^{2+} could promote

oligomerization (Racape *et al.*, 2005). 2 mM $CaCl_2$ and 0.1 mg *E. coli* lipsomes (Section 2.13 for liposomes preparation) were mixed in the crosslinking buffer respectively or simultaneously to show their effects in the oligomerization of Hpa1. However, no significant difference was found in the presence of 2 mM $CaCl_2$, or 0.1 mg *E. coli* liposome, or both of them simultaneously, compared with Hpa1 only (Figure 3.12).

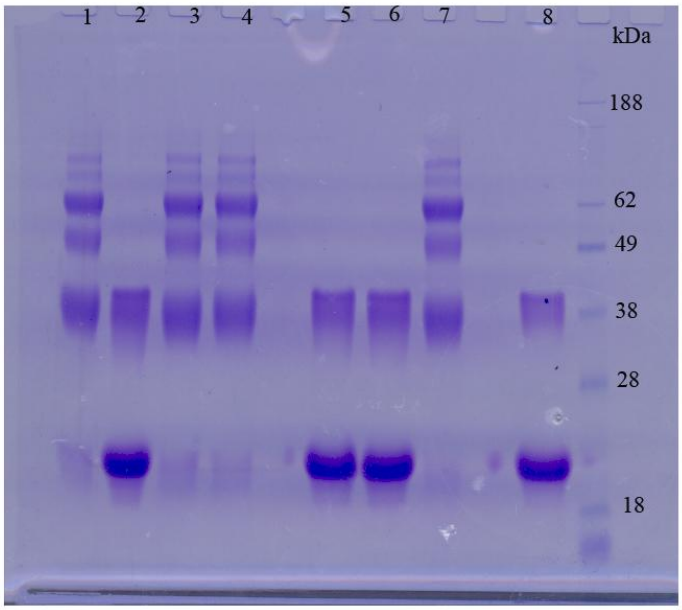

Figure 3.12 Chemical cross-linking of Hpa1-His_6 in the presence of $CaCl_2$ and liposomes. Lane 1: 1 mg/ml Hpa1-His_6 mixed with 0.5 mM DSP, 2 mM $CaCl_2$ and 0.1 mg *E. coli* lipsomes, 37 ^oC, 0.5 hour. Lane 2: 1 mg/ml Hpa1-His_6, mixed with 0.1 mg *E. coli* liposomes and 2 mM $CaCl_2$, 37 ^oC, 0.5 hour. Lane 3: 1 mg/ml Hpa1-His_6, mixed with 0.5 mM DSP and 0.1 mg *E. coli* liposomes, 37 ^oC, 0.5 hour. Lane 4: 1 mg/ml Hpa1-His_6, mixed with 0.5 mM DSP and 2 mM $CaCl_2$, 37 ^oC, 0.5 hour Lane 5: 1 mg/ml Hpa1-His_6, mixed with 0.1mg *E. coli* liposomes, 37 ^oC, 0.5 hour. Lane 6: 1 mg/ml Hpa1-His_6, mixed with 2 mM $CaCl_2$, 37 ^oC, 0.5 hour. Lane 7: 1 mg/ml Hpa1-His_6, mixed with 0.5 mM DSP, 37 ^oC, 0.5 hour. Lane 8: 1 mg/ml Hpa1-His_6.

In conclusion, our cross-linking data indicates that the maximal oligomer state of Hpa1 is a heptamer, which is inconsistent with the decamer from SEC (Section 3.2). This difference might be explained by the spacer arm being sub-optimal for cross-linking the active site in the Hpa1 oligomers. In addition, although Ca^{2+} and liposomes were reported to promote oligomerization of harpin (Racape *et al.*, 2005); in this study, such effects could not be detected in our experiments. A detailed discussion of these findings is given in Section 3.9.3.

3.6 Circular dichroism (CD) spectroscopy of Hpa1-His_6

The formation of amyloid fibrils accompanies a secondary structure change and amyloid fibrils are β-sheet rich structures (Chiti and Dobson, 2006). In order to study the secondary structure transition of Hpa1-His_6 during fibril formation, CD spectroscopy was used. In order to minimize the strong absorbance from Cl^- in the far UV region, the Hpa1-His_6 buffer was changed to Tris-base or NaH_2PO_4, with NaF as salt.

4 µM Hpa1-His_6 in 20 mM Tris-base pH 8.5 (pH adjusted by H_2SO_4), 20 mM NaF, generated a CD spectrum from 260-190 nm. Meanwhile, Hpa1-His_6 was diluted into 20 mM NaH_2PO_4 pH 6.5, 20 mM NaF to have a final concentration 5 µM and incubated at room temperature for 1 day. The CD spectrum of this 5 µM Hpa1-His_6 at pH 6.5 was recorded. All CD spectra were analyzed using the software Dichroweb online (Section 2.11, Whitmore and Wallace, 2004 and 2008).

Our CD analyses indicated that Hpa1-His_6 at pH 8.5 has a structural content of 34.8% helix, 7.5% sheet, 27.9% turn, and 29.9% unordered (Figure 3.13). After incubation of Hpa1 at pH 6.5 for 1 day, the spherical oligomer Hpa1 formed curvilinear fibrils under TEM (Figure 3.7 E), and the percentage of helix decreased to 14.5%, whereas the sheet content increased to 29.2%, with 23.4% turn, and 32.9% unordered structure (Figure 3.13). In conclusion, the formation of fibrils of Hpa1 increases the sheet content, but not all the secondary structure of the Hpa1 fibrils is β-sheet structure.

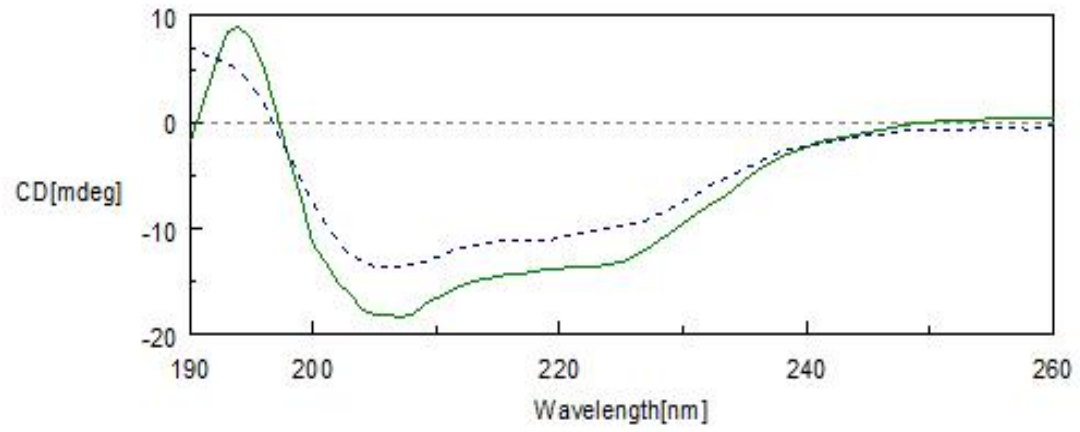

Figure 3.13 CD spectroscopic analysis of soluble Hpa1-His_6 at pH 8.5 and pH 6.5. 5 µM soluble Hpa1 at pH 8.5 (solid line), 5 µM soluble Hpa1 at pH 6.5, 1 day incubation (dotted line).

3.7 Membrane disrupted by Hpa1-His_6

Liposomes were prepared from *E. coli* extracted lipids as described in Section 2.13 and incubated with 5 mg Hpa1 at different pHs (pH 6.0, 6.5, 7.0, 7.5, 8.0 and 8.5). After 1 day incubation, the bound Hpa1 with liposomes and unbound Hpa1 were separated using sucrose gradient centrifugation (Section 2.13). The liposome fractions were pipetted and loaded onto a SDS/PAGE gel to show bound Hpa1. Only at pH 6.0 and 6.5, Hpa1 could bind to liposomes (Figure 3.14). In addition, these liposomes bound with Hpa1 were observed under TEM (Figure 3.15 D, E and F), revealing that these liposomes were broken by the Hpa1 at pH 6.0 and pH 6.5.

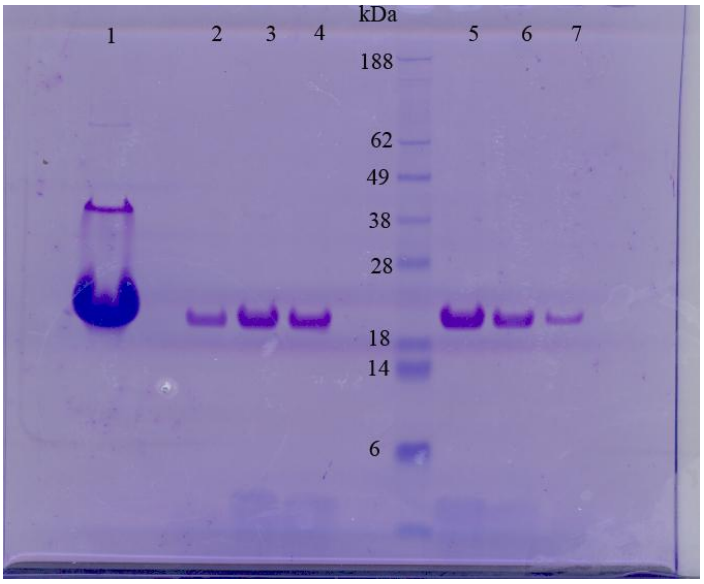

Figure 3.14 A SDS/PAGE gel shows the Hpa1-His$_6$ bound with liposome after sucrose gradient centrifugation Lane 1: 1 mg/ml Hpa1-His$_6$. Lane 2, 3, 4: Hpa1-His$_6$ from 10% sucrose fraction of liposome, at pH 6.5. Lane 5, 6, 7: Hpa1-His$_6$ from10% sucrose fraction of liposome, at pH 6.0

To test the function of membrane fraction Hpa1-His$_6$ and the C47S derivative on the membrane, we reconstituted the detergent solubilised Hpa1-His$_6$ and C47S into membranes as described in Section 2.13. The liposomes were prepared and mixed with detergent solubilised Hpa1-His$_6$ and C47S. The detergents in the system were moved by Bio-bead SM-2 absorbent (Bio-Rad®) and integrated membranes were spun down. TEM observations show both the membrane fraction Hpa1-His$_6$ and C47S disrupt membranes (Figure 3.15 B and C).

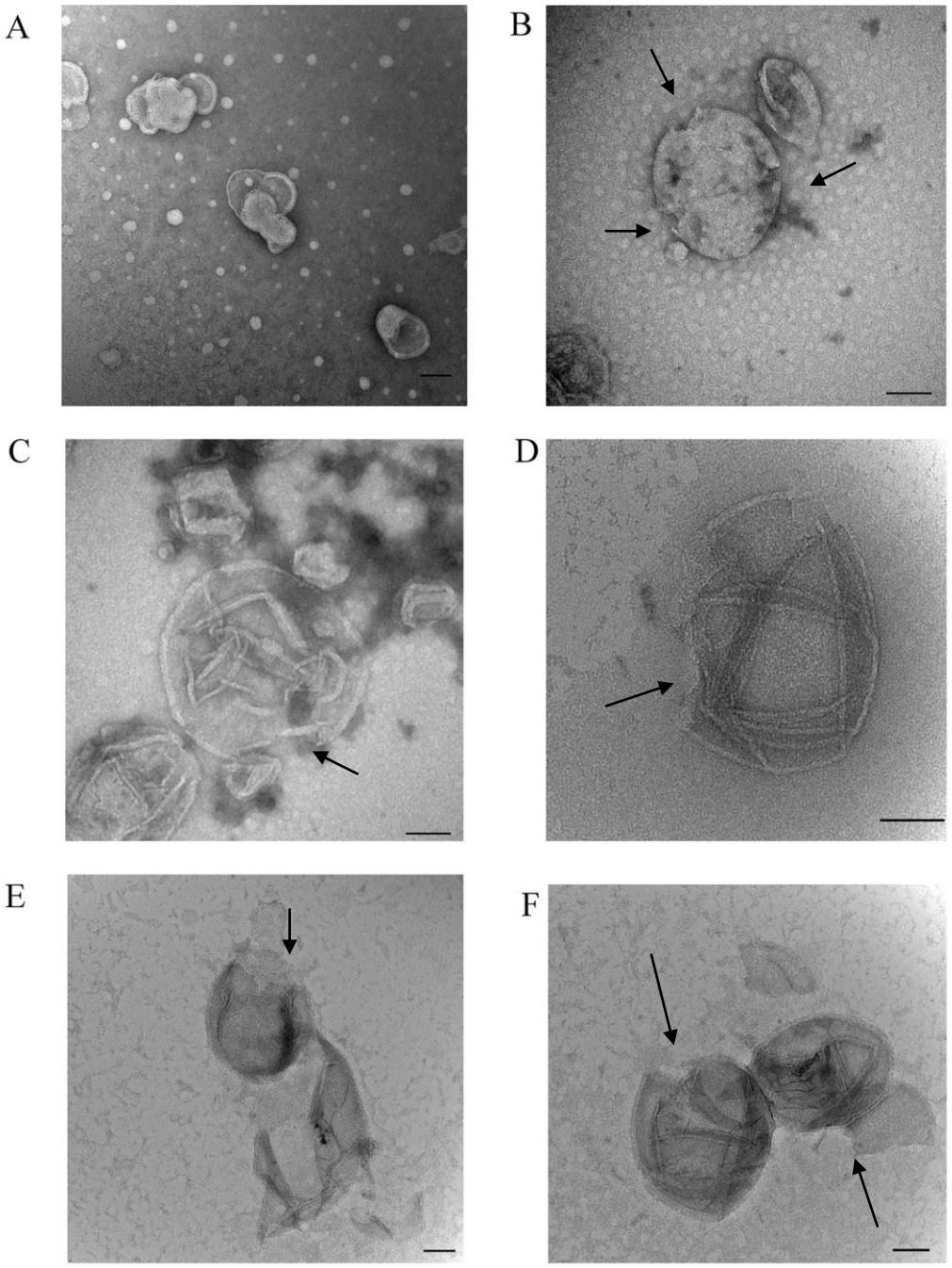

Figure 3.15 Negative-staining electron microscopy analysis shows that Hpa1-His_6 purified from soluble and membrane fraction of *E. coli* disrupt liposomes (A) Intact liposomes. (B) Liposomes lysed by membrane fraction Hpa1-His_6. (C) Liposomes lysed by membrane fraction C47S. (D) and (E) Liposomes lysed by soluble Hpa1-His_6 at pH 6.5 (F) Liposomes lysed by soluble Hpa1-His_6 at pH 6.0. The black arrow points to the lysed liposomes (scale bar = 100 nm)

3.8 Crystallization of Hpa1

Hpa1-His_6 (20 mM Tris-HCl buffer at pH 8.5, 100 mM NaCl, and 4 μM DTT), was purified as described in section 3.1.2 and 3.1.3, and concentrated to 10 mg/ml for crystallization trials.

The following crystallization suites were used:
1 The classics suites (Nextal Biotech)
2 The classics Lite suites (Nextal Biotech)
3 Structure Screen 1, 2 (Molecular Dimensions)
4 Random sparse matrix crystallization screen Wizard I, Wizard II (Emerald Biosystems.)

1ml crystallization buffer from each crystallization suite was transferred into the wells of crystallization plates. 2 μl 10 mg/ml Hpa1-His_6 was mixed with 2 μl reservoir buffer from the kits, and loaded on the cover slip of each well, to form the hanging drops at 18 ^{o}C.

The crystallization of the above screening conditions did not yield any crystals or even needles. Self-prepared buffer conditions were used to screen for buffers suitable for crystallization of Hpa1. PEG4000 and PEG400 were taken as precipitants, concentration from 5% to 25%, in 100 mM Tris-HCl at different pHs from 7.0 to 8.5. Fortunately, some small needles or spherulites could be found in buffer containing 15% PEG4000, 100 mM Tris-HCl at pH 7.8 (Figure 3.16). However, these needle-like spherulites or crystallines were too small to obtain any diffraction and not reproducible. Further trials did not get any promising result than these needle-like crystals.

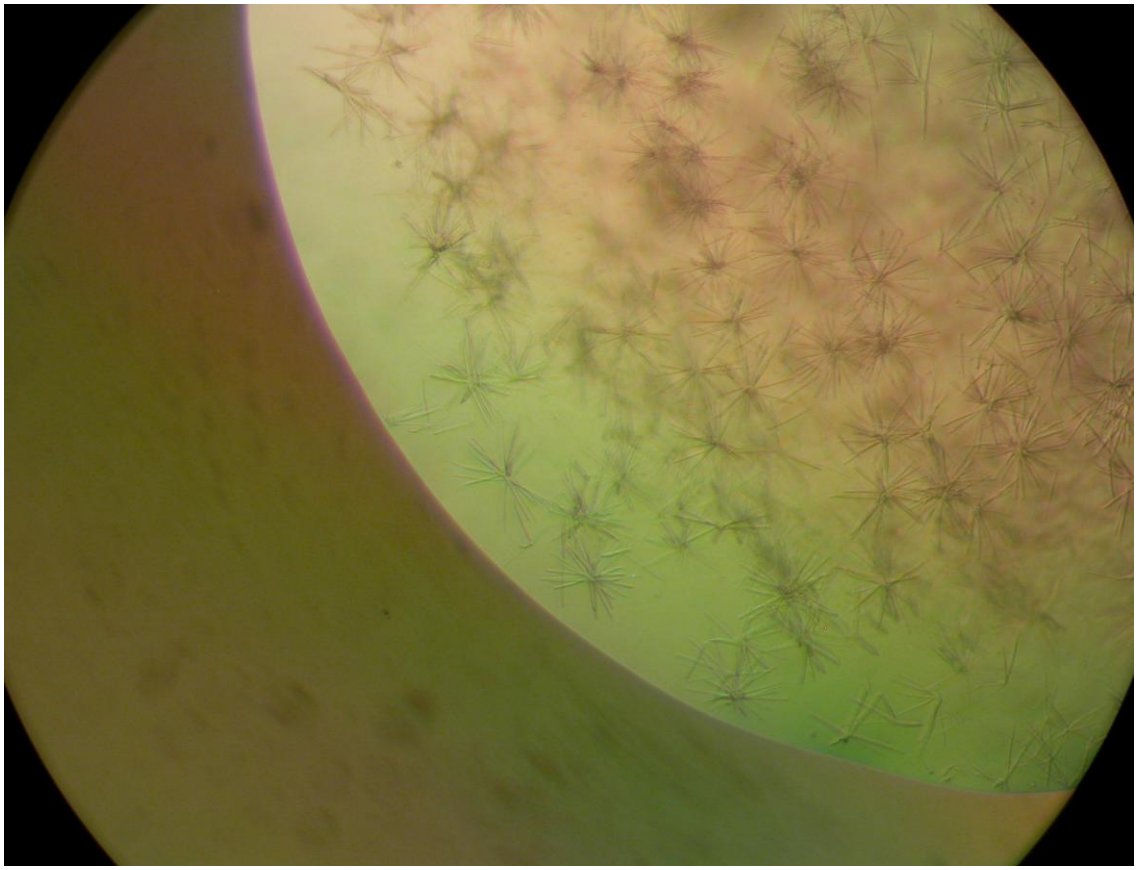

Figure 3.16 Needle-like crystallines or aggregation formed by Hpa1-His_6 at 100 mM Tris-HCl buffer at pH 7.8 and 15% PEG4000.

3.9 Discussion

Harpins play an important function between the plant and plant pathogen (Alfano and Collmer, 2004). They act by eliciting a complex natural defence mechanism in plants, analogous to a broad spectrum immune response in animals (Alfano and Collmer, 2004)**.** The harpin-like protein PopA, from the bacterial plant pathogen *Ralstonia solanacearum*, has a high affinity for sterols and sphingolipids *in vitro* and requires Ca^{2+} for lipid binding and oligomerization (Racape *et al.*, 2005). Recently, HpaG was found to form amyloid fibrils (Oh *et al.*, 2007). In order to investigate the biochemical characteristic of Hpa1, we over-expressed and purified it from *E. coli* and found fibril forming conditions for Hpa1.

3.9.1 Over-expression and purification of Hpa1

The low mobility of harpins on an SDS-PAGE gel is reported in several publications and could be a general characteristic of harpins (Charkowski *et al*., 1998). In this study, Hpa1 has a similar low mobility on SDS-PAGE gels, shifting from 14 kDa to around a 20 kDa position (Figure 3.3). Western blot and mass spectra confirmed the correct expression of Hpa1 (Section 3.1.3), and eliminated the unexpected contamination of proteins. This characteristic of harpins could reflect the special amino acid composition of harpins, or unique structure of harpins, which has to be determined in future work.

3.9.2 Function of cysteine in Hpa1

Although the lack of cysteine is considered as a general characteristic of harpins (Charkowski *et al*., 1998), Hpa1 has one cysteine residue. To investigate the function of this residue, we mutated Cys to Ser (C47S) and purified this derivative from *E. coli*. In contrast to the WT Hpa1, only the membrane fraction of C47S was purified successfully. As expected, the lack of cysteine in Hpa1 led to the dissociation of dimer to monomer (Figure 3.4). In addition, the formation of intermolecular disulfide bonds could also stabilize Hpa1 in the soluble state, as the derivative C47S was absent in the soluble fraction in its purification (Section 3.3).

3.9.3 Oligomerization of Hpa1

The oligomeric state of harpin was reported for HpaG, which forms a tetramer (Oh *et al*., 2007). PopA was thought to be a Ca^{2+}-dependent lipid binding protein, for which Ca^{2+} could promote oligomerization (Racape *et al.*, 2005). In this study, *in vitro* cross-linking of Hpa1 was performed with SEC used to analyse the oligomeric state of Hpa1. Analytical SEC shows Hpa1 is not a single species in buffer and the major species has a molecular weight 142.3 kDa (Table 3.1), which indicates that this species of Hpa1-His_6 may be a decamer in solution.

To understand the effect of Ca^{2+} and lipids on oligomerization of Hpa1, liposomes and Ca^{2+} were mixed with Hpa1 and cross-linking was performed. In contrast to

PopA, Ca^{2+} and lipids had no effect on the oligomerization of Hpa1 (Figure 3.12). However, the possibility of an effect of Ca^{2+} and lipids on the oligomerization of Hpa1 can not be ruled out, since the purified Hpa1 is already in its oligomeric state, a decamer rather than a monomer. The equilibrium between monomeric and oligomeric state of fibril forming proteins was reported and some parameters are found to shift this equilibrium, e.g. anionic strength in the buffer (Cruz *et al.*, 2005). The possible shift between monomer and oligomer of Hpa1 could be studied in future work.

3.9.4 Amyloid fibril formation of Hpa1

A pH-dependent folding transition has been widely reported in amyloid forming proteins (Cruz *et al.*, 2005; Lai *et al.*, 1996; Morozova-Roche *et al.*, 2000; Smith *et al.*, 2003; Uversky and Fink, 2004). The Type III-dependent harpins from plant pathogenic bacteria, HpaG from *X.axonopodis*, HrpN from *E. amylovora* and HrpZ from *P. syringae* pv. syringae were found to form amyloid fibrils in XVM2, the hrp induction minimal medium (Oh *et al.*, 2007). However, the effect of pH on fibril formation by harpins is still enigmatic. In this study, a series of buffers with different pHs (6.0, 6.5, 7.0, 7.5, 8.0 and 8.5) were prepared to determine their influence on fibril formation of Hpa1. As observed by TEM, short curved fibrils formed by soluble Hpa1 at pH 6.0 and 6.5 after 1day incubation at RT (Figure 3.7 B, C, E and F). A Congo red binding assay indicated that these fibrils are amyloid-like, similar to the fibrils formed by HpaG of *X. axonopodis* (Oh *et al.*, 2007). The CD spectrum shows that the formation of fibrils by Hpa1 at acidic pH involves the transition of secondary structure from helix to strand (Section 3.6), similar to those observed in the fibrils formed by HpaG (Oh *et al.*, 2007).

Hpa1 and the C47S derivative purified from membrane cannot form fibrils. The possible explanation is that the detergents bound to the protein, used in the purification of protein from the membrane, mask the surface for fibril-assembly.

Although decreasing the net charge of proteins was thought to be the reason for the formation and stabilization of fibrils (Chiti *et al*., 2002; Schmitts and Scholtz, 2003); in this study, a lower pH of 4-5 around the pI (4.06, calculated by Vector NTI) of

Hpa1, were found to induce the precipitation of Hpa1 (data not shown), which indicates that the formation of fibrils needs electrostatic conditions to allow folding of Hpa1.

The possible mechanism for fibril formation of Hpa1 at acidic pHs is that the shift of pH changes conformation of Hpa1 and thus exposes the protein surface for fibril-assembly. Further work will be required to support this hypothesis or find out another mechanism by which fibril-assembly occurs at acidic pH of Hpa1.

3.9.5 Membrane binding and disruption of Hpa1

The membrane binding characteristic of PopA, an harpin-like protein, was reported (Racape *et al.*, 2005). In this study, successful purification of Hpa1 from the membrane of *E. coli* (Figure 3.4) indicates that membrane binding is a characteristic of Hpa1 *in vivo*. Sucrose gradient centrifugation revealed that Hpa1 can bind liposomes at pH 6.0 and 6.5 *in vitro* (Figure 3.14). TEM observation also indicated that liposomes are disrupted by Hpa1 at these pHs (Figure 3.15 D, E and F). These results together with fluoresce studies that revealed the location of Hpa1-GFP (localized Hpa1 at the plasma membrane, communication with Prof. Gongyou Chen, Nanjing Agricultural University, China) suggest Hpa1 localizes to and disrupts the membrane. More discussion about function of Hpa1 in TTSS of *Xanthomonas* will be given in Section 6.1.2.

3.9.6 Crystallization of Hpa1 and harpin proteins

Harpin protein crystallography is still a challenge, as no harpin structure has been determined until now after their discovery in 1992 (Wei *et al*., 1992). In this work, only 1000 commercial screening conditions have been screened in the Hpa1 crystallography, but no crystal were formed from these conditions. Although needles or spherulites of Hpa1 (Figure 3.16) were successfully grown in self-prepared buffer, it was not reproducible and could not be optimized further.

More buffer conditions need to be screened for Hpa1 crystallization. In addition, other commonly employed tactics, such as crystallization additives, small molecules

known to bind harpin and limited proteolysis, could be tried for harpin crystallography. The higher percent of unordered structure of Hpa1 (Section 3.6) could be a reason for the difficulties in the crystallization and the method to improve the folding of Hpa1 could be beneficial in crystallization. The other factor in Hpa1 crystallization is the pH-dependent fibril formation of Hpa1 (Figure 3.7), which makes the selection of pH range critical to get the crystals.

Chapter 4 Fibril formation domain study of Hpa1

HpaG, the harpin of *X. axonopodis* pv glycines, was reported to have two predicted α-helical domains in the N- and C-terminal regions, and a Gln and Gly repeated sequence (QGQGQGQGG) (Figure 4.1), which is located between the two α helices and homologous to the prion-forming domain (PrD) of yeast prion protein (Oh *et al.*, 2007). The N-terminal α-helix region was found to be essential for inducing HR and fibril formation (Oh *et al.*, 2007). A single amino acid change of this region from leucine to proline abolished HR induction and fibril formation (Oh *et al.*, 2007).

In this chapter, I report the N-terminal α-helix region truncated Hpa1 (55-138) is sufficient for amyloid fibril formation, different from HpaG. The synthesized poly-peptide (ASPLTQMLMNIVGEILQAQ), corresponding to the C-terminal α-helix region, is responsible for fibril formation. The fibrils formed by the N-terminal α-helix region of truncated Hpa1 and a synthesized poly-peptide could damage membranes by analogy to full length Hpa1. The N-terminal α-helix region interacts with the C-terminal one and inhibits its fibril formation.

4.1 Amino acid sequence alignment of Hpa1 and HpaG, and secondary structure prediction

In order to study the domains of Hpa1, sequences of Hpa1 and HpaG were aligned using Vector NTI advance 10 (Invitrogen) and secondary structures of Hpa1 and HpaG were predicted by HNN secondary structure prediction method (Whitmore and Wallace, 2004 and 2008).

Hpa1 and HpaG show 59.7% identity. Hpa1 has N- and C-terminal α-helices and one GGGQGGNQQ domain between them (Figure 4.1 and 4.2). Hpa1 has one cysteine amino acid located in the N-terminal α-helix domain (Figure 4.1).

```
     1                                                            50
     ccccccccccc ccccceeeccc ccccccccccc ccccccchhhh hhhhhhhhhh
Hpa1 MNSLNTQFGG SASNFQVDQS QNAQSDSSQG SNGSQGISEK QLDQLLCQLI
HpaG MNSLNTQLGA NSSFFQVDPG QNTQSSPNQG N...QGISEK QLDQLLTQLI
     Ccccccccecc cceeeeeccc ccccccccccc c   ccchhh hhhhhhhhhh

     51                                                          100
     hhhhcccccc ccccccccccc ccccccccccc ccccccchhh   hhhhhhhhh
Hpa1 QALLQPNKNA EEGKGQQGGE NGGGQGGNQQ AGKENGASP. .LTQMLMNIV
HpaG MALLQQSNNA EQGQGQGQGG DSGGQGGNPR QAGQSNGSPS QYTQALMNIV
     hhhhhhcccc ccccccccccc ccccccccccc ccccccccccc hhhhhhhhhh

      101                                       139
      hhhhhhhccc ccccccccccc ccccccchhhc ccccccccc
Hpa1  GEILQAQNGG GAGGAGGSSG GDFGGSFASS FSNDSGSMQ
HpaG  GDILQAQNGG GFG...GGFG GGFGGILVTS LASDTGSMQ
      hhhhhhhccc ccc   cccc ccccceeeeee ecccccccc

 Alpha helix(h),Extended strand (e),Random coil(c)
```

Figure 4.1 Amino acid sequence alignment between Hpa1 and HpaG, and their protein secondary structure predictions. Hpa1 and HpaG display 59.7% identity, and identical residues are underlined, while alpha helix indicated with h, extended strand indicated with e, and random coil indicated with c; the alpha helix, extended strand and radom coil content of prediction of Hpa1 and HpaG are h (29%), e (2%), c (69%) and h (27%), e (10%), c (63%), respectively.

4.2 Cloning, over-expression and purification of N-terminal truncated Hpa1

In order to study the function of two helical domains in Hpa1, different constructs to truncate the N-terminal and C-terminal helical domains (Figure 4.2) were made.

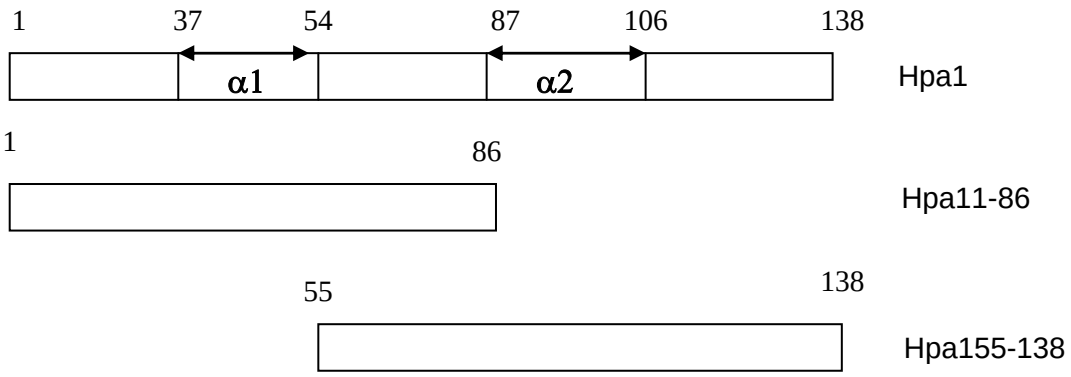

Peptide 1(α1 domain of Hpa1): ISEKQLDQLLCQLIQALL
Peptide 2 (α2 domain of Hpa1): ASPLTQMLMNIVGEILQAQ

Figure 4.2 Schematic representation of Hpa1 domains and synthesized peptides.

4.2.1 Cloning of truncated *hpa1* into pET21a expression vector

The truncated *hpa1* genes (1-258 and 163-414) were amplified by PCR from pET21a/*hpa1* with primer pairs *NdeI*- *hpa1* Forward and *XhoI*- 1-258-*hpa1* Reverse, *NdeI*-163-414-*hpa1* Forward and *XhoI*- *hpa1* Reverse, respectively (Table 2.3). The amplified truncated *hpa1* genes (1-258 and 163-414) were extracted and purified from the agarose gel and ligated into the commercial T-A propagation vector, pGEM-T Easy. The ligation mixture was transformed into chemically competent *E. coli* NovaBlue. Positively identified recombinant clones were used in the following expression vector sub-cloning procedure. Plasmid DNA purified from recombinant colonies was digested with NdeI and XhoI to confirm the presence of inserted DNA. After restriction enzyme digestion of the vector with NdeI and XhoI, the resulting *hpa1* fragments were ligated into pET21a generating constructs to express the *hpa1*

1-258 and 163-414 genes with C-terminal His_6 tags. The two constructs were sequenced to guarantee the correct sequence as expected. The constructs were transformed into *E. coli* strain BL21(DE3) for overexperssion.

4.2.2 Over-expression and purification of N-terminal truncated Hpa1-His_6

2L Hpa1 (1-86) and (55-138) cells were grown and induced by 1 mM IPTG as described in Section 2.7.1. Cells were harvested and resuspended in buffer (20 mM Tris-HCl, 300 mM NaCl, 10% glycerol, pH 8.5). Cells were lysed by mechanical disruption (Section 2.7.2).

The soluble fraction containing Hpa1 (1-86) and (55-138) from 2 litres of culture was obtained by differential centrifugation (Section 2.7.2) and purified by metal affinity chromatography using Ni^{2+} agarose (Section 2.7.2).

The packed column was washed with 10 ml of 20 mM Tris-HCl pH 8.5, 300 mM NaCl, 10% glycerol, 50 mM imidazole. Protein was eluted from the column using buffer A containing 500 mM imidazole. We failed to purify Hpa1 (1-86), as it aggregated and blocked the column during purification. In addition, there was no Hpa1(1-86) purified from *E. coli* membrane. Soluble Hpa1(55-138) (N-terminal 54 residue truncated) was purified successfully by the following procedure.

Hpa1 (55-138) purified by metal affinity chromatography was loaded onto a gel filtration Hiload 16/60 superdex 200 column (GE Healthcare), preequilibrated with 3 column volumes of buffer, for further purification. Figure 4.3 shows the elution profile of Hpa1-His_6 on a Hiload 16/60 superdex 200 prep grade size-exclusion column. Hpa1 (55-138) has low UV280 absorbance as there is no Trp or Tyr in truncated Hpa1 (55-138). Figure 4.4 lane 1 shows the efficiency of expression and purification of Hpa1-His_6 on an SDS-PAGE gel. The predicted molecular weight of Hpa1 (55-138) is 8343.51 Da (Vector NTI advance 10, Invitrogen). A His_6-tag western blot (Section 2.7.6) was carried out to confirm the correct expression and purification of Hpa1 (55-138). Figure 4.4 lane 3 shows the western blot of Hpa1 (55-138).

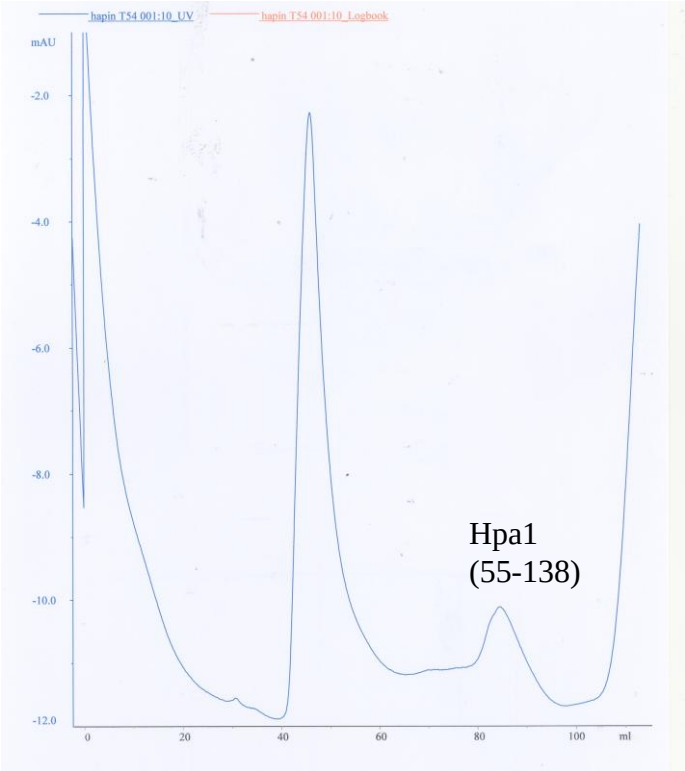

Figure 4.3 The elution chromatography profile of Hpa1 (55-138) from a Hiload 16/60 superdex 200 prep grade size-exclusion column.

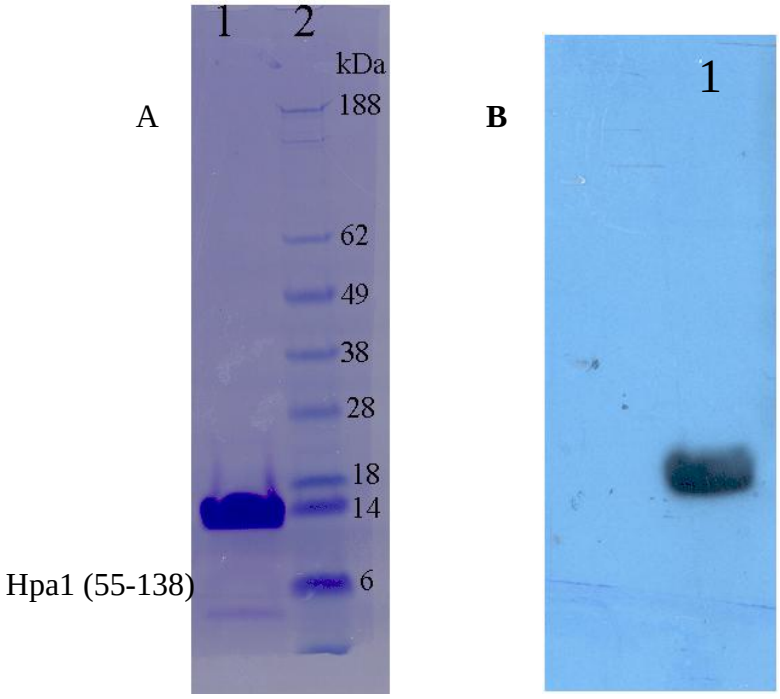

Figure 4.4 SDS-PAGE and western blot of Hpa1 (55-138). (A) Lane 1 shows the purified Hpa1 (55-138); Lane 2 M_r marker; (B) Lane 1 is the western blot signal of Hpa1 (55-138) corresponding to lane 1 in A.

4.3 Amyloid fibrils formed by Hpa1 (55-138)

In order to study the fibril forming ability of Hpa1 (55-138), the purified protein was diluted into pH 8.0 buffer containing 20 mM Tris-HCl, 50 mM NaCl, and pH 6.5 buffer containing 20 mM MES, 50 mM NaCl to give a final protein concentration of 40 μM, respectively. Samples were immediately observed by TEM after dilution of the Hpa1 (55-138) in each buffer. Purified Hpa1 (55-138) formed fibrils at pH 8.0 and pH 6.5. Hpa1 (55-138) might form fibrils in the process of protein preparation or TEM sample preparation. After incubation of Hpa1 (55-138) at each buffer for 1 day at room temperature (RT), the morphologies of the Hpa1 (55-138) fibrils were observed under TEM again. The Hpa1 (55-138) fibrils had about 10 nm width at pH 6.5. In conclusion, Hpa1 (55-138) forms fibrils at acidic and basic pHs (Figure 4.5).

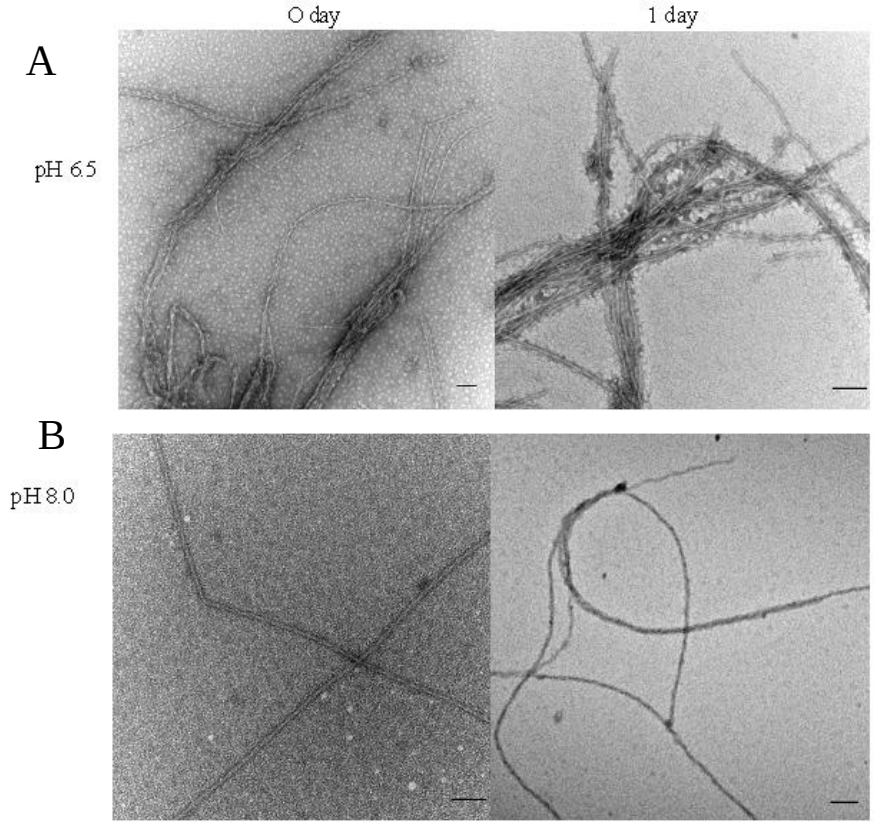

Figure 4.5 Negative-staining electron microscopy of fibrils forming of N-terminal truncated Hpa1 (55-138). (A) Fibril formation of 40 μM Hpa1 (55-138) in 20 mM MES (pH 6.5) and 20 mM NaCl, 0 day and 1 day, repectively. (B) Fibril formation of 40 μM Hpa1 (55-138) in 20 mM Tris-HCl (pH 8.5) and 20 mM NaCl, 0 day and 1 day, respectively. The time point 0 h is defined as the moment immediately following dilution of the protein in each buffer. (Scale bar = 100 nm).

4.4 Membrane lysis by Hpa1 (55-138)

Full length Hpa1 could damage the membranes prepared from *E. coli* lipid extraction (Section 3.7). Membrane disruption might be an important characteristic of amyloid fibrils that contributes to the toxicity of these fibrils. Liposomes were prepared as described in section 2.13. Purified Hpa1 (55-138) was mixed with the liposomes and incubated at RT for 1 day. The mixture of liposome and purified Hpa1 (55-138) were loaded onto carbon coated grids and stained with 1% uranyl acetate. TEM observation shows Hpa1 (55-138) could lyse the liposomes as did full length Hpa1 (Figure 4.6).

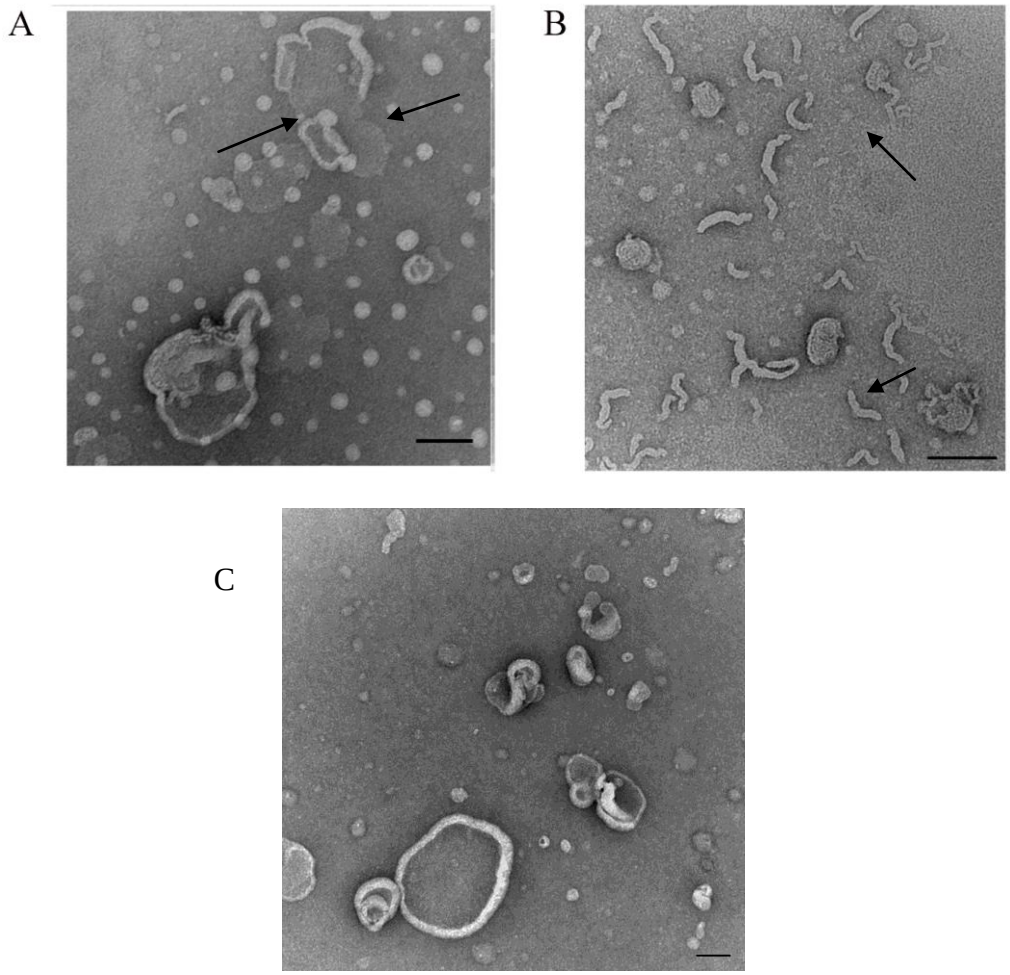

Figure 4.6 Liposomes lysed by Hpa1 (55-138). A and B, Liposomes lysed by Hpa1(55-138); C, the intact liposome control. Scale bar = 100 nm. Black arrows point to the disrupted liposomes.

4.5 Amyloid fibrils formed by peptides

In the study of HpaG, the N-terminal α-helix domain was synthesized and found to be the domain responsible for fibril formation (Oh *et al*., 2007). One site located in this N-terminal α-helix was thought to be the functional site, the mutation of which blocked fibril formation (Oh *et al*., 2007). Similar fibril forming peptides have been found in Alzeimer's β-amyloid peptides, Human amylin, and yeast prion sup35. Hpa1 has two α-helix domains located at the N- and C-terminus. In this study, the N-terminal and C-terminal α-helix domains were synthesized and nominated as peptide 1 and 2, respectively (Figure 4.2).

The ability of peptide 1 and peptide 2 to form amyloid fibrils at different pHs was tested. Peptide 1 and peptide 2 were dissolved in different buffers at pH 6.5, 7.0 and 8.0. The TEM observation was performed immediately after dilution to show the morphology of the peptide 1 and 2 in each buffer condition, or after 1 day incubation at room temperature (Figure 4.7). Peptide 1 could not form fibrils at any pH (Figure 4.7A). In contrast, peptide 2 formed fibrils at pH 6.5, 7.0 and 8.5 (Figure 4.7 B and C). These fibrils are straight with about a 12nm width, different from those formed by Hpa1-His_6 (Figure 3.7 B, C, E and F) and Hpa1-His_6 (55-138) (Figure 4.5). They clearly have 3 stands of protofibrils twisted together to form a mature fibril, as shown in Figure 4.7 B.

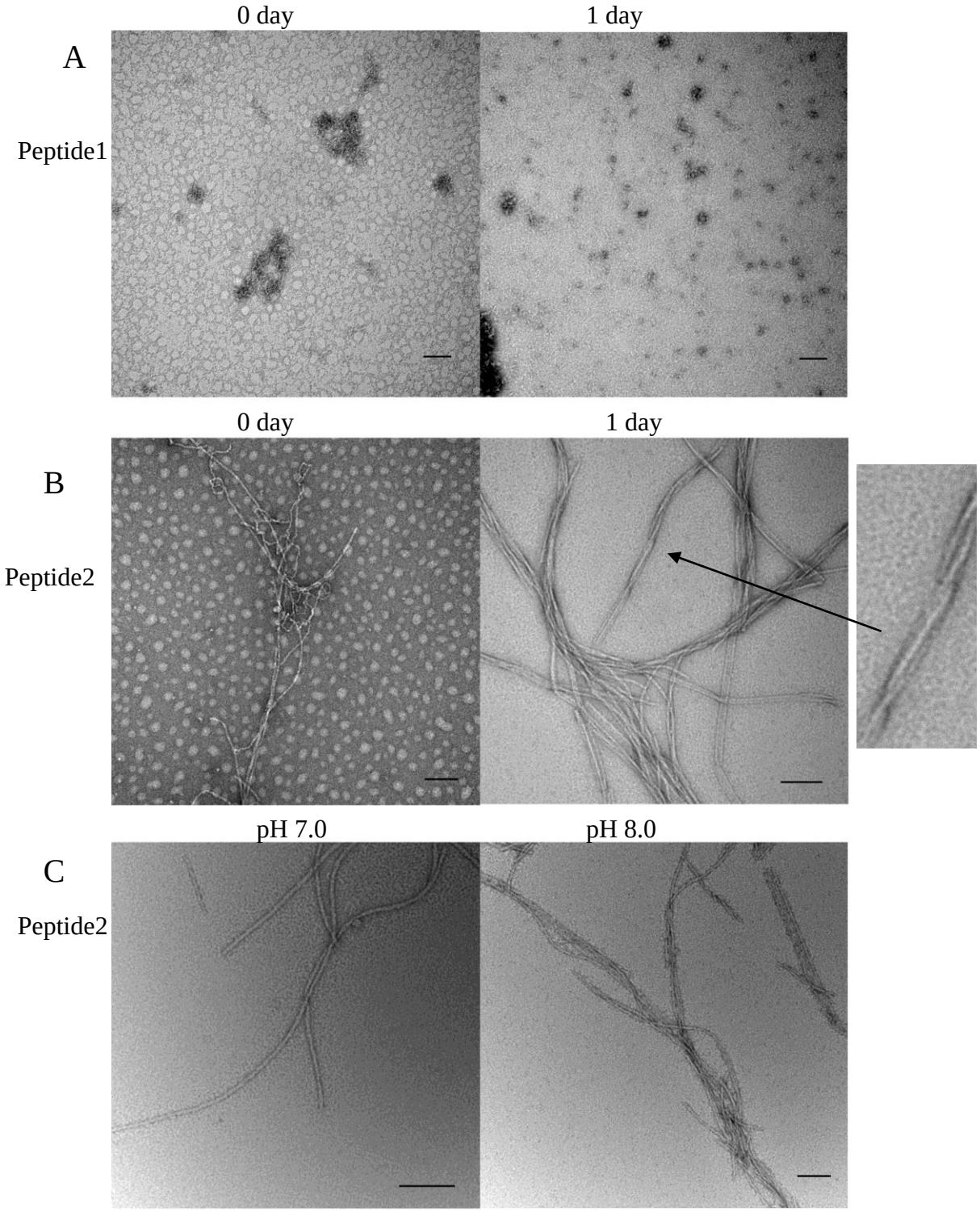

Figure 4.7 Negative-staining electron microscopy of fibril formation of peptide 1 and peptide2 of Hpa1. (A) 40 μM peptide 1 of Hpa1 in buffer (20 mM MES, pH 6.5 and 20 mM NaCl), at 0 day and 1 day, respectively. (B) The fibril formation of 40 μM peptide 2 of Hpa1 in 20 mM MES (pH 6.5) and 20 mM NaCl at 0 day and 1 day. The mature fibrils twisted by 3 strands of protofibrils shown in the amplified figure. (C) The fibril formation of 40 μM peptide 2 of Hpa1 in 20 mM MES (pH 7.0), 20 mM NaCl, and 20 mM Tris-HCl (pH 8.0), 20 mM NaCl. The time point 0 h is defined as the moment immediately following dilution of the protein in each buffer. (Scale bar = 100 nm)

4.6 Membrane lysis by peptides

Full length Hpa1 and Hpa1 (55-138) assemble into fibrils and damage the liposomes prepared from *E. coli* lipids (Section 3.7 and 4.4). Membrane disruption could be an important characteristics of amyloid fibrils that contributes to the toxicity of these fibrils. Liposomes were prepared as described in section 2.13. 50 μM peptide 2 was mixed with 5 mg liposomes and incubated at RT for 1 day. The mixture of liposome and peptide 2 were loaded onto carbon coated grids and stained with 1% uranyl acetate. Compared with the control, intact liposomes (Figure 4.6 C), TEM observation shows peptide 2 could lyse liposomes as did full length Hpa1 and Hpa1 (55-138) (Figure 4.8). Fibrils formed by peptide 2 were also visible (white arrows point to fibrils in Figure 4.8).

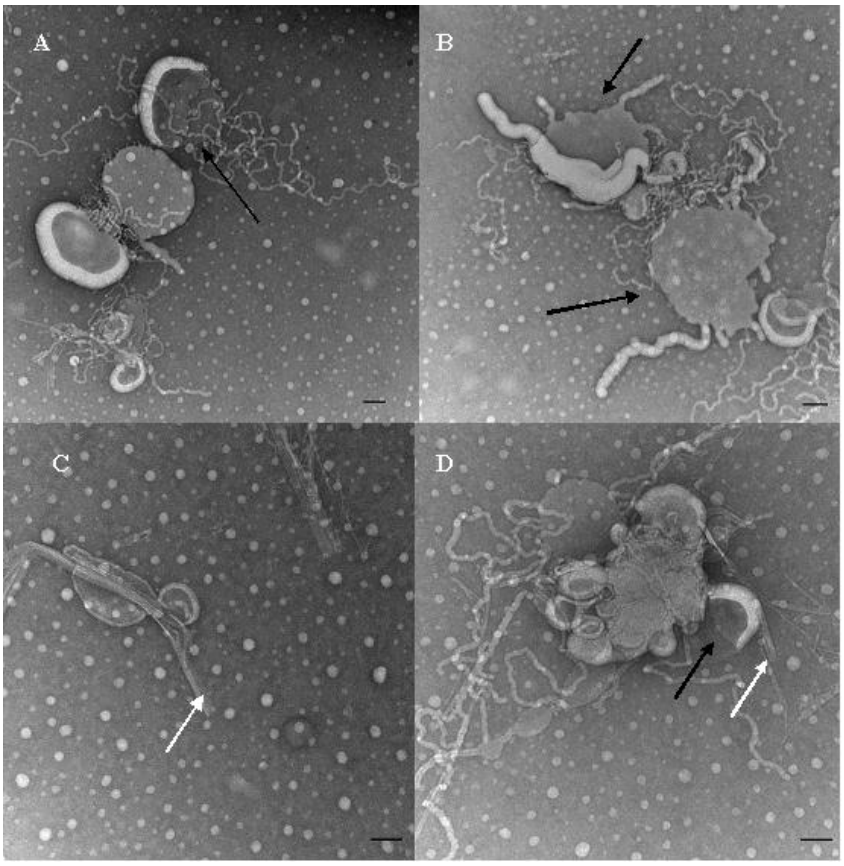

Figure 4.8 Liposomes lysed by fibrils formed by peptide 2 A, B, C and D, Liposomes lysed by fibrils formed by peptide 2 of Hpa1 at 20 mM MES (pH 6.0) and 20 mM NaCl, the white arrows point to the fibrils and the black arrows point to the broken liposome. (Scale bar = 100 nm)

4.7 Circular dichroism spectroscopy

Amyloid fibrils have a β-sheet rich structure. In order to study the secondary structure of Hpa1 (55-138) and peptide 2 during fibril formation, CD spectroscopy was performed. In order to minimize the strong absorbance from Cl^- in the far UV region, the buffer of Hpa1 (55-138) and peptide 2 was changed to Tris-base or NaH_2PO_4, with NaF as salt. All CD spectra were analyzed using the software Dichroweb online (Whitmore and Wallace, 2004 and 2008).

Truncated Hpa1 (55-138) has a high percentage of sheet structure at both pH 8.0 and 6.5, of 28.3% and 38.3%, respectively (Figure 4.9 A), which are fibrils under TEM (Figure 4.5). These CD spectra data combined with TEM results suggest that the fibril formed by Hpa1 (55-138) are beta sheet rich structures.

In the CD study of peptide 2, at pH 8.5, peptide2 has 15.5% helix, 43.6% sheet, 12% turn, and 28.9% unordered structure (Figure 4.9 B). After 30 min incubation at pH6.5, peptide 2 has 40.6% helix structure, 16.9% sheet structure, 22.2% turn structure and 21.3% disordered structure (Figure 4.9 C).

In conclusion, both the fibrils formed by Hpa1 (55-138) and by peptide 2 have sheet rich structures, but, in each case, not all the secondary structure is β-sheet structure. Considering that peptides as short as 4 residues can form amyloid fibrils and their atomic structures only have β-sheet structure (Nelson *et al*., 2005; Kajava *et al*., 2007), peptide 2 is unlikely to be the minimal sequence in Hpa1 for fibril assembly.

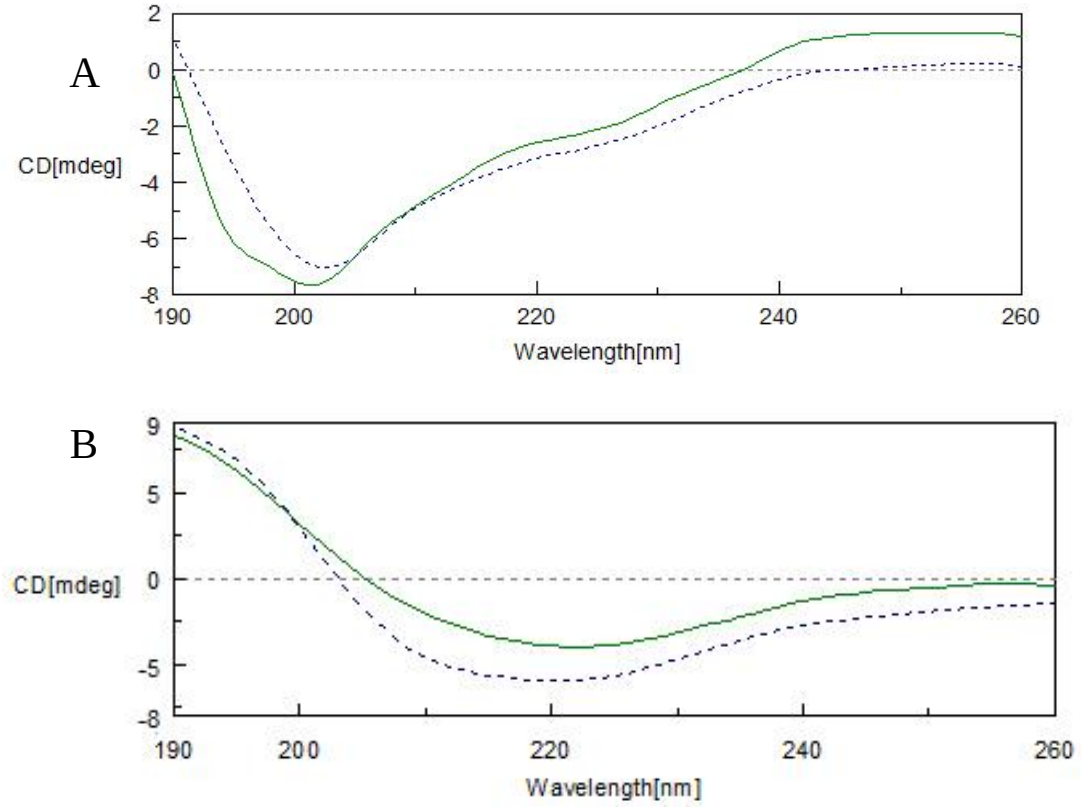

Figure 4.9 CD spectroscopic analysis of Hpa1 (55-138) at pH 8.0 and pH 6.5, peptide 2 at pH 8.0 and 6.5. (A) 5 µM Hpa1 (55-138) at pH 8.0 after 1 day incubation (solid line), 5 µM Hpa1 (55-138) at pH 6.5 after 1 day incubation (dotted line). (B) 10 µM peptide 2 at pH 8.0 (solid line), 10 µM peptide 2 at pH 6.5, 30 min (dotted line).

4.8 Intramolecular interaction of Hpa1

To study the possible intramolecular interaction of Hpa1, the effect of peptide 1 on peptide 2's fibril formation was tested. 40 µM peptide 1 and 40 µM peptide 2 were diluted into pH 6.5 buffer (20 mM MES, 50 mM NaCl), and co-incubated at room temperature for 1 day, after which the mixture was loaded onto carbon coated grids and observed under TEM (Figure 4.10A). Compared with Figure 4.7 B and C, peptide 2 cannot form fibrils in the presence of peptide 1. To rule out the low concentration of samples resulting in the absence of fibrils during observation, the concentrations of peptide 1 and peptide 2 were increased to 400 µM. After 1 day incubation at RT in pH 6.5 buffer (20 mM MES, 50 mM NaCl), the mixture was observed under TEM (Figure 4.10 B): no fibrils were observed, which indicates that peptide 2 cannot form fibrils in the presence of peptide 1.

The ability of peptide 1 to block fibril formation by the full length and N-terminal truncated Hpa1 was also tested. We found the fibrils formed by the full length and N-terminal truncated Hpa1 survived in the presence of peptide 1 under EM.

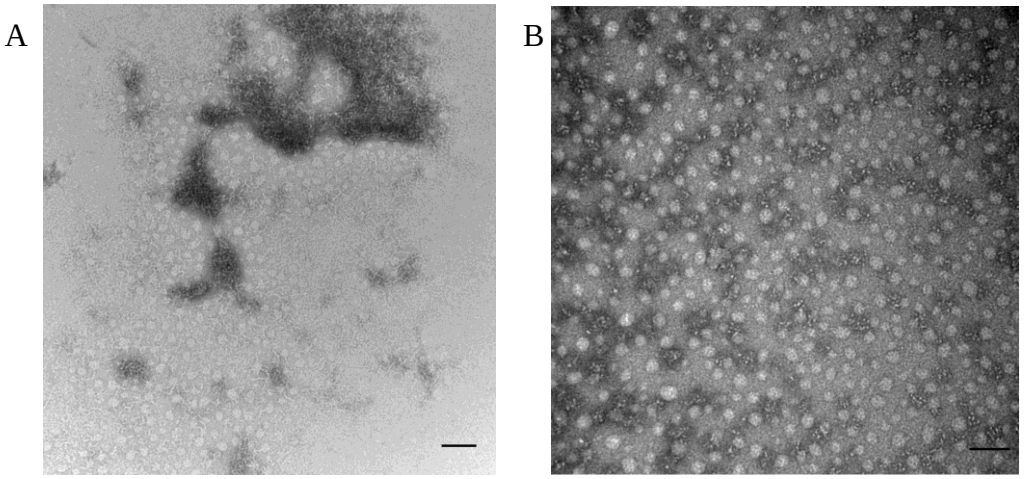

Figure 4.10 Intramolecular interaction of Hpa1 (A) 40 μM peptide 1 inhibited the fibrils formed by 40 μM peptide 2 in 20 mM MES (pH 6.5) and 20 mM NaCl. (B) 400 μM peptide 1 inhibited the fibrils formed by 400 μM peptide 2 in 20 mM MES (pH 6.5) and 20mM NaCl.

4.9 Discussion

Polypeptides from fibril formation precursor proteins are widely reported to be the segment responsible for the amyloid fibril formation (Table 1.2). They are the products after the protease digestion of full length protein, e.g. $A\beta_{40}$ and $A\beta_{42}$ peptide associated with Alzheimer's disease (Benzinger *et al.*, 2000), or the predicted α helix domains of full length precursors of amyloid fibril formation, e.g. the poly-amino acids from myoglobin (Fandrich *et al.*, 2001) and amyloid forming peptide of HpaG (Oh *et al.*, 2007). To obtain the segment of Hpa1 involved in amyloid fibril formation, we firstly truncated the N-terminus (1-54) of Hpa1 and then synthesized two predicted α-helical domains to localize the fibril forming segment.

4.9.1 Domains of Hpa1

To study the function of the two predicted α helix domains located at the N-terminus (37-54) and C-terminus (87-105) of Hpa1, truncated Hpa1 (1-86 and 55-138) was constructed and over-expressed (Figure 4.1 and 4.2). Hpa1 (1-86) failed to purify because of the blockage of the Ni-column, which is probably due to the aggregation of protein *in vitro*. *In vivo* fluorescence localization of Hpa1 (1-86) shows this domain is responsible for binding to plant plasma membranes (communication with Prof. Gongyou Chen, Nanjing Agricultural University). Hpa1 (55-138) functions as the domain for fibril formation (Figure 4.5). In contrast to the full length Hpa1, this segment forms fibrils at acidic and basic pH (Figure 4.5).

Even though HpaG and Hpa1 share 59.7% identity and similar secondary structures (Figure 4.1), they have different domains for fibril formation. The N-terminal α helix domain of HpaG forms fibrils (Oh *et al*., 2007), in contrast with the C-terminal α helix domain of Hpa1. This difference might indicate the evolution of harpins in *X. oryzae* pv. oryzicola and *X. axonopodis* pv glycines to fulfil their function in different hosts.

4.9.2 Fibril-forming peptide of Hpa1

Polypeptides, derived from the segment of precursor proteins for amyloid fibril formation have been widely studied to understand the mechanism for amyloid fibril formation, as the basis for designing new inhibitors in amyloid fibril associated diseases. The minimal length for amyloid fibril formation is a tetrapeptide, e.g. NNQQ of yeast prion protein Sup35 (Sawaya *et al.*, 2007). The C-terminal α helix domain, 19 amino acids (ASPLTQMLMNIVGEILQAQ), of Hpa1 forms fibrils at all pHs tested (Figure 4.7), which indicates that the fibrils formed by peptide 2 is pH-independent and an inherent characteristic of the sequence component.

CD spectrum analyses show fibrils formed by peptide 2 are a mixture of α helix and β sheet (Section 4.7). The secondary structure transition of peptide 2, recorded by CD, found high percentage of sheet (43.6%) at pH 8.5, but a high percentage of helix

structure (40.6%) at pH 6.5. A possible explanation is that the precipitation of mature fibrils at pH 6.5, which decreases the sheet structure content in the soluble state for CD spectrum. Further work will be required to re-construct the 3-D structure of the mature fibrils of peptide 2 by cryo-EM, and to establish the interaction between the 3 strands of protofibrils in the mature fibril assembly.

In addition, considering that the minimal segment for fibril formation is a tetrapeptide (Sawaya *et al.*, 2007; Tjernberg *et al*., 2002) and that the peptide Aβ(1-42) lacking residues 14-23 is not fibrillogenic (Tjernberg *et al*., 1999), the minimal segment of peptide 2 of Hpa1 for fibril formation could be determined in future work.

4.9.3 Membrane disrupted by fibrils

Several mechanisms have been proposed to explain the pathogenicity of amyloid fibrils, e.g. membrane disruption, ion channel formation and permeabilization of membranes (Engel *et al.*, 2008; Kayed *et al.*, 2004; Quist *et al.*, 2005). The intermediate state, soluble amyloid oligomers, has been assumed as the main cytotoxic species. The function of fibril formation of Hpa1 in the pathogenicity of *Xoc* on plants is still unclear.

In this study, the fibrils formed by the segment or polypeptide of Hpa1 could damage the membranes directly after mixing them (Figure 4.6 and 4.8). Engel *et al*., 2008 reported that the human islet amyloid polypeptide (IAPP) damaged the membrane through fibril growth on the membrane (Engel *et al.*, 2008). However, in this study, it is fibrils that damage the membrane, since the fibrils had already formed by Hpa1 (55-138) and peptide 2 of Hpa1 before mixing with liposomes (Figure 4.5, 4.5, 4.7 and 4.8). This direct function of membrane damage by the fibrils formed by Hpa1 raises the possibility that harpins not only trigger signal transduction to induce cell death (Alfano and Collmer, 2004) but also damage the cell membrane directly after being infiltrated into the intercellular space of nonhost leaves. Further work is required to support this hypothesis *in vivo*.

4.9.4 Intramolecular interaction of Hpa1

Peptide 2 (C-terminal α helix domain) of Hpa1 forms fibrils, whereas peptide 1 (N-terminal α helix domain) of Hpa1 can not assemble into fibrils (Figure 4.7). However, fibrils formed by peptide 2 of Hpa1 were disassembled by peptide 1 (Figure 4.10 A and B). These results suggest that the assembly of fibrils by Hpa1 requires the separation of the fibril forming domain (peptide 2 segment) from the N-terminal domain (peptide 1), which is consistent with the report that the intermolecular contacts and separation of regions from the N-terminal region of Sup35 are both required for fibril assembly (Krishnan and Lindquist, 2005). In addition, the presence of such domains in preventing fibril assembly provides clues to developing methods to prevent fibril assembly or dissemble preformed fibrils.

Chapter 5 Crystallization and preliminary structure analysis of the *Vibrio cholerae* VceR drug-pump repressor in complex with bound DNA

In this chapter, I report on the crystallization and structure analysis of VceR in complex with bound DNA. In optimizing the crystallization process, I have used different lengths and end designs of synthetic DNA oligonucleotides whilst purification of the protein/DNA complex was carried out to improve the diffraction power of the native VceR/DNA crystals. A native data set was processed to 3.15 Å. In phasing, anomalous scattering from Br labelled DNA and Se-Met substituted VceR was used. The positions of Se were located successfully by ShelxD and an interpretable electron density map was obtained. A preliminary model with one VceR dimer and an 11 bp base pair DNA duplex was built.

5. 1 VceR and QacR sequence alignment

VceR and QacR are both members of the TetR family of repressors (Borges-Walmsley *et al.*, 2005). It has been suggested that two dimers of VceR bind the 28 bp region of *vceCAB* operon, similar to the interaction of QacR with its cognate DNA (Borges-Walmsley *et al.*, 2005). To determine the sequence similarity of VceR and QacR, the VceR and QacR sequences were aligned with Vector NTI. QacR and VceR display 17.7% overall identity, but higher identity, 29.8%, in the DNA binding domain (α1-α3). Compared with QacR, VceR has an 8 amino acid insertion in the drug binding domain between helix 7 and helix 8 (Figure 5.1), which could reflect differences in the ligands bound. VceR also has 5 extra amino acids at the beginning of the N-terminus (Figure 5.1).

Figure 5.1 VceR and QacR sequence alignment and secondary structures. VceR and QacR display 17.7% identity, and identical residues are underlined. h shows α-helix structure of QacR (Schumacher *et al*., 2002; PDB code: 1JT0).

5. 2 Oligodeoxynucleotide preparation

To obtain VceR/DNA complex crystals, the operator sequence bound by VceR was studied (Borges-Walmsley *et al*., 2005) and the oligodeoxynucleotides from this study were ordered from MWG purified by HPSF (high purity salt free) purification. Purified P5 and P6 oligodeoxynucleotides were dissolved to a final concentration 1 mM in 10 mM $MgCl_2$, respectively. Equal volumes of these two corresponding oligodeoxynucleotides were mixed, placed in a heating block at 95^{o}C for two minutes and then allowed to cool to ambient temperature for annealing, which formed the duplex (Figure 5.2) at a concentration of 500 μM for crystallization.

30-mer with blunt end (P56):

5'-AG**TATAACT**GT**AC**G**GT**ACGGTTTAGTTATA-3'
3'-TCATATTGACATGCCA**TG**C**CA**AA**TCAATAT**-5'

Figure 5.2 P56 duplex used for VceR/dsDNA co-crystallization. The inverted repeats (IR) are shown in bold letters. (Borges-Walmsley *et al*., 2005).

5.3 VceR purification

VceR-His_6-pET21a(+) (Table 2.1) was transformed into BL21(DE3) for over-expression (Section 2.4.8). The over-expression of VceR-His_6 was achieved as described in Section 2.7.1 and purification was carried out as described in Section 2.7.2. The column was washed with buffer (50 mM Tris-HCl, 300 mM NaCl, 10% glycerol, 100 mM imidazole, 0.5 mM THP, pH 7.0) to remove contaminating proteins. The protein was eluted with buffer (50 mM Tris-HCl, 300 mM NaCl, 10% glycerol, 500 mM imidazole, 0.5 mM THP, pH 7.0). 20 µl aliquots of the VceR-His_6 protein (23.4 kDa) were run out on a 12% SDS-PAGE gel (Figure 5.3).

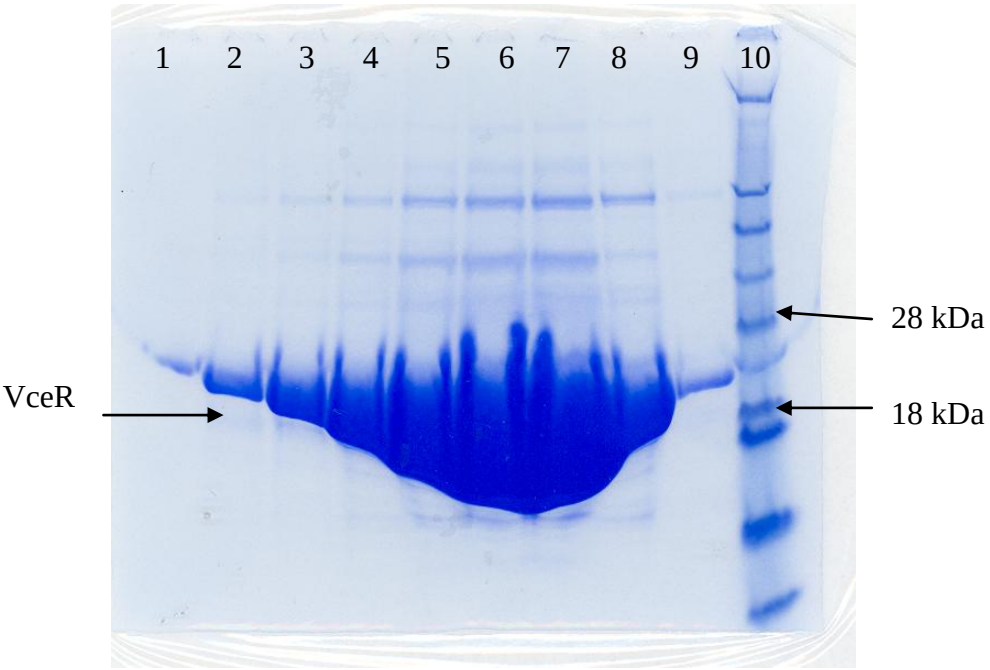

Figure 5.3 A Coomassie blue stained SDS-PAGE gel of VceR-His_6 (23.4 kDa) purified by Ni^{2+} affinity chromatography. Lane 1-9: VceR-His_6. Lane 10: See blue marker (Invitrogen) in MES buffer

VceR-His_6 was further purified using a Hi-load 16/60 Superdex 200 prep grad column (GE Healthcare) according to the protocol described in Section 2.5.3 (Figure 5.4). 20 µl aliquots of the VceR purified from the gel filtration chromatography were run out on a 12% SDS-PAGE gel (Figure 5.5).

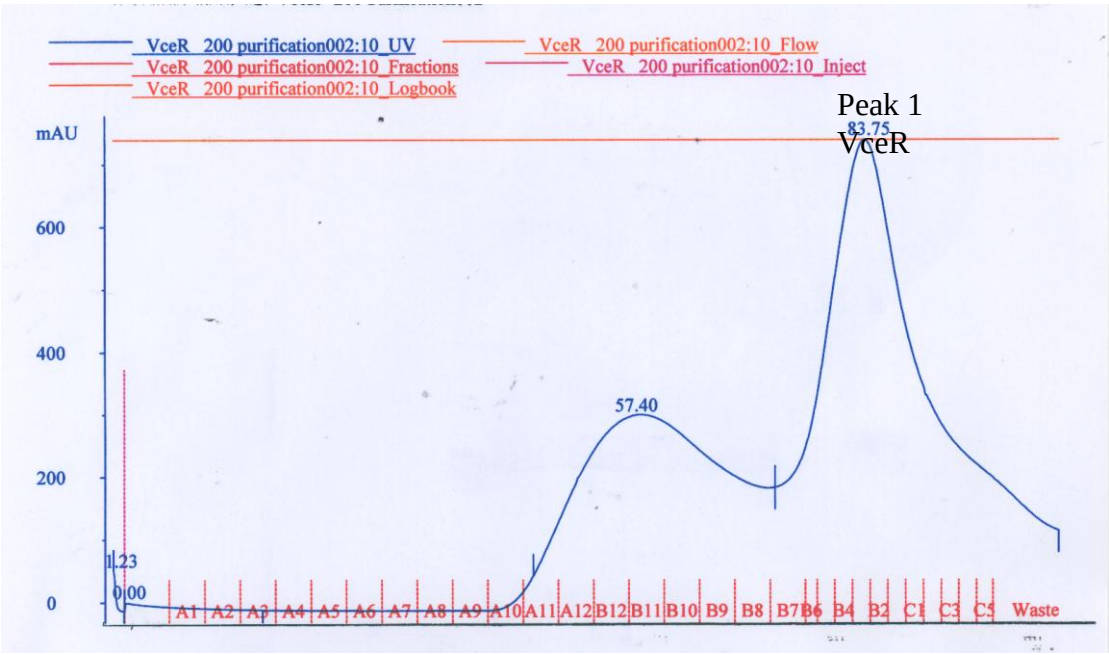

Figure 5.4 The elution chromatography of VceR-His_6 from a Hi-load 16/60 Superdex 200 prep grad column.

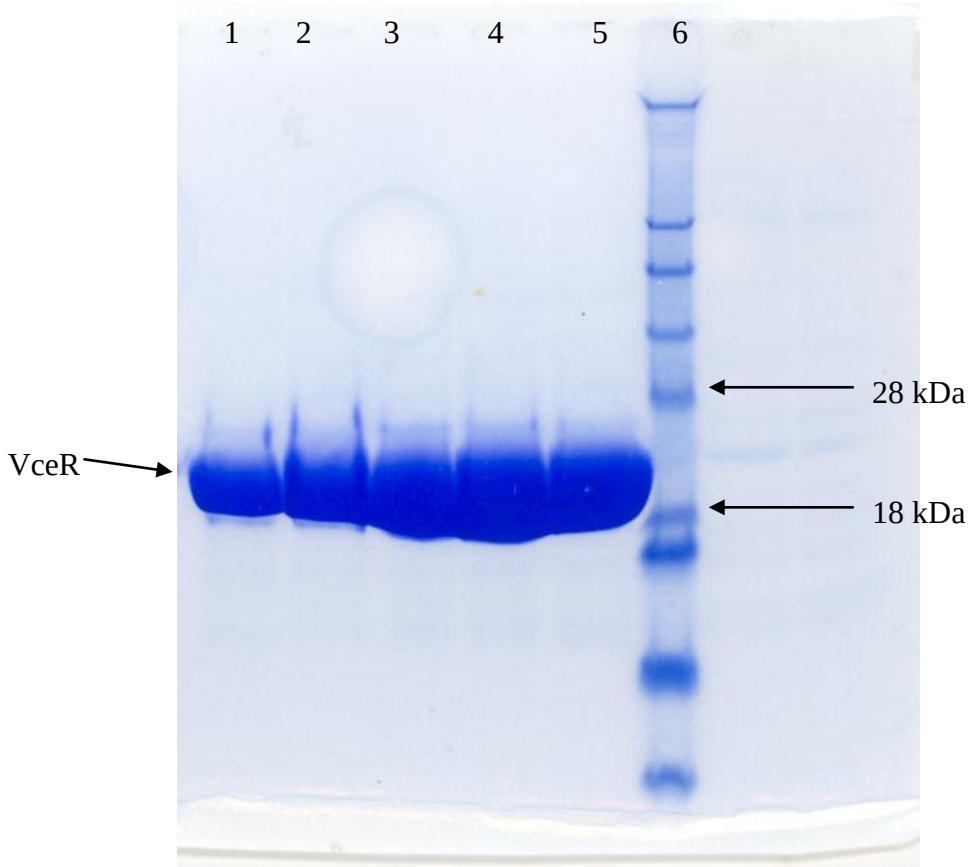

Figure 5.5 A Coomassie blue stained SDS-PAGE gel showing VceR-His$_6$ protein purified by size-exclusion chromatography. Lane 1-5 correspond to fractions from peak 1 in Figure 5.4. Lane 6: See blue marker (Invitrogen) in MES buffer

5.4 Crystallization of VceR/dsDNA

Initial crystallization trials of VceR/dsDNA complex were performed by Dr. David Albesa-Jove and Beth Ashbridge (Department of Chemistry, University of Durham). The P56 duplex (Figure 5.2) was used in their study. In their experiments, 2 M ammonium phosphate, 100 mM Tris-HCl at pH 8.5 (The Classics Suite, 27, Qiagen), was used to obtain crystals, which were taken as seeds in 1 M ammonium phosphate, 100 mM Tris-HCl at pH 8.5 (The Classics Lite Suite, 27, Qiagen) to grow larger-sized crystals. Figure 5.6 shows the optimization procedure used in this study to obtain a 3.15 Å native data set.

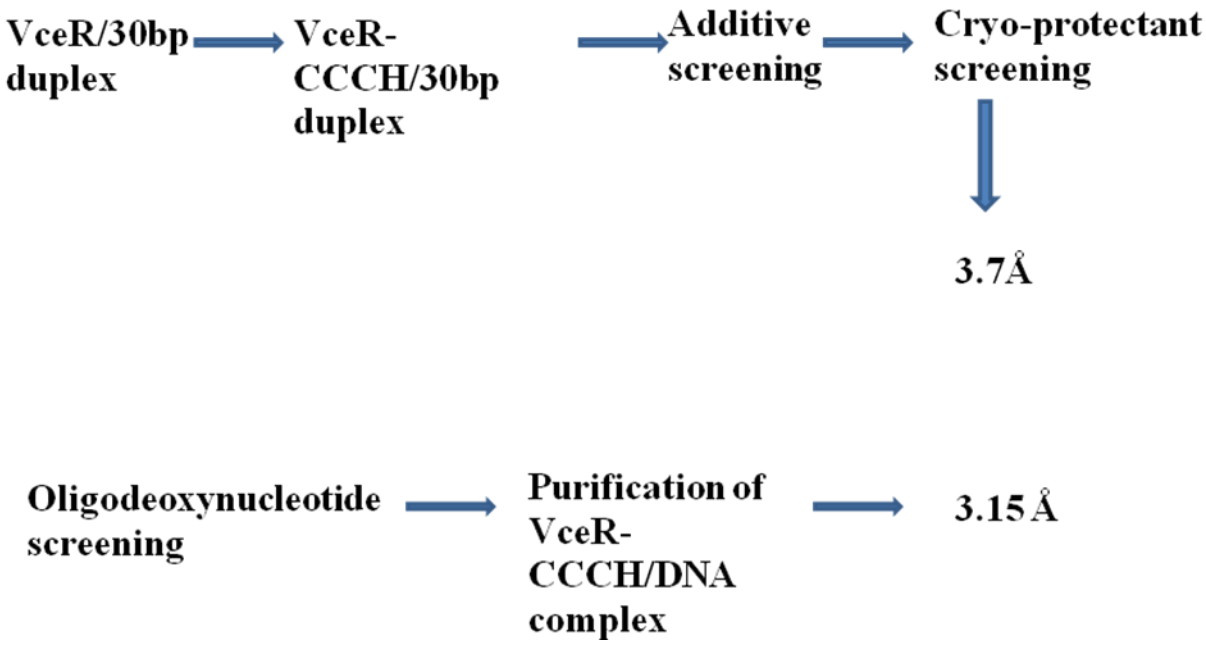

Figure 5.6 The optimization procedure to obtain a 3.15 Å native data set.

According to a crystallization product report (Qiagen), the pH of the crystallization buffer used by Dr. David Albesa-Jove (2 M ammonium phosphate, 100 mM Tris-HCl at pH 8.5) is 4.01 and that of 1 M ammonium phosphate, 100 mM Tris-HCl at pH 8.5 is 4.7. In my work, the crystallization conditions around these were screened (Table 5.1 and 5.2). Tris-HCl was used as the buffer to adjust the pH of the crystallization condition. However, in this condition, 1-2 M of ammonium hydrogen phosphate changes the final pH dramatically and 0.1 M Tris-HCl loses its control over the pH. In ammonium phosphate and pH screen II, Tris-HCl was not used. Under buffer conditions B1, B2, B3, B4, C1, C2 and C3 of Table 5.1, and E1, E2, E3, F1, F2, F3, G1and G2 of Table 5.2, the VceR/dsDNA complex could form crystals. As a control, VceR cannot form crystals in these conditions (Figure 5.7 A). For the best diffracting crystals with this pair of oligos, the drop consisted of 1µl 10 mg/ml VceR/dsDNA (the molar ratio of VceR monomer : dsDNA= 2:1 for mixing before crystallization) in 50 mM MES, 200 mM KCl, 4 µM DTT at pH 7.0, plus 2µl of well solution, which was 1 M ammonium phosphate, at pH 4.05.

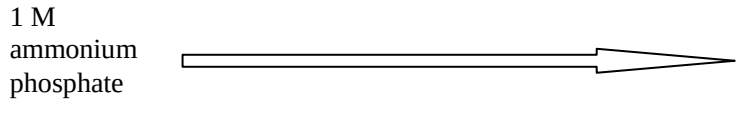

pH 3.8 ⇩ pH 4.4						
	A1	A2	A3	A4	A5	A6
	B1	B2	B3	B4	B5	B6
	C1	C2	C3	C4	C5	C6
	D1	D2	D3	D4	D5	D6

Table 5.1 Ammonium phosphate and pH screen I

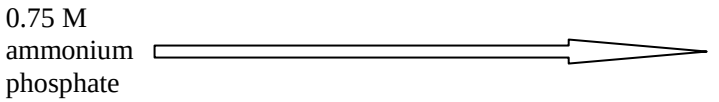

pH 4.0 ⇩ pH 4.3						
	A1	A2	A3	A4	A5	A6
	B1	B2	B3	B4	B5	B6
	C1	C2	C3	C4	C5	C6
	D1	D2	D3	D4	D5	D6

Table 5.2 Ammonium phosphate and pH screen II

In order to optimize the crystallization conditions, different methods, such as low temperature, adding silicon oil to the drop and decreasing the concentration of protein, were tried to decrease the evaporation speed and nucleation forming in drops. The incubation at 4^{o}C was chosen after comparison with drops from 20^{o}C (Figure 5.7 B and 5.7 C). The low temperature not only decreases the evaporation speed, but also increases the stability of protein in the drops, resulting in larger crystals (Figure 5.7 B and 5.7 C).

Micro-seeding was also used to grow bigger crystals in this study. The crystals in Figure 5.7 B were taken as the seeds and transferred into new drops containing 2 μl 10 mg/ml VceR/dsDNA (the molar ratio of VceR monomer: dsDNA = 2:1) in 50 mM MES, 300 mM KCl, 4 μM DTT at pH 7.0, plus 4 μl of well solution, which was a solution of 100 mM Tris-HCl, 1 M ammonium phosphate, at pH 4.05. However, the diffraction power of the resulting crystals was not improved by seeding.

For the additive screening (Section 2.15), additive 10, (0.1 M $ZnCl_2$) (Figure 5.7 D) and 53 (10% PEG3350) (Figure 5.7 E) gave much larger crystals and were selected for the subsequent crystallization optimization.

5.5 Crystallization of VceR-CCCH/dsDNA

In the crystallization of QacR, cysteines were mutated to serines to prevent serious cross-linking and oxidation problems observed in the wild-type protein (Schumacher, *et al.*, 2002). In this study, cysteine 138, 142, 148 and histidine 156 were mutated to serine, serine, serine, and arginine, for crystallization and structure analysis. The site directed mutagenesis of pET21a-VceR was performed as described in Section 2.6. The mutagenic primers *vceR*-C148S-Forward and *vceR*-C148S-Reverse were used as detailed in Table 2.4. The pET21a-*vceR* ds-DNA was used as the template. Mutant strand synthesis using PCR was achieved with an extension time of 6 minutes. The clones were sequenced to ensure the correct was selected mutant. Then, VceR-C148S was used as the template and the primers *vceR*-C138S-C142S-Forward and *vceR*-C138S-C142S-Reverse (Table 2.6, primers designed by Dr. M. Ines Borges-Walmsley) were utilized to get VceR-C138, 142, 148S. Finally, the correct VceR-C138, 142, 148S was used as the template and the primers *vceR*-H156R-Forward and *vceR*-H156R-Reverse (Table 2.6, primers designed by Dr. M. Ines Borges-Walmsley) were utilized to get the VceR-CCCH derivative. After sequencing, the correct clones were transformed into BL21(DE3) for over-expression.

Purification of the VceR-CCCH derivative was performed as for VceR in Section 5.3. The VceR-CCCH/DNA crystallization was performed as for VceR/DNA. Figure 5.7 F shows crystals formed by VceR-CCCH/dsDNA (P56) in the presence of PEG3350 at 4 ^{o}C.

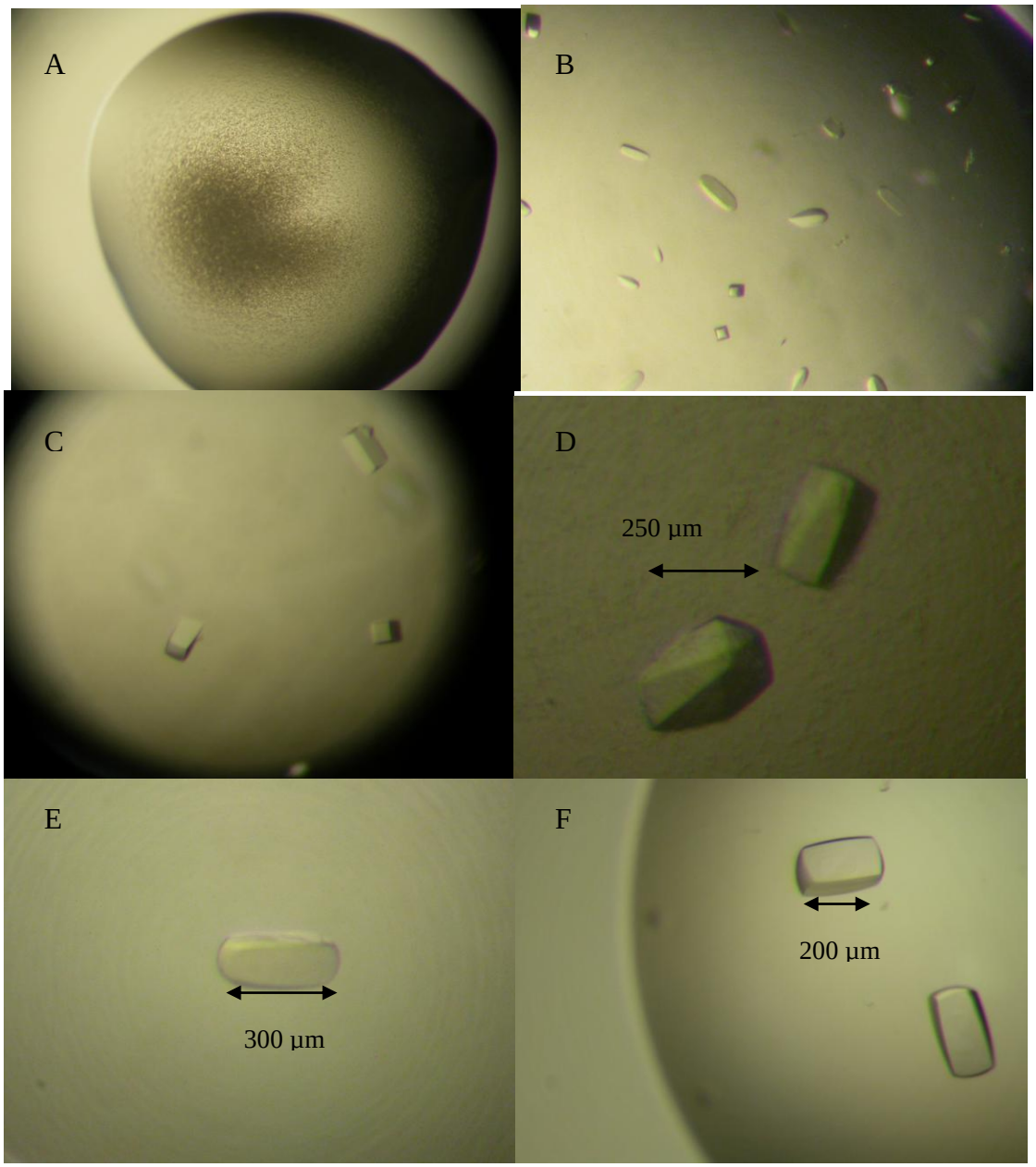

Figure 5.7 Crystals formed by VceR or VceR-CCCH in complex with the DNA duplex P56 (A) VceR-His_6 precipitated in crystallization buffer (1 M ammonium phosphate, pH 4.0). (B) Crystals of VceR/dsDNA (P56) from the condition (1 M ammonium phosphate, pH 4.0), at 20^{o}C. (C) Crystals of VceR/dsDNA (P56) from the condition (1 M ammonium phosphate, pH 4.0), at 4^{o}C. (D) Crystals of VceR/dsDNA (P56) formed in the presence of Zn^{2+} at 4^{o}C. (E) Crystals of VceR/dsDNA (P56) formed in the presence of PEG3350 at 4^{o}C. (F) Crystals of VceR-CCCH/dsDNA (P56) formed in the presence of PEG3350 at 4 ^{o}C.

5.6 Crystal freezing and X-ray diffraction tests

To freeze the crystals for X-ray diffraction at 100 K, 30% MPD, 30% PEG400, 30% sucrose, 30% PEG3350, saturated ammonium phosphate and 30% glycerol were tested to find out if they provided suitable cryo-protection. However, according to diffraction tests, no significant differences were found in these cryo-protectants. 30% glycerol was chosen as the cryo-protectant. A typical diffraction pattern from the SLS is shown in Figure 5.8. The diffraction data are summarized in Table 5.3.

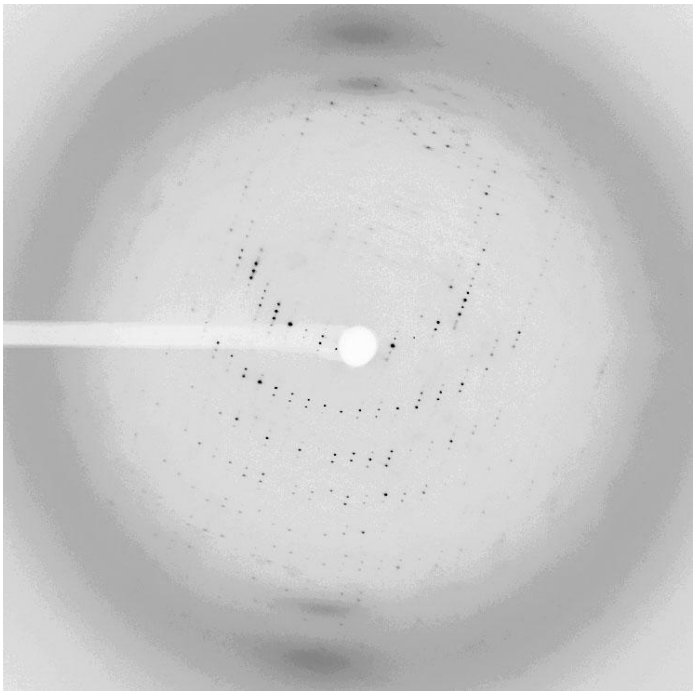

Figure 5.8 Diffraction pattern of VceR-CCCH/P56 at SLS beamline X06DA.

Proteins	dsDNA	Crystals	Diffraction limits
VceR	P56	150 μm in length, No additive	4 Å
VceR	P56	150 μm in lenth, additive $ZnCl_2$, (Figure 5.7D)	Crystals disappeared in the 30% glycerol as cryo-protectant.
VceR-CCCH derivative	P56	200 μm in length (Figure 5.7F), with additive PEG3350	3.7 Å
VceR-CCCH derivative	P56	280 μm in length, with additive $ZnCl_2$	4.3-6 Å

Table 5.3 Summaries of the diffraction limits for VceR/DNA crystals from P56 30 bp duplex DNA.

5.7 Oligodeoxynucleotide screening for diffraction quality improvement.

In protein/DNA complex crystallization, the length and construction of the DNA fragment and the nature of the terminal nucleotides should be considered in establishing conditions to form crystals of protein/DNA complexes and for improving the diffraction of protein/DNA complex (Aggarwal, 1990; Pohl *et al*., 1999).

The oligodeoxynucleotides used for VceR/dsDNA complex crystallization were the original from Borges-Walmsley *et al*., 2005 and further oligonucleotide screening was on the basis of P56 duplex (Figure 5.2). To improve the diffraction quality, different pairs of oligodeoxynucleotides were designed (Table 2.5).

P56-1 and P56-2 were designed to form 28 bp duplexes with a high order palindrome for VceR binding; P56-3 was designed as the 28 bp duplexes without site mutation from the original promoter sequence (P56); P56-4 was designed to form a 30-mer with one overhang; P56-5 was designed to form a 29-mer with one overhang; P56-6 was designed to form a 28-mer with two overhangs; P56-7 was designed to form a

31-mer with blunt ends. P56-24, P56-26, P56-27, were designed to form 24 bp, 26 bp and 27 bp length duplexes on the basis of P56-1. All these oligo pairs were shown in Table 2.5.

5.7.1 Purification of the VceR-CCCH/DNA complex

VceR-CCCH was purified as described previously (Section 5.3). Gel filtration purified VceR-CCCH was mixed with DNA (Table 2.5), and incubated at 4 ^{o}C for 1 hour. The mixture of VceR-CCCH and oligos were loaded onto a Hiload 16/60 superdex 200 gel filtration column, pre-equilibrated with buffer (25 mM MES, 200 mM NaCl, 6 mM DTT, pH 7.0) for protein/dsDNA complex purification. The VceR/DNA complex has an elution volume of 68.02 ml, in contrast to 80 ml for the VceR dimer on the same column (Figure 5.9). In addition, the 260/280 nm ratio, 1.7, for VceR/DNA complex, indicated the formation of VceR/DNA complex, which is 2 for pure DNA and 1.2 for VceR. The purified complex was concentrated to 10 mg/ml for crystallization screening.

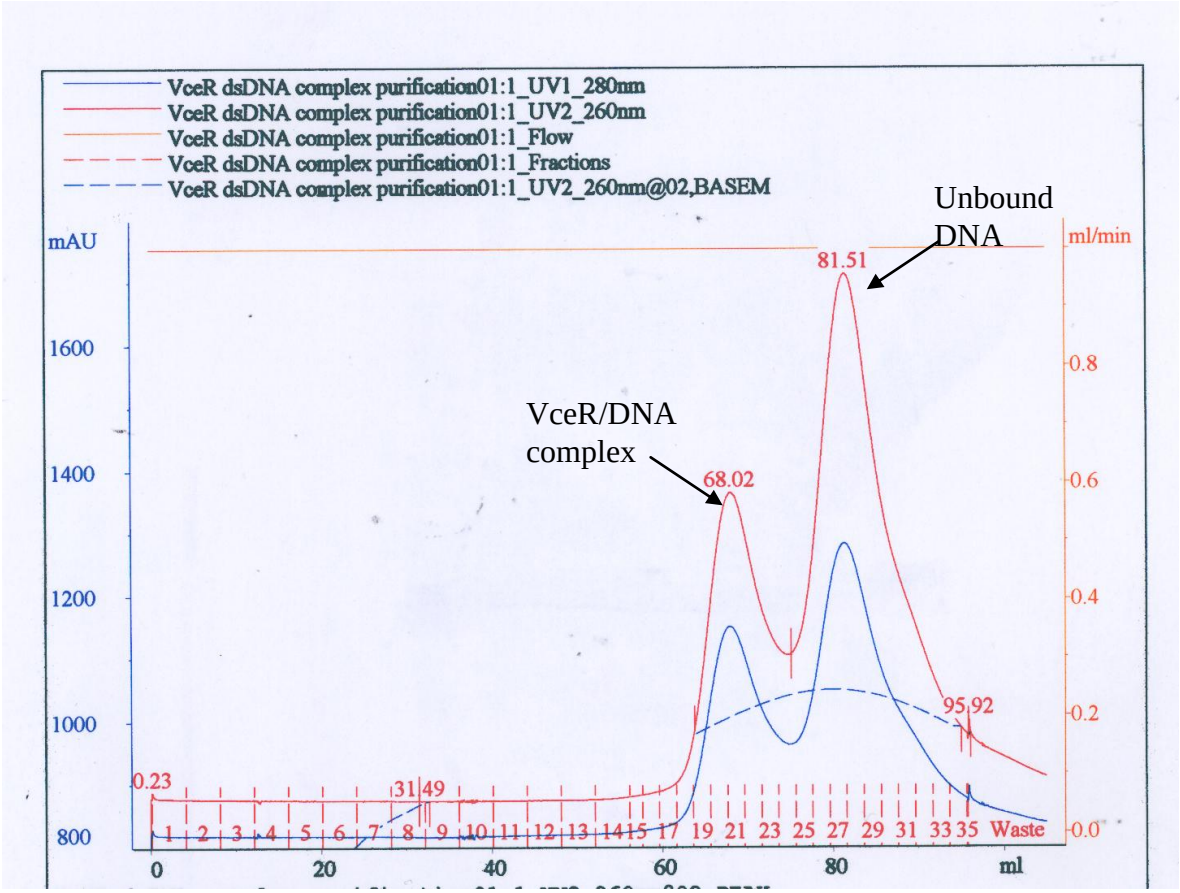

Figure 5.9 The elution chromatography of VceR-CCCH/DNA complex from a Hi-load 16/60 Superdex 200 prep grad column. The curve of UV 260 nm is shown in red and UV 280 nm in blue.

5.7.2 Crystallization of purified VceR-CCCH/DNA complex

As described in Section 2.14, the crystallization screening of purified VceR-CCCH/DNA complex was performed. After 3 week incubation at 20^{o}C, crystals of purified VceR-CCCH/P56 (30 bp oligos) were obtained in the following conditions:

(1) A8 (0.1 M sodium acetate, pH 5.5, 1.8 M lithium sulphate) of the Clear strategy screen from Molecular Dimensions
(2) B1 (0.1 M sodium citrate, pH 4.0, 0.8 M ammonium sulphate) of the JCSG-plus from Molecular Dimensions (Page *et al*., 2003).

Crystals of purified VceR-CCCH/P56-1 (28 bp oligos) were obtained in the following conditions:

(1) C11 (0.1 M sodium acetate pH 4.6, 2 M ammonium sulphate) of JCSG-plus from Molecular Dimensions
(2) B1 (0.1 M sodium citrate, pH 4.0, 0.8 M ammonium sulphate) of JCSG-plus from Molecular Dimensions

The optimization was based on these crystallization conditions. A gradient of pH and concentration of precipitant was set up as shown in Table 5.4, 5.5 and 5.6. The crystals from these conditions are shown in Figure 5.10. Different DNA pairs (Table 2.5) in complex with VceR-CCCH were purified by gel filtration and used in the crystallization conditions in Tables 5.4, 5.5 and 5.6. The VceR-CCCH/P56-24 and VceR-CCCH/P56-26 complexes were not stable. The crystals were frozen in liquid nitrogen and taken to the SLS for diffraction analysis. Crystals could be formed from VceR-CCCH/P56-3, VceR-CCCH/P56-5, VceR-CCCH/P56- 6, VceR-CCCH/P56-27 and VceR-CCCH/P56-28, but the diffraction from them did not exceed 3.2 Å. The best diffraction was 3.15 Å from the VceR-CCCH/P56-1 crystal in 0.1 M Na citrate pH 4.0, 0.85 M ammonium sulphate) with 30% glycerol as cryo-solution. Table 5.7 shows data collection statistics of a VceR-CCCH/P56-1 crystal.

pH 5.2 → pH 5.7

1.6 M lithium sulphate ↓ 1.9 M lithium sulphate

A1	A2	A3	A4	A5	A6
B1	B2	B3	B4	B5	B6
C1	C2	C3	C4	C5	C6
D1	D2	D3	D4	D5	D6

Table 5.4 Lithium sulphate and pH gradient screen

pH 3.8 → pH 4.3

0.75 M ammonium sulphate ↓ 0.9 M ammonium sulphate

A1	A2	A3	A4	A5	A6
B1	B2	B3	B4	B5	B6
C1	C2	C3	C4	C5	C6
D1	D2	D3	D4	D5	D6

Table 5.5 Ammonium sulphate and pH gradient screen I

1.8 M ammonium sulphate

pH 4.4 → pH 4.9

2.1 M ammonium sulphate

A1	A2	A3	A4	A5	A6
B1	B2	B3	B4	B5	B6
C1	C2	C3	C4	C5	C6
D1	D2	D3	D4	D5	D6

Table 5.6 Ammonium sulphate and pH gradient screen II

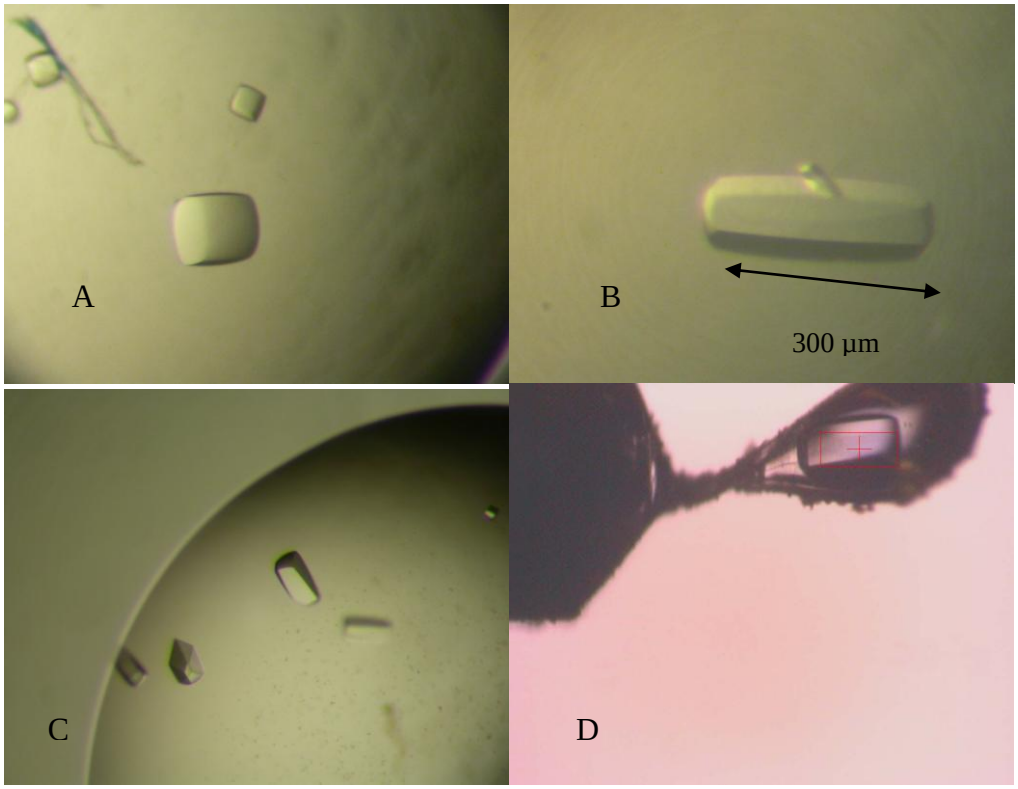

Figure 5.10 Crystals formed from the purified protein/DNA complex.
(A) VceR-CCCH/dsDNA (P56) crystals formed in the crystallization buffer (0.1 M Na acetate, pH 4.8, 1.6 M lithium sulphate) at 20^{o}C. (B) VceR-CCCH/dsDNA (P56-1) crystals formed in the crystallization buffer (0.1 M Na citrate, pH 4.0, 0.85 M ammonium sulphate) at 20^{o}C. (C) VceR-CCCH/dsDNA (P56-1) crystals formed in the crystallization buffer (0.1M Na acetate pH 5.4, 1.8 M ammonium sulphate) at 20^{o}C (D) VceR-CCCH/dsDNA (P56-1) crystals in cryo-solution under the flow of cold nitrogen (ice formed around the loop)

	Native
Beamline	SLS X06DA
Wavelength (Å)	1.000
Resolution (Å)	43.17-3.15
(last shell)	3.25-3.15
R_{merge} [a b]	0.086(0.665)
Total/Unique reflections	72717/10918
Completeness	97.8(96.3)
Multiplicity	4.2
I/σ*(I)*	19.3(1.8)
Cell dimensions	a= b=90.2 Å, c=298.0 Å, α=β=γ=90°
Space group	I $4_{1/3}22$

Table 5.7 Data collection statistics of a VceR-CCCH/P56-1 crystal.

[a] The values in parentheses of R_{merge}, completeness, and I/σ*(I)* correspond to the outermost resolution shell.
[b] R_{merge} = ΣhΣj |I(h;*j*)- <I(h)>| /ΣhΣjI(h), where I(h;*j*) is the *j*th measurement of the intensity of the unique reflection h, and <I(h)> is the mean overall symmetry-related measurements.

5.8 Br-labelled crystals

To provide phasing information, the QacR/DNA model was used in molecular replacement. However, the low identity (17.7%) between QacR and VceR hampered successful structure solution. Thus, brominated DNA oligonucleotides were designed and crystallized in complex with VceR.

Brominated DNA P5-1-BrP6-1 (Table 5.8), in which thymines were substituted with 5-Br-uracil, was synthesized from Operon, and co-crystallized with VceR-CCCH. Three wavelength MAD data sets were collected from a crystal of VceR-CCCH/P5-1-BrP6-1 at the DLS. A typical diffraction pattern for a VceR-CCCH/P5-1-Br crystal at the DLS is shown in Figure 5.11. Table 5.9 shows data collection statistics of a VceR-CCCH/P5-1-BrP6-1 crystal.

P5-1-BrP6-1: 5'-TATAAC**T**AAACGGTACGG**T**TTAG**TT**ATA-3' 3'-ATATTGATTTGCCATGCCAAATCAATAT-5'
Duplex-PLS1 (DPLS1) : 5'-TATAAC**T**AAACGGTACGG**TT**TAGTTATA-3' 3'-ATATTGAT**TT**GCCATGCCAAA**T**CAATAT-5'
Duplex-PLS2 (DPLS2) : 5'-TA**T**AAC**T**AAACGGTACGGT**TT**AGTTATA-3' 3'-ATATTGA**TT**TGCCATGCCAAA**T**CAA**T**AT-5'

Table 5.8 Brominated DNA duplexes for phasing calculation. Bold thymines were substituted with 5-Br-uracil.

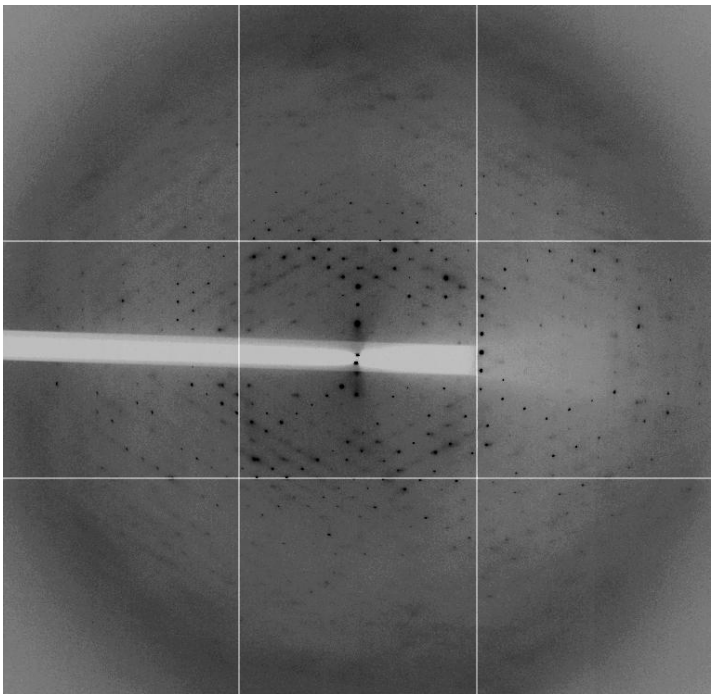

Figure 5.12 A diffraction pattern for a VceR-CCCH/ P5-1-BrP6-1 crystal recorded at the Diamond Light Source.

Palindromic sequences labelled with Br (DPLS1 and DPLS2, Table 5.8) were designed (explanation in Section 5.9). Purification of VceR-CCCH in complex with DPLS1 and DPLS2 were performed as for the VceR-CCCH/P56-1 complex and similar crystallization conditions were used. Crystals of VceR-CCCH/DPLS2 were obtained and a three wavelength MAD data set was collected. Table 5.10 shows data collection statistics of a VceR-CCCH /DPLS2 crystal.

	Br (nonpalindromic)		
	Peak	Inflection point	Remote
Beamline	DLS I04	DLS I04	DLS I04
Wavelength (Å)	0.9200	0.9202	0.9132
Resolution (Å)	48.83-3.25	48.91-3.48	48.86-3.48
(last shell)	3.35-3.25	3.58-3.48	3.58-3.48
R_{merge} [a] [b]	0.096(0.623)	0.084(0.484)	0.087(0.516)
Total/Unique reflections	220277/9903	187621/7980	180026/7831
Completeness	94.7(74.8)	92.6 (60.7)	91.3 (60.4)
I/σ*(I)*	18.6(1.6)	19.1(4.5)	21.9(4.5)
Cell dimensions	a=b=91.0, c= 299.9 Å, α=β=γ=90°	a=b=91.0, c= 299.9 Å, α=β=γ=90°	a=b=91.0,c= 299.9 Å, α= β= γ=90°
Space group	I $4_{1/3}22$	I $4_{1/3}22$	I $4_{1/3}22$

Table 5.9 Data collection statistics of a VceR-CCCH/P5-1-BrP6-1 crystal.

[a] The values in parentheses of R_{merge}, completeness, and I/σ*(I)* correspond to the outermost resolution shell.
[b] R_{merge} = ΣhΣj |I(h;*j*)- <I(h)>| /ΣhΣjI(h), where I(h;*j*) is the *j*th measurement of the intensity of the unique reflection h, and <I(h)> is the mean overall symmetry-related measurements.

	Br (palindromic)		
	Peak	Inflection	Remote
Beamline	DLS I04	DLS I04	DLS I04
Wavelength (Å)	0.9198*	0.9204*	0.9050*
Resolution (Å)	49.96-3.6	49.96-3.5	48.67-3.71
(last shell)	3.69-3.6	3.6-3.5	3.80-3.71
R_{merge} [a b]	0.103(0.586)	0.087(0.647)	0.121(0.645)
Total/Unique reflections	80590/7584	40124/8325	52413 /6986
Completeness	98.6 (89.0)	93.0 (66.2)	98.9 (93.3)
I/σ*(I)*	12.31(4.0)	10.81(2.6)	9.07(2.9)
Cell dimensions	a=b=90.6, c= 299.4 Å, α=β=γ=90°	a=b=90. 6, c=299.4 Å, α= β=γ=90°	a=b=90. 6, c= 299.4 Å, α= β= γ=90°
Space group	I $4_{1/3}22$	I $4_{1/3}22$	I $4_{1/3}22$

Table 5.10 Data collection statistics of a VceR-CCCH /DPLS2 crystal

[a] The values in parentheses of R_{merge}, completeness, and I/σ*(I)* correspond to the outermost resolution shell.

[b] R_{merge} = ΣhΣj |I(h;*j*)- <I(h)>| /ΣhΣjI(h), where I(h;*j*) is the *j*th measurement of the intensity of the unique reflection h, and <I(h)> is the mean overall symmetry-related measurements.

* These values are estimated of true energy only because no fluorescence emission scanning device is available.

5.9 Substructure solution of Br

As described in 2.14.4, Xprep (Bruker AXS, Madison, USA) was used to produce input files for running on ShelxD (Schneider and Sheldrick, 2002; Sheldrick, 2008) in order to determine the Br positions. The anomalous signals of Br from a VceR-CCCH/P5-1-BrP6-1 crystal are shown in Table 5.11. Even though the anomalous signal from Br scatterers is not poor, the correct position of Br could not be located. The possible explanation is that the pseudo-symmetry of the Br sites breaks the crystal symmetry (only half of 28 bp duplex in the asymmetric unit). Two pairs of brominated DNA duplex with palindromic Br sites were thus designed and tried (DPLS1 and DPLS2 in Table 5.8). However, the device for fluorescence emission scanning was not available at DLS when we tested these crystals. Consequently, the theoretical values were used. Thus, the anomalous signal of Br from these crystals (VceR-CCCH/DPLS2) is weak (Table 5.12) and the CC between the 3 wavelength data sets is low (Table 5.13). The correct positions of Br sites cannot be determined for phasing.

Resolution (Å)	8.0	6.0	5.0	4.8	4.6	4.4	4.2	4.0	3.8	3.6	3.4
Anomalous signal/noise ratios (peak)	1.89	1.50	1.31	1.27	**1.18**	1.1	1.19	1.12	1.06	1.06	0.99

Table 5.11 Anomalous signal/noise ratios of VceR-CCCH/P5-1-BrP6-1 data set. The values are based on variances of F^+ and F^-, calculated by Xprep. The cutoff of significant anomalous signals is shown in bold.

Resolution (Å)	8	6	5.4	5.2	5.0	4.8	4.6	4.4	4.2	4.0	3.8
Anomalous signal/noise ratios (Peak)	1.34	1.30	1.24	**1.20**	1.15	1.14	0.95	1.07	1.15	1.03	0.92
Anomalous signal/noise ratios (Inflection)	1.07	1.18	1.2	1.05	1.17	1.16	1.07	1.17	1.12	1.00	1.01
Anomalous signal/noise ratios(Remote)	1.25	1.04	1.13	1.29	1.38	1.26	**1.31**	1.17	1.17	1.09	1.01

Table 5.12 Anomalous signal/noise ratios of VceR-CCCH/DPAL2 data set. The values are based on variances of F^+ and F^-, calculated by Xprep. The cutoff of significant anomalous signals of each data set is shown in bold.

Resolution (Å)	8	6	5.4	5.2	5.0	4.8	4.6	4.4	4.2	4.0	3.8
Peak Against Remote (%)	7.6	39.1	28.7	18.1	10.9	6.8	6.6	-8	2	10.6	4
Inflection Against Remote (%)	8.5	28.8	20.2	8.7	-15.9	-7.4	-4.0	2.4	1.7	-1.9	0.6
Inflection Against Peak (%)	20.3	30.4	23.5	1.7	3.9	4.5	14.3	-4.5	1.3	9.3	5.3

Table 5.13 Low anomalous correlation coefficients (%) between peak, remote and inflection of VceR-CCCH/DPAL2 data set, calculated by Xprep.

5.10 Preparation of selenomethionine-containing proteins

As described in Section 2.14.2, selenomethionine substituted VceR-CCCH was prepared and purified. The crystallization of the Se-VceR-CCCH/DNA was performed as for VceR-CCCH/DNA (Section 5.7.1 and 5.7.2).

5.11 Data collection and processing

Scanning the fluorescence emission spectrum of crystals of the Se-VceR/DNA at the SLS clearly showed the presence of Se in the crystals and was used in selecting the wavelengths for MAD. The data collection statistics of a Se peak data set is summarized in Table 5.14 and those of two Se-MAD data sets are summarized in Table 5.15 and 5.16.

	Se peak
Beamline	SLS X06SA
Wavelength (Å)	0.9793
Resolution (Å)	49.95-3.50
(last shell)	3.60 - 3.50
R_{merge} [a b]	18.3(76.4)
Total/unique reflections	84400/8350
Completeness	99.6(97.0)
I/σ*(I)*	8.5(3.0)
Cell dimensions	a= b=90.8, c=299.0 Å, α=β=γ=90°
Space group	I $4_{1/3}22$

Table 5.14 Data collection statistics of a Se-VceR-CCCH/P56-1 crystal (Se data set I).

[a] The values in parentheses of R_{merge}, completeness, and I/σ*(I)* correspond to the outermost resolution shell.
[b] R_{merge} = ΣhΣj |I(h;*j*)- <I(h)>| /ΣhΣjI(h), where I(h;*j*) is the *j*th measurement of the intensity of the unique reflection h, and <I(h)> is the mean overall symmetry-related measurements.

	Se		
	Peak	Inflection	Remote
Beamline	SLS X06SA	SLS X06SA	SLS X06SA
Wavelength (Å)	0.9795	0.9797	0.9686
Resolution (Å)	48.86-3.75	50.05-3.76	48.86-3.71
(last shell)	3.85-3.75	3.86-3.76	3.81-3.71
R_{merge} [a b]	11.4(49.1)	12.4(51.4)	11.4(55.7)
Total/Unique reflections	47061/6788	59929/6743	65011/6979
Completeness	98.1 (91.2)	98.1 (89.9)	97.8(86.2)
I/σ*(I)*	10.1(3.2)	10.6(4.3)	12.2(4.4)
Cell dimensions	a=b=91.2, c=299.3 Å, α=β=γ=90°	a=b=91.0, c=299.0 Å, α=β=γ=90°	a=b=91.2, c=299.3 Å, α=β=γ=90°
Space group	I $4_{1/3}22$	I $4_{1/3}22$	I $4_{1/3}22$

Table 5.15 Data collection statistics of a Se-VceR-CCCH/P56-1 crystal (Se data set II)

[a] The values in parentheses of R_{merge}, completeness, and I/σ*(I)* correspond to the outermost resolution shell.

[b] R_{merge} = ΣhΣj |I(h;*j*)- <I(h)>| /ΣhΣjI(h), where I(h;*j*) is the *j*th measurement of the intensity of the unique reflection h, and <I(h)> is the mean overall symmetry-related measurements.

	Se		
	Peak	Inflection point	Remote
Beamline	SLS X06SA	SLS X06SA	SLS X06SA
Wavelength (Å)	0.9795	0.9797	0.9686
Resolution (Å)	49.88-3.6	49.77-3.78	49.77-3.75
(last shell)	3.70-3.60	3.87-3.78	3.85-3.75
R_{merge} (%)[a b]	14.1(63.5)	17.5(48.4)	14.4(51.4)
Total/unique reflections	53691/7653	58934/6555	53756/6755
Completeness	99.4(96.3)	98.3(84.7)	98.9(92.4)
I/σ*(I)*	7.14 (2.2)	5.35(2.5)	7.16(3.3)
Cell dimensions	a=b=90.6, c= 298.4 Å, α=β=γ=90°	a=b=90.6, c=298.4 Å, α= β=γ=90°	a=b= 90.6, c= 298.4 Å, α= β=γ=90°
Space group	I $4_{1/3}22$	I $4_{1/3}22$	I $4_{1/3}22$

Table 5.16 Data collection statistics of a Se-VceR-CCCH/P56-1 crystal (Se data set III)

[a] The values in parentheses of R_{merge}, completeness, and I/σ*(I)* correspond to the outermost resolution shell.

[b] R_{merge} = ΣhΣj |I(h;*j*)- <I(h)>| /ΣhΣjI(h), where I(h;*j*) is the *j*th measurement of the intensity of the unique reflection h, and <I(h)> is the mean overall symmetry-related measurements.

5.12 Substructure solution of Se

For Se substructure determination, the *f'* and *f''* values for Se at peak, inflection point and high energy remote were obtained from http://skuld.bmsc.washington.edu/scatter/AS_form.html. Xprep (Bruker AXS, Madison, USA) was used to produce input files for running on ShelxD (Schneider and Sheldrick, 2002; Sheldrick, 2008) in order to determine the Se positions. However, the correct Se positions could not be determined from the Se data sets I, II or III (Table 5.14, 5.15 and 5.16) singly. Finally, two data sets (Se data set II and III) of three wavelengths (Table 5.15 and 5.16) and one peak data (Se data set I) (Table 5.14) were scaled and merged together with Xprep (Bruker AXS, Madison, USA). Table 5.17 shows the anomalous signal/noise ratios of the merged Se-MAD data set and Table 5.18 shows the anomalous correlation coefficient between peak, inflection and high energy remote data of the merged Se-MAD data set. Using this merged data set, the 12 selenium positions in the asymmetric unit were located from a three-wavelength anomalous dispersion experiment with ShelxD (Schneider and Sheldrick, 2002; Sheldrick, 2008). Figure 5.12 shows the clear cutoff of occupancy between the 12th and 13th sites and the statistics for CC (correlation coefficient between observed and calculated *E* values) and CC (weak) are consistent with the correct positions of the 12 Se.

Resolution (Å)	8	6	5.3	5.1	4.9	4.7	4.5	4.3	4.1	3.9	3.7
Anomalous signal/noise ratios (Peak)	3.33	2.58	2.04	1.61	1.52	1.46	1.42	1.22	1.21	**1.14**	1.02
Anomalous signal/noise ratios (Inflection)	4.4	2.33	1.84	1.48	1.51	1.35	1.32	1.3	**1.2**	1.07	1.01
Anomalous signal/noise ratios (Remote)	3.31	1.81	1.39	1.29	1.38	1.26	1.31	1.17	**1.17**	1.09	1.01

Table 5.17 Anomalous signal/noise ratios of merged Se data sets. The values are based on variances of F^+ and F^-, calculated by Xprep. The cutoff of significant anomalous signals of each data set is shown in bold.

Resolution (Å)	8	6	5.3	5.1	4.9	4.7	4.5	4.3	4.1	3.9	3.7
Peak against remote (%)	68	80.0	68.5	49.9	48.7	40.5	**30.9**	26.7	25.1	15	9.1
Inflection against remote (%)	72.8	76.9	52.4	48.6	38.3	**41.0**	24.7	27.2	20.8	13.4	27.5
Inflection against peak (%)	57.7	85.8	63.2	56.0	56.4	43.4	**37.9**	29.0	22.8	16.7	25.4

Table 5.18 Anomalous correlation coefficients (%) betweens peak, remote and inflection of Se merged data sets, calculated by Xprep. The cutoff of significant anomalous correlation coefficients between each data set is shown in bold.

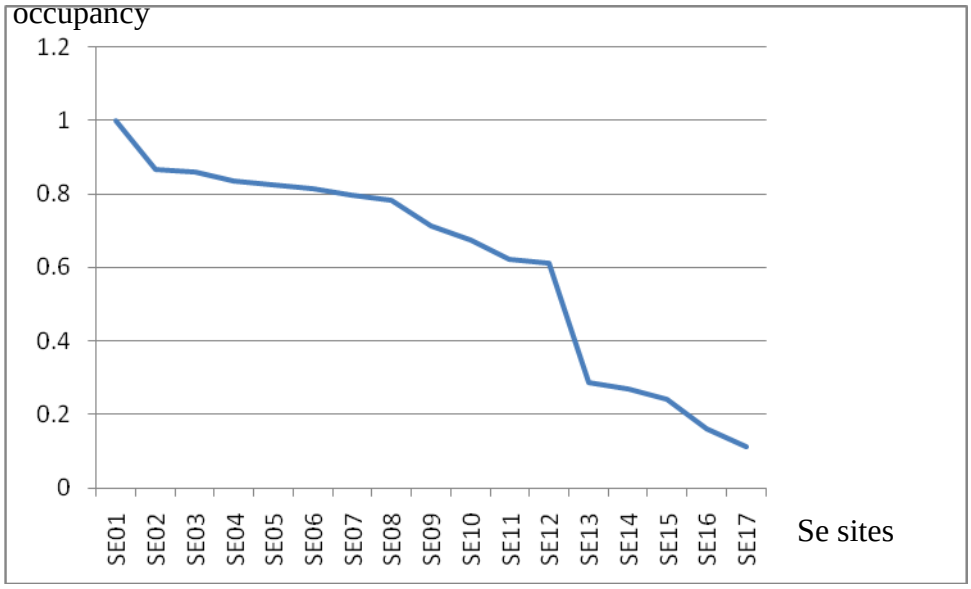

Figure 5.12 The occupancies for selenium positions with CC 63.84% and CC(weak) 51.36%. There is the clear cutoff of occupancy between the 12th and 13th sites.

5.13 Phasing and model building

As described in Section 2.14.5, mtz files were produced for Sharp (Bricogne *et al*., 2003) with columns containing native and three wavelength data sets. The high energy remote data set was used as the reference for scaling, and the default setting of Sharp was used. The 12 Se atom sites from ShelxD and their inversed sites were used as the input site in Sharp. In addition, the space group $I4_122$ and $I4_322$ were tested in Sharp. After the solvent flattening (54%) by DM, the map with space group $I4_122$ was interpretable. Figure 5.14 shows the electron density map after solvent flattening in Sharp, which clearly reveals helical features.

To build a polyalanine model, the connected helix 5 and helix 6 of the QacR monomer from the QacR model (PDB code 1JT0) was superimposed on the electron density map manually in Coot. More helices were superimposed on the electron density map and the model was extended to the whole dimer manually (Figure 5.13 and 5.14). The electron density for the last 3 bp at the end of duplex is missed in the map after solvent flattening. For the DNA model, 11 bp duplex of B-DNA from Coot were manually superimposed on the electron density map. The crystallographic

symmetry operation of space group I 4_122 was used to produce the preliminary model for two VceR dimers bound to a 22 bp duplex, which is shown in Figure 5.13.

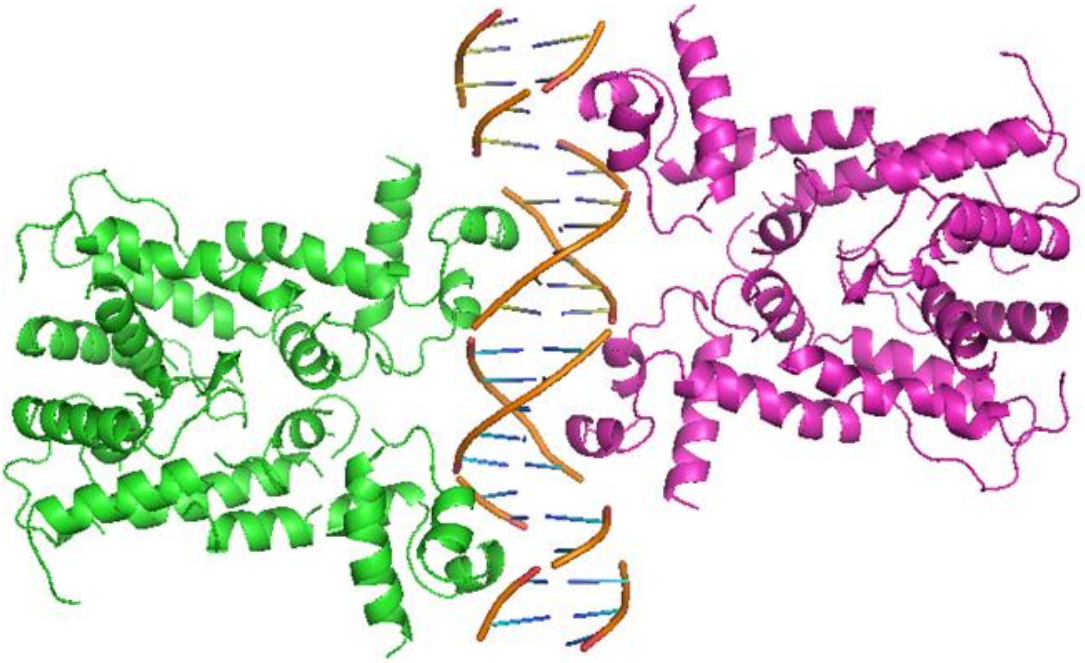

Figure 5.13 The ribbon representation of two VceR dimers bound to a 22 bp duplex.

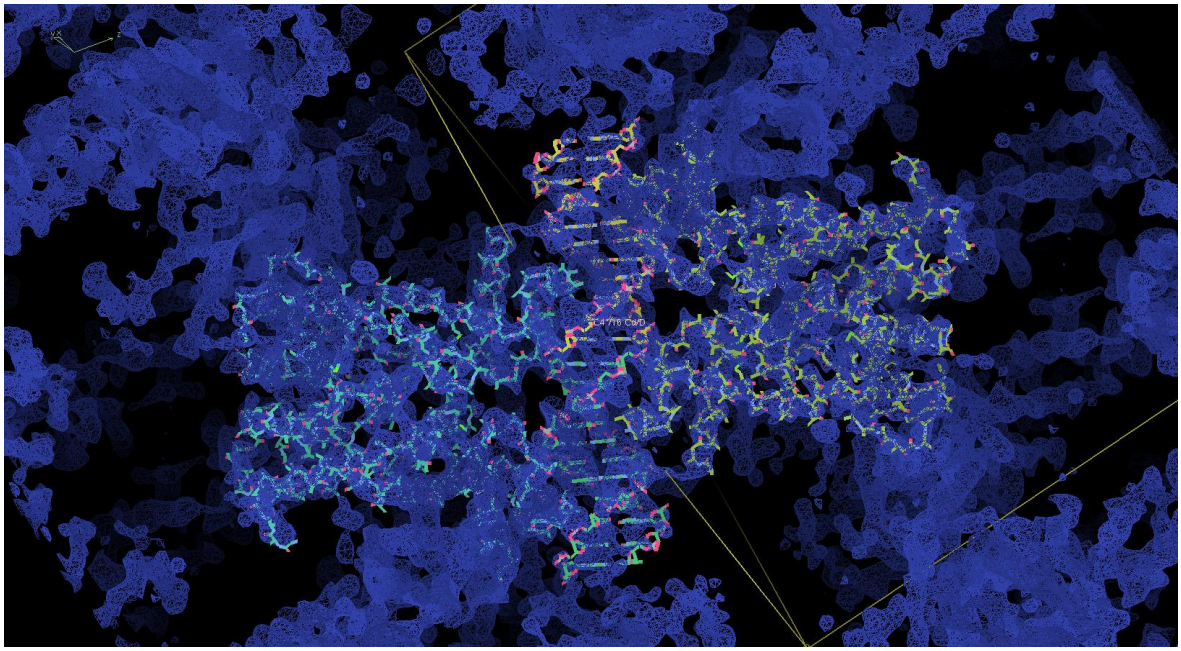

Figure 5.14 A 3.2 Å Se-MAD electron-density map at 1.0 σ superimposed with two VceR dimers bound to a 22 bp duplex.

5.14 Discussion

5.14.1 Oligo design for protein/DNA co-crystallization

The interactions between DNA molecules often generate crystal packing contacts, which make the choice of DNA fragments critical for the formation of X-ray quality protein/DNA co-crystals (Tan *et al.*, 2000). However, there is no method to predict the correct DNA fragment to obtain X-ray quality complex crystals. The empirical search for fragments of different lengths and ends is the main strategy for selecting DNA fragments in protein/DNA co-crystallization.

The 30 bp P56 DNA duplex (Figure 5.2), bound with VceR, was chosen as the starting point to generate the crystals of the VceR/dsDNA complex. However, the diffraction power of the crystals formed by VceR/P56 could not be improved (Section 5.4 and 5.5, and Table 5.3). Different pairs of oligodeoxynucleotides (Table 2.5) were designed and used into co-crystallization trials. The complex crystals formed from 28 bp P56-1 gave the best diffraction. These results suggest that there was no better method to determine the length and the end of the DNA for protein/DNA co-crystallization, and that all possibilities for the DNA design to improve diffraction resolution should be put into trials.

Although there is no method to predict the best DNA fragment for protein/DNA co-crystallization, DNase I footprinting assays are important for defining the starting DNA sequence for protein/DNA co-crystallization. Any base bound to protein could be protected from the digestion by DNase I, which produces the DNA sequence for co-crystallization. This method has been widely used in protein/DNA co-crystallization successfully, e.g. DtxR bound with the *tox* operator (White *et al.*, 1998). Interestingly, in the DtxR example, three structures of the DtxR/DNA complex were solved from three pairs of duplex DNA of 43 bp, 33 bp and 21 bp (Chen *et al.*, 2000; White *et al.*, 1998; Pohl *et al.*, 1999), which indicates that different designs of the oligonucleotide can produce X-ray quality crystals.

5.14.2 Simple mixture or purification of protein/DNA complex for co-crystallization

The stoichiometry of the components of the protein/DNA complex should be considered in preparing the complex for co-crystallization. One method is the examination of the complex over a series of protein:DNA ratios using EMSA to determine the ratio for maximal complex formation. Alternatively, analytical gel filtration or dynamic light-scattering could be used to calculate the molecular weight of the protein/DNA complex, from which the ratio of protein to DNA in the complex can be known. The ratio of VceR monomer to DNA in the VceR/DNA complex is 4:1, two dimers of VceR bound to DNA, indicated from analytical gel filtration and dynamic light-scattering.

Usually, in the preparation of the protein DNA complex, an excess of DNA is used, because the efficiency of DNA annealing is less than 100%. In this study, the ratio of VceR to DNA was increased to 2:1 for co-crystallization, rather than 4:1 for complex formation. In addition, the purification of the protein/DNA complex for co-crystallization was also tried. The advantage of this method is the high purity of the complex and the elimination of any unbound protein or DNA. However, before purifying the protein/DNA complex its stability should be considered, as the presence of an excess amount of unbound DNA could force the equilibrium (the equilibrium between free protein and DNA and the protein/DNA complex) to the protein/DNA complex forming and stabilize the protein/DNA complex, when there is a low protein-DNA binding affinity.

5.14.3 Palindromic or nonpalindromic sequence in protein /DNA co-crystallization

A palindromic sequence has an identical sequence with its complementary sequence. The recognition sites of many restriction enzymes are palindromic. In TetR, the DNA sequence used in TetR/DNA complex crystallization was derived from the natural promoter with a perfect palindrome (Orth *et al.*, 2000) In QacR/DNA complex crystals, the DNA used was mutated to form the complete inverted repeat (Schumacher *et al*., 2002). In this study, both palindromic and non-palindromic

sequences (Table 2.5) formed crystals with VceR. However, DNA with high palindromic order formed complex crystals more easily than the natural one with an imperfect palindrome (data not shown). This phenomenon could be explained by the fact that the optimization of the palindrome in the operator sequence increases the binding of the second dimer to the operator. This behaviour was found for TtgR, a TetR family repressor (Krell *et al*., 2007). Further studies will be needed to determine the effect of the palindromic sequence in the binding of VceR to the operator sequence.

5.14.4 Substructure and phasing

The phase problem is an inevitable challenge in protein crystallography (Taylor, 2003). Because of the presence of homology models and the availability of synchrotron beamlines, several methods, including MR (Molecular Replacement), SIR (Single isomorphous replacement), SIRAS (single isomorphous replacement with anomalous scattering), MIR (multiple isomorphous replacement), MIRAS (multiple isomorphous replacement with anomalous scattering), MAD (Multiple-wavelength anomalous dispersion) and SAD (single-wavelength anomalous dispersion) are widely used to solve the phase problem (Taylor, 2003). For solving the phase problem for protein/DNA complexes, the incorporation of selenomethionine into the protein, the labelling of DNA and the soaking of heavy atoms into crystals have been utilized to obtain phasing, if there is no homology model available (Konig *et al*., 2009; Schumacher *et al*., 2002).

In this study, because of the low sequence identity of VceR in comparison to QacR 17.7% (generally, 25% or higher sequence identity is required for successful molecular replacement, Taylor, 2003), the use of the QacR/DNA model to solve the VceR/DNA structure was unsuccessful. Instead, bromines incorporated into the DNA and later selenomethionine in the protein were taken as anomalous scatterers to perform MAD or SAD experiments. Initially, the phasing experiments started with the brominated DNA pair P5-1-BrP6-1(Table 5.8). However, the location of the Br in this DNA duplex could not be determined, possibly due to the pseudo-symmetry of the Br sites, which breaks the crystal symmetry.

Further efforts were carried out using both symmetric brominated DNA (Table 5.8) and selenomethionine substituted VceR. However, the VceR-CCCH/DPAL2 crystals had a very weak anomalous signal (Table 5.12and 5.13), because of the incorrect wavelengths used in peak, inflection and remote data collection.

Interestingly, merging of two three-wavelength Se data sets and one peak Se data set produced the correct substructure, as indicated by CC/low CC in ShelxD (Table 5.18) and following refinement of the Se positions in Sharp. This merging of several data sets could increase the anomalous signals for Se substructure calculation (Table 5.17), and will be a good method in solving the substructure of low resolution data sets.

Chapter 6 Final discussion and future work

6.1 Hpa1

6.1.1 Fibril formation mechanism of Hpa1

We found that full length Hpa1 was able to assemble into fibrils at acidic pH (Figure 3.8) Similar pH-dependent fibril assembly has been widely reported (Cruz *et al.*, 2005; Lai *et al.*, 1996; Morozova-Roche *et al.*, 2000; Smith *et al.*, 2003; Uversky and Fink, 2004). One explanation of this phenomenon is that the fibril forming precursors have low net charge or even zero at acidic pH, which accelerates fibril assembly (Chiti *et al.*, 2002; Schmittschmitt and Scholtz, 2003). However, pHs around the pI of Hpa1 only induce precipitation of Hpa1 in this study (data not shown). The fact that the C-terminal α helical domain is the fibril forming domain of Hpa1, but cannot assemble into fibrils in the presence of the N-terminal α helical domain suggests that the assembly of fibrils by Hpa1 requires separation of the C-terminal α helical domain from the N-terminal α helical domain. Similar domains acting to prevent fibril formation were reported for lysozyme (Mishima *et al.*, 2007). A mechanism for fibril assembly was proposed that the fibril formed by full length Sup35 involves the intermolecular interaction of one region of Sup35 (Krishnan and Lindquist, 2005). Acidification of the pH might change the conformation of Hpa1 and promote the association of the C-terminal α helical domain with itself for fibril assembly.

In addition, the fibril assembly of the C-terminal α helical domain of Hpa1 seems to be an inherent characteristic of the sequence component, which is independent of pH (Figure 4.5). Several characteristics of the amino acid sequence have been thought to facilitate fibril assembly. For example, aromatic moieties could be recognition interfaces, which mediate the early stage of amyloid formation, and the stacking interactions of these aromatic moieties provides an energetic contribution in the self-assembly of amyloid structure (Azriel and Gazit, 2001; Gazit, 2002; Gazit, 2005; Gazit, 2007). However, there is no aromatic moiety in peptide 2 (ASPLTQMLMNIVGEILQAQ) of Hpa1, which could facilitate the assembly into fibrils.

The other characteristic of the amino acid sequence required for fibrillogenesis is attractive electrostatic interactions. For example, K-E interactions seem to be essential for the fibril assembly, since the peptides KFFK or EFFE did not form fibrils when incubated alone, but did so when co-incubated (Tjernberg *et al*., 2002). The sequence of peptide 2 (ASPLTQMLMNIVGEILQAQ) has one negatively charged E, but no positively charged residues (K or R).

On the other hand, the inherent aggregation propensity, which is dependent on the intrinsic physiochemical properties of the amino acids in the sequence, is thought to be one reason for fibril assembly (Chiti and Dobson, 2006; Routledge *et al*., 2009). Predictions of the aggregation-prone regions of whole length Hpa1 identified residues (Hpa1 90-101, LTQMLMNIVGEI) as the most aggregation-prone region (Conchillo-Sole *et al*., 2007) is in agreement with the experimental data that peptide 2 is the segment of Hpa1 for fibril assembly. This result suggests the inherent aggregation propensity of peptide2 in this study is important for its fibril assembly.

The determinants for fibril formation are not fully understood and there is no common motif among fibril forming proteins. The inherent aggregation propensity might be important for fibril assembly and more cases are needed to demonstrate this hypothesis in the future.

6.1.2 Secretion of Hpa1 through TTSS and its function in *Xanthomonas*

Hpa1, the harpin of *Xanthomonas*, is secreted via TTSS (Zou *et al*., 2006). However, the *in vivo* state of Hpa1 and how Hpa1 is secreted through the narrow Hrp pilus of TTSS remain unknown. One possible explanation is that most effectors would be translocated or secreted in an unfolded state and TTSS chaperones maintain effectors in this state (Alfano and Collmer, 2004). However, such chaperones of the TTSS in *Xanthomonas* have not been reported. Further work could be performed using Hpa1 as the bait in two hybrid screens with a library of *Xanthomonas* proteins to find this kind of chaperone. In addition, heat shock proteins (HSP) stabilize partially unfolded proteins, help in protein folding and prevent the unwanted protein aggregation (Ohtsuka and Hata, 2000). HSP was also found to disassemble the fibrils (Shorter and Lindquist, 2008; Shorter, 2008). The possible interaction between Hpa1 and HSP, and stabilization of Hpa1 by HSP, could be studied in future work.

The data presented here have expanded the view for the function of harpins. Our finding of direct membrane damaging by fibrils of Hpa1 and its derivatives indicates their possible toxicity to the biological membrane, which has never been reported. However, the *in vivo* data are required to show this toxicity in its host plant rice and the biological function of fibril assembly of Hpa1 in the pathogenicity of *Xanthomonas orzyae* pv. oryzicola.

6.2 Crystallization of VceR in complex with its cognate DNA

6.2.1 DNA binding domain of VceR

Three protein/DNA structures from the TetR family have been determined: one dimer of TetR bound to a 15 bp operator DNA (Orth *et al*., 2000), two dimers of QacR bound to a 28 bp operator DNA (Schumacher *et al*., 2002) and two dimers of CgmR bound to a 28 bp operator DNA (unpublished, PDB code 2yvh). As a conserved signature of the TetR family, TetR repressors use a helix-turn-helix (HTH) motif to bind the operator DNA (Ramos *et al*., 2005). VceR share 29.8% sequence identity with QacR in the DNA binding domain (Figure 5.1) and binds the 28 bp promoter DNA as a pair of dimers, as determined by SEC and dynamic light scanning (Borges-Walmsley *et al*., 2005). The model of VceR/DNA complex in this study shows VceR uses the same DNA binding style with QacR, two dimers bound with an operator DNA. Future work has to refine model and improve phasing to show the interaction between VceR and DNA.

6.2.2 Drug binding domain of VceR

VceR, a TetR repressor, binds to a 28 bp sequence within the *vceR-vceCAB* intergenic region and thus repress the expression of the VceCAB drug efflux pump through steric hindrance of RNA polymerase binding to the operator (Borges-Walmsley *et al*., 2005). A pump substrate, CCCP (carbonyl cyanide m-chlorophenyl-hydrazone) binds to VceR and dissociates it from the binding site (Borges-Walmsley *et al*., 2005). As determined by stopped-flow fluorescence spectroscopy, the VceR monomer possesses two binding-sites that can be occupied by CCCP simultaneously (Borges-Walmsley *et al*., 2005). However, the drug binding pocket of VceR could not be located in this study. The determination of the VceR/DNA complex structure could provide clues about the drug binding pocket of VceR.

In the QacR drug binding pocket, Glu is widely used in the neutralization of the positively charged drug. Interestingly, Glu120 in the QacR-Et complex, Glu58 in QacR-Dq and QacR-Be complex have their counterparts in VceR Glu122 and Glu60

(Figure 5.1), which indicates their possible function in drug binding, considering that CCCP has a positive charge.

In addition, different to QacR, VceR has an 8 amino acid insertion in the drug binding domain between helix 7 and helix 8 and a CCCH (Cys-Cys-Cys-His) motif (Figure 5.1). Future work has to determine the function of the CCCH motif, which may be involved in metal binding, and of this 8-residue insertion.

6.2.3 Induction mechanism of VceR

Upon binding of ligands, TetR and QacR undertake similar induction mechanisms (Section 1.10.1.3 and 1.10.2.2). Essentially, a conformational change in their C-terminal drug binding domains is propagated to the DNA-binding domain by helix connecting the two domains and this increases the distance between the midpoints of the two DNA recognition helices, which then do not fit in the major groove of the DNA, causing TetR and QacR to dissociate from their cognate DNA (Orth *et al*., 1998b; Orth *et al*., 2000; Schumacher *et al*., 2002). In addition, there is another species of TetR, revTetR, which is a derivative of TetR with a single site mutation and reverse activity, in that the binding of ligand increases its DNA-binding. RevTetR employs the disorder-order mechanism, which is that ligand-free revTetR has an unfolded DNA-binding domain, and the binding of ligand increases the folding of DNA-binding domain of revTetR that subsequently benefits DNA binding (Scholz *et al*., 2004; Resch *et al*., 2008). The induction mechanism of VceR is still unclear. Future work has to determine the crystal structures of VceR and the VceR/ligand complex to compare with that of VceR/DNA, which could show the induction mechanism of VceR.

References:

Aggarwal, A.K. (1990) Crystallization of DNA binding proteins with oligodeoxynucletides. *Methods: A companion to methods in Enzymology* 1: 83-90

Akeda, Y., and Galan, J.E. (2005) Chaperone release and unfolding of substrates in type III secretion. *Nature* 437: 911-915

Alfano, J.R., and Collmer, A. (1997) The Type III (Hrp) secretion pathway of plant pathogenic baceteria: Trafficking Harpins, Avr proteins, and Death. *Journal of Bacteriology* 179: 5655-5662

Alfano, J.R., and Collmer, A. (2004) Type III secretion system effector proteins: double agents in bacterial disease and plant defense. *Annu Rev Phytopathol* 42: 385-414

Alatoom, A.A., Aburto, R., Hamood, A.N. and Colmer-Hamood J.A. (2007) *vceR* negatively regulates the *vceCAB* MDR efflux operon and positively regulates its own synthesis in *Vibrio cholerae* 569B. *Can J. Microbiol*. 53(7): 888-900

Anderson, J., Ptashne, M. and Harrison, S.C. (1984) Cocrystals of the DNA-binding domain of phage 434 repressor and a synthetic phage 434 operator. *Proc. Natl Acad. Sci. USA* 81, 1307-1311

Arlat, M., Van Gijsegem, F., Huet, J.C., Pernollet, J.C. and Boucher, C.A. (1994) PopA1, a protein which induces a hypersensitive-like response on specific *Petunia* genotypes, is secreted via the Hrp pathway of *Pseudomonas solanacearum*. *EMBO J*. 13: 543-53

Azriel, R., and Gazit, E. (2001) Analysis of the minimal amyloid-forming fragment of the islet amyloid polypeptide. An experimental support for the key role of the phenylalanine residue in amyloid formation. *J Biol Chem* 276: 34156-34161

Bent, A.F., and Mackey, D. (2007) Elicitors, effectors, and R genes: the new paradigm and a lifetime supply of questions. *Annu Rev Phytopathol* 45: 399-436

Benzinger, T.L., Gregory, D.M., Burkoth, T.S., Miller-Auer, H., Lynn, D.G., Botto, R.E., and Meredith, S.C. (1998) Propagating structure of Alzheimer's beta-amyloid(10-35) is parallel beta-sheet with residues in exact register. *Proc Natl Acad Sci U S A* 95: 13407-13412

Benzinger, T.L., Gregory, D.M., Burkoth, T.S., Miller-Auer, H., Lynn, D.G., Botto, R.E., and Meredith, S.C. (2000) Two-dimensional structure of beta-amyloid(10-35) fibrils. *Biochemistry* 39: 3491-3499

Blaylock, B., Riordan, K.E., Missiakas, D.M., and Schneewind, O. (2006) Characterization of the *Yersinia enterocolitica* type III secretion ATPase YscN and its regulator YscL. *J Bacteriol* 188: 3525-3534

Bogdanove, A.J., Wei, Z.M., Zhao, L., and Beer, S.V. (1996) *Erwinia amylovora* secretes harpin via a type III pathway and contains a homolog of *yopN* of *Yersinia* spp. *J Bacteriol* 178: 1720-1730

Borges-Walmsley, M.I., McKeegan, K.S., and Walmsley, A.R. (2003) Structure and function of efflux pumps that confer resistance to drugs. *Biochem J* 376: 313-338

Borges-Walmsley, M.I., Du, D., McKeegan, K.S., Sharples, G.J., and Walmsley, A.R. (2005) VceR regulates the *vceCAB* drug efflux pump operon of *Vibrio cholerae* by alternating between mutually exclusive conformations that bind either drugs or promoter DNA. *J Mol Biol* 349: 387-400

Brennan, R.G. (2001) Introduction: multidrug resistance. *Seminars in Cell & Developmental Biology* 12: 201-204

Bricogne, G., Vonrhein, C., Flensburg, C., Schiltz, M. and Paciorek, W. (2003) Generation, representation and flow of phase information in structure determination: recent developments in and around SHARP 2.0. *Acta Cryst.* D59: 2023-2030

Buck, M.A. and Cooperman, B.S. (1990) Single protein omission reconstitution studies of tetracycline binding to the 30S subunit of *Escherichia coli* ribosomes. *Biochemistry* 29: 5374-9

Buttner, D., Nennstiel, D., Klusener, B., and Bonas, U. (2002) Functional analysis of HrpF, a putative type III translocon protein from *Xanthomonas campestris* pv. vesicatoria. *J Bacteriol* 184: 2389-2398

Cagliero, C., Maurel, M.C., Cloeckaert, A., and Payot, S. (2007) Regulation of the expression of the CmeABC efflux pump in *Campylobacter jejuni*: identification of a point mutation abolishing the binding of the CmeR repressor in an in vitro-selected multidrug-resistant mutant. *FEMS Microbiol Lett* 267: 89-94

Charkowski, A.O., Alfano, J.R., Preston, G., Yuan, J., He, S.Y., and Collmer, A. (1998) The *Pseudomonas syringae* pv. tomato HrpW protein has domains similar to harpins and pectate lyases and can elicit the plant hypersensitive response and bind to pectate. *J Bacteriol* 180: 5211-5217

Chaudhary, N., Singh, S. and Nagarai, R. (2008) Organic solvent mediated self-association of an amyloid forming peptide from beta2-microglobulin: an atomic force microscopy study. *Biopolymers* 90: 783-91

Chen, C.S., White, A., Love, J., Murphy, J. R. and Ringe, D. (2000) Methyl groups of thymine bases are important for nucleic acid recognition by DtxR. *Biochemistry* 39, 10397-10407

Chisholm, S.T., Coaker, G., Day, B., and Staskawicz, B.J. (2006) Host-microbe interactions: shaping the evolution of the plant immune response. *Cell* 124: 803-814

Chiti, F., Calamai, M., Taddei, N., Stefani, M., Ramponi, G and Dobson, C. M. (2002) Studies of the aggregation of mutant proteins *in vitro* provide insights into the genetics of amyloid diseases. *Proc. Natl Acad. Sci. USA* 99, 16419-16426

Chiti, F., and Dobson, C.M. (2006) Protein misfolding, functional amyloid, and human disease. *Annu Rev Biochem* 75: 333-366

Collaborative computational project, Number4, 1994, The CCP4 suite: programs for protein crystallography. *Acta Cryst.* D50: 760-763

Collins, S.R., Douglass, A., Vale, R.D., and Weissman, J.S. (2004) Mechanism of prion propagation: amyloid growth occurs by monomer addition. *PLoS Biol* 2: e321

Conchillo-Sole, O., de Groot, N. S., Aviles, F.X., Vendrell, J., Daura, X. and Ventura, S. (2007). AGGRESCAN: a server for the prediction and evaluation of "hot spots" of aggregation in polypeptides. *BMC Bioinformatics* 8: 65

Cornelis, G.R., and Van Gijsegem, F. (2000) Assembly and function of type III secretory systems. *Annu Rev Microbiol* 54: 735-774

Cornelis, G.R. (2006) The type III secretion injectisome. *Nat Rev Microbiol* 4: 811-825

Cowtan, K. (1994), Joint CCP4 and ESF-EACBM Newsletter on Protein Crystallography, 31, p34-38.

Crop prospects and food situation, No. 4, November 2009, Food and Agriculture organization (FAO)

Cruz, L., Urbanc, B., Borreguero, J.M., Lazo, N.D., Teplow, D.B., and Stanley, H.E. (2005) Solvent and mutation effects on the nucleation of amyloid beta-protein folding. *Proc Natl Acad Sci U S A* 102: 18258-18263

Deane, J.E., Graham, S.C., Mitchell, E.P., Flot, D., Johnson, S., and Lea, S.M. (2008) Crystal structure of Spa40, the specificity switch for the *Shigella flexneri* type III secretion system. *Molecular Microbiology* 69: 267-76

DeLano, W.L. The PyMOL Molecular Graphics System (2002) DeLano Scientific, San Carlos, CA, USA. http://www.pymol.org

Dong, H., Delaney, T.P., Bauer, D.W., and Beer, S.V. (1999) Harpin induces disease resistance in Arabidopsis through the systemic acquired resistance pathway mediated by salicylic acid and the *NIM1* gene. *Plant J* 20: 207-215

Dong, H.P., Peng, J., Bao, Z., Meng, X., Bonasera, J.M., Chen, G., Beer, S.V., and Dong, H. (2004) Downstream divergence of the ethylene signaling pathway for harpin-stimulated Arabidopsis growth and insect defense. *Plant Physiol* 136: 3628-3638

Dong, H.P., Yu, H., Bao, Z., Guo, X., Peng, J., Yao, Z., Chen, G., Qu, S., and Dong, H. (2005) The ABI2-dependent abscisic acid signalling controls HrpN-induced drought tolerance in Arabidopsis. *Planta* 221: 313-327

Dover, L.G., Corsino, P.E., Daniels, I.R., Cocklin, S.L., Tatituri, V., Besra, G.S., and Futterer, K. (2004) Crystal structure of the TetR/CamR family repressor *Mycobacterium tuberculosis* EthR implicated in ethionamide resistance. *J Mol Biol* 340: 1095-1105

Edqvist, P.J., Olsson, J., Lavander, M., Sundberg, L., Forsberg, A., Wolf-Watz, H., and Lloyd, S.A. (2003) YscP and YscU regulate substrate specificity of the *Yersinia* type III secretion system. *J Bacteriol* 185: 2259-2266

Emsley, P. and Cowtan, K. (2004) Coot: model-building tools for molecular graphics. *Acta Cryst.* D60: 2126-2132

Engel, M.F., Khemtemourian, L., Kleijer, C.C., Meeldijk, H.J., Jacobs, J., Verkleij, A.J., de Kruijff, B., Killian, J.A., and Hoppener, J.W. (2008) Membrane damage by human islet amyloid polypeptide through fibril growth at the membrane. *Proc Natl Acad Sci U S A* 105: 6033-6038

Engohang-Ndong, J., Baillat, D., Aumercier, M., Bellefontaine, F., Besra, G.S., Locht, C., and Baulard, A.R. (2004) EthR, a repressor of the TetR/CamR family implicated in ethionamide resistance in mycobacteria, octamerizes cooperatively on its operator. *Molecular Microbiology* 51: 175-188

Fändrich, M., Fletcher, M.A., and Dobson, C.M. (2001) Amyloid fibrils from muscle myoglobin. *Nature* 410: 165-166

Fändrich, M., and Dobson, C.M. (2002) The behaviour of polyamino acids reveals an inverse side chain effect in amyloid structure formation. *EMBO J.* 21: 5682-5690

Fändrich, M. (2007) On the structural definition of amyloid fibrils and other polypeptide aggregates *Cell. Mol. Life Sci*. 64: 2066-2078

Fändrich, M., Forge, V., Buder, K., Kittler, M., Dobson, C.M. and Diekmann, S. (2003). Myoglobin forms amyloid fibrils by association of unfolded polypeptide segments. *PNAS* 100 (26): 15463-15468

Faruque, S.M., Albert, M.J. and Mekalanos, J.J. (1998) Epidemiology, genetics and

ecology of toxigenic *Vibrio cholera Microbiology and Molecular Biology Reveiws*, 1301-1314

Faruque, S.M. and Nair, G.B. (2008) *Vibrio cholera*: genomics and molecular biology. Caister Academic Press

Federici, L., Du, D., Walas, F., Matsumura, H., Fernandez-Recio, J., McKeegan, K.S., Borges-Walmsley, M.I., Luisi, B.F., and Walmsley, A.R. (2005) The crystal structure of the outer membrane protein VceC from the bacterial pathogen *Vibrio cholerae* at 1.8 Å resolution. *J Biol Chem* 280: 15307-15314

Ferrao-Gonzales, A.D., Souto, S.O., Silva, J.L. and Foguel, D. (2000) The preaggregated state of an amyloidogenic protein: Hydrostatic pressure converts native transthyretin into the amyloidogenic state. *Proc. Natl. Acad. Sci. USA* 97: 6445-50

Ferris, H.U., and Minamino, T. (2006) Flipping the switch: bringing order to flagellar assembly. *Trends Microbiol* 14: 519-526

Folster, J.P., and Shafer, W.M. (2005) Regulation of *mtrF* expression in *Neisseria gonorrhoeae* and its role in high-level antimicrobial resistance. *J Bacteriol* 187: 3713-3720

Folster, J.P., Dhulipala, V., Nicholas, R.A., and Shafer, W.M. (2007) Differential regulation of *ponA* and *pilMNOPQ* expression by the MtrR transcriptional regulatory protein in *Neisseria gonorrhoeae*. *J Bacteriol* 189: 4569-4577

Frenois, F., Engohang-Ndong, J., Locht, C., Baulard, A.R., and Villeret, V. (2004) Structure of EthR in a ligand bound conformation reveals therapeutic perspectives against tuberculosis. *Mol Cell* 16: 301-307

Gabriel, D.W. (1999) Why do pathogens carry avirulence genes? *Physiological and Molecular plant pathology* 55: 205-214

Gazit, E. (2002) A possible role for pi-stacking in the self-assembly of amyloid fibrils. *Faseb J* 16: 77-83

Gazit, E. (2005) Mechanisms of amyloid fibril self-assembly and inhibition. Model short peptides as a key research tool. *Febs J* 272: 5971-5978

Gazit, E. (2007) Self assembly of short aromatic peptides into amyloid fibrils and related nanostructures. *Prion* 1: 32-35

Gerber, R., Tahiri-Alaoui, A., Hore, P.J. and James, W. (2008) Conformational pH dependence of intermediate states during oligomerization of the human prion protein. *Protein Science* 17: 537-544

Ghosh, P. (2004) Process of protein transport by the type III secretion system. *Microbiol Mol Biol Rev* 68: 771-795

Glabe, C.G. (2006) Common mechanisms of amyloid oligomer pathogenesis in degenerative disease. *Neurobiol Aging* 27: 570-575

Glass, R.I., I. Huq, A.R.M.A. Alim, and Yunus, M. (1980) Emergence of multiple antibiotic-resistant *Vibrio cholera* in Bangladesh. *J. Infect. Dis.* 142: 939-942

Gnanamanickam, S.S., Priyadarisini, V.B., Narayanan, N.N., Vasudevan, P. and Kavitha, S. (1999) An overview of bacterial blight disease of rice and strategies for management. *Current Science* 77: 1435-1443

Gophna, U., Ron, E.Z., and Graur, D. (2003) Bacterial type III secretion systems are ancient and evolved by multiple horizontal-transfer events. *Gene* 312: 151-163

Green, D.R., and Reed, J.C. (1998) Mitochondria and apoptosis. *Science* 281: 1309-1312

Greenberg, J.T. (1996) Programmed cell death: a way of life for plants. *Proc Natl Acad Sci U S A* 93: 12094-12097

Grkovic, S., Brown, M.H., Roberts, N.J., Paulsen, I.T., and Skurray, R.A. (1998) QacR is a repressor protein that regulates expression of the *Staphylococcus aureus* multidrug efflux pump QacA. *J Biol Chem* 273: 18665-18673

Grkovic, S., Brown, M.H., and Skurray, R.A. (2001) Transcriptional regulation of multidrug efflux pumps in bacteria. *Semin Cell Dev Biol* 12: 225-237

Gu, R., Su, C.C., Shi, F., Li, M., McDermott, G., Zhang, Q., and Yu, E.W. (2007) Crystal structure of the transcriptional regulator CmeR from *Campylobacter jejuni*. *J Mol Biol* 372: 583-593

Gurlebeck, D., Thieme, F., and Bonas, U. (2006) Type III effector proteins from the plant pathogen *Xanthomonas* and their role in the interaction with the host plant. *J Plant Physiol* 163: 233-255

Hagman, K.E., Pan, W., Spratt, B.G., Balthazar, J.T., Judd, R.C., and Shafer, W.M. (1995) Resistance of *Neisseria gonorrhoeae* to antimicrobial hydrophobic agents is modulated by the MtrRCDE efflux system. *Microbiology* 141 (Pt 3): 611-622

Harrison, J.W. and Svec, T.A. (1998) The beginning of the end of the antibiotic era? Part I. The problem: abuse of the 'miracle drugs' *Quintessence Int.* 29: 151-62

He, S.Y., Huang, H.C., and Collmer, A. (1993) *Pseudomonas syringae* pv. syringae harpinPss: a protein that is secreted via the Hrp pathway and elicits the hypersensitive response in plants. *Cell* 73: 1255-1266

He, S.Y., and Jin, Q. (2003) The Hrp pilus: learning from flagella. *Curr Opin Microbiol* 6: 15-19

Heath, M.C. (2000a) Hypersensitive response-related death. *Plant Mol Biol*. 44(3): 321-34

Heath, M.C. (2000b) Nonhost resistance and nonspecific plant defenses. *Curr Opin Plant Biol* **3**: 315-319

Hernandez, A., Mate, M.J., Sanchez-Diaz, P.C., Romero, A., Rojo, F., and Martinez, J.L. (2009) Structural and functional analysis of SmeT, the repressor of the *Stenotrophomonas maltophilia* multidrug efflux pump SmeDEF. *J Biol Chem* 284: 14428-14438

Hinrichs, W., Kisker, C., Duvel, M., Muller, A., Tovar, K., Hillen, W., and Saenger, W. (1994) Structure of the Tet repressor-tetracycline complex and regulation of antibiotic resistance. *Science* 264: 418-420

Hoffmann, K.M., Williams, D., Shafer, W.M., and Brennan, R.G. (2005) Characterization of the multiple transferable resistance repressor, MtrR, from *Neisseria gonorrhoeae*. *J Bacteriol* 187: 5008-5012

Hoyos, M.E., Stanley, C.M., He, S.Y., Pike, S., Pu, X-A. and Novacky, A. (1996) The interaction of HarpinPss, with plant cell walls. *MPMI* 9: 608-616

Jang, Y.S., Sohn, S.I., and Wang, M.H. (2006) The *hrpN* gene of *Erwinia amylovora* stimulates tobacco growth and enhances resistance to *Botrytis cinerea*. *Planta* 223: 449-456

Jimenez, J.L., Guijarro, J.I., Orlova, E., Zurdo, J., Dobson, C.M., Sunde, M., and Saibil, H.R. (1999) Cryo-electron microscopy structure of an SH3 amyloid fibril and model of the molecular packing. *EMBO J*. 18: 815-821

Jimenez, J.L., Nettleton, E.J., Bouchard, M., Robinson, C.V., Dobson, C.M., and Saibil, H.R. (2002) The protofilament structure of insulin amyloid fibrils. *Proc Natl Acad Sci U S A* 99: 9196-9201

Jones, J.D., and Dangl, J.L. (2006) The plant immune system. *Nature* 444: 323-329

Kabsch, W. (1988) Evaluation of single-crystal X-ray diffraction data from a postion-sensitive detector. *J. Appl. Cryst*. 21, 916-924

Kajava, A.V., Aebi, U., and Steven, A.C. (2005) The parallel superpleated beta-structure as a model for amyloid fibrils of human amylin. *J Mol Biol* 348: 247-252

Kayed, R., Head, E., Thompson, J.L., Mclntire, T.M., Milton, S.C., Cotman, C.W. and Glabe, C.G. (2003) Common structure of soluble amyloid oligomers implies common mechanism of pathogenesis *Science* 300: 486-489

Kayed, R., Sokolov, Y., Edmonds, B., McIntire, T.M., Milton, S.C., Hall, J.E., and Glabe, C.G. (2004) Permeabilization of lipid bilayers is a common conformation-dependent activity of soluble amyloid oligomers in protein misfolding diseases. *J Biol Chem* 279: 46363-46366.

Kay, S. and Bonas, U. (2009) How *Xanthomonas* type III effectors manipulate the host plant. *Current opinion in Microbiology* 12: 37-43

Kelly, J.W., and Balch, W.E. (2003) Amyloid as a natural product. *J Cell Biol* 161: 461-462

Kim, J.F., and Beer, S.V. (1998) HrpW of *Erwinia amylovora*, a new harpin that contains a domain homologous to pectate lyases of a distinct class. *J Bacteriol* 180: 5203-5210

Kim, J.G., Jeon, E., Oh, J., Moon, J.S., and Hwang, I. (2004) Mutational analysis of *Xanthomonas* harpin HpaG identifies a key functional region that elicits the hypersensitive response in nonhost plants. *J Bacteriol* 186: 6239-6247

Kisker, C., Hinrichs, W., Tovar, K., Hillen, W., and Saenger, W. (1995) The complex formed between Tet repressor and tetracycline-Mg^{2+} reveals mechanism of antibiotic resistance. *J Mol Biol* 247: 260-280

Klotzsche, M., Berens, C., and Hillen, W. (2005) A peptide triggers allostery in tet repressor by binding to a unique site. *J Biol Chem* 280: 24591-24599

Konig, B., Muller, J.J., Lanka, E. and Heinemann, U. (2009) Crystal structure of KorA bound to operator DNA: insight into repressor cooperation in *RP4* gene regulation. *Nucleic Acids Research*. 37, 1915-1924

Krell, T., Teran, W., Mayorga, O. L., Rivas, G., Jimenez, M., Daniels, C., Molina-Henares, A. Martinez-Bueno, M., Gallegos, M. and Ramos, J. (2007) Optimization of the palindromic order of the TtgR operator enhances binding cooperativity. *J. Mol. Biol.* 369, 1188-1199

Krishnan, R., and Lindquist, S.L. (2005) Structural insights into a yeast prion illuminate nucleation and strain diversity. *Nature* 435: 765-772

Kumar, A., and Schweizer, H.P. (2005) Bacterial resistance to antibiotics: active efflux and reduced uptake. *Adv Drug Deliv Rev* 57: 1486-1513

Kumar, S., Mohanty, S.K., and Udgaonkar, J.B. (2007) Mechanism of formation of amyloid protofibrils of barstar from soluble oligomers: evidence for multiple steps and lateral association coupled to conformational conversion. *J Mol Biol* 367: 1186-1204

Kvitko, B.H., Ramos, A.R., Morello, J.E., Oh, H.S., and Collmer, A. (2007) Identification of harpins in *Pseudomonas syringae* pv. tomato DC3000, which are functionally similar to HrpK1 in promoting translocation of type III secretion system effectors. *J Bacteriol* 189: 8059-8072

Lai, Z., Colon, W., and Kelly, J.W. (1996) The acid-mediated denaturation pathway of transthyretin yields a conformational intermediate that can self-assemble into amyloid. *Biochemistry* 35: 6470-6482

Lee, E.H., Rouquette-Loughlin, C., Folster, J.P., and Shafer, W.M. (2003) FarR regulates the *farAB*-encoded efflux pump of *Neisseria gonorrhoeae* via an MtrR regulatory mechanism. *J Bacteriol* 185: 7145-7152

Lee, J.H., Bhak, G., Lee, S.G. and Paik, S.R. (2008) Instantaneous amyloid fibril formation of α-synuclein from the oligomeric granular structures in the presence of hexane. *Biophysical Journal: Biophysical letters* 95(2): L16-L18

Lee, J., Klusener, B., Tsiamis, G., Stevens, C., Neyt, C., Tampakaki, A.P., Panopoulos, N.J., Noller, J., Weiler, E.W., Cornelis, G.R., Mansfield, J.W., and Nurnberger, T. (2001) HrpZPsph from the plant pathogen *Pseudomonas syringae* pv. phaseolicola binds to lipid bilayers and forms an ion-conducting pore *in vitro*. *Proc. Natl. Acad. Sci. USA* 98: 289-294

Li, C.M., Haapalainen, M., Lee, J., Nurnberger, T., Romantschuk, M., and Taira, S. (2005) Harpin of *Pseudomonas syringae* pv. phaseolicola harbors a protein binding site. *Mol Plant Microbe Interact* 18: 60-66

Li, M., Gu, R., Su, C.C., Routh, M.D., Harris, K.C., Jewell, E.S., McDermott, G., and Yu, E.W. (2007) Crystal structure of the transcriptional regulator AcrR from *Escherichia coli*. *J Mol Biol* 374: 591-603

Lin, J., Akiba, M., Sahin, O., and Zhang, Q. (2005a) CmeR functions as a transcriptional repressor for the multidrug efflux pump CmeABC in *Campylobacter jejuni*. *Antimicrob Agents Chemother* 49: 1067-1075

Lin, J., Cagliero, C., Guo, B., Barton, Y.W., Maurel, M.C., Payot, S., and Zhang, Q. (2005b) Bile salts modulate expression of the CmeABC multidrug efflux pump in *Campylobacter jejuni*. *J Bacteriol* 187: 7417-7424

Lopez De La Paz, M., Goldie, K., Zurdo, J., Lacroix, E., Dobson, C.M., Hoenger, A., and Serrano, L. (2002) *De novo* designed peptide-based amyloid fibrils. *Proc Natl Acad Sci USA* 99: 16052-16057

Lorenz, C., Kirchner, O., Egler, M., Stuttmann, J., Bonas, U. and Buttner, D. (2008a) HpaA from *Xanthomonas* is a regulator of type III secretion. *Molecular Microbiology* 69: 344-360

Lorenz, C., Schulz, S., Wolsch, T., Rossier, O., Bonas, U., and Buttner, D. (2008b) HpaC controls substrate specificity of the *Xanthomonas* type III secretion system. *PLoS Pathog* 4: e1000094

Lorenz, C., and Buttner, D. (2009) Functional characterization of the type III secretion ATPase HrcN from the plant pathogen *Xanthomonas campestris* pv. vesicatoria. *J Bacteriol* 191: 1414-1428

Lucas, C.E., Balthazar, J.T., Hagman, K.E., and Shafer, W.M. (1997) The MtrR repressor binds the DNA sequence between the *mtrR* and *mtrC* genes of *Neisseria gonorrhoeae*. *J Bacteriol* 179: 4123-4128

Luckner, S.R., Klotzsche, M., Berens, C., Hillen, W., and Muller, Y.A. (2007) How an agonist peptide mimics the antibiotic tetracycline to induce Tet-repressor. *J Mol Biol* 368: 780-790

Macnab, R.M. (2003) How bacteria assemble flagella. *Annu Rev Microbiol* 57: 77-100

Malisauskas, M., Zamotin, V., Jass, J., Noppe, W., Dobson, C.M. and Morozova-Roche L.A. (2003) Amyloid protofilaments from the calcium-binding protein equine lysozyme: formation of ring and linear structures depends on pH and metal ion concentration *J. Mol. Biol*. 330: 879-90

McKeegan, K.S., Borges-Walmsley, M.I., and Walmsley, A.R. (2004) Structural understanding of efflux-mediated drug resistance: potential routes to efflux inhibition. *Curr Opin Pharmacol **4**:* 479-486

Mishima, T., Ohkuri, T., Monji, A. Imoto, T. and Ueda, T. (2007) A particular hydrophobic cluster in the residual structure of reduced lysozyme drastically affects the amyloid fibrils formation. *Biochem. Biophys. Res. Commun.* 356: 769-772

Morozova-Roche, L.A., Zurdo, J., Spencer, A., Noppe, W., Receveur, V., Archer, D.B., Joniau, M., and Dobson, C.M. (2000) Amyloid fibril formation and seeding by wild-type human lysozyme and its disease-related mutational variants. *J Struct Biol* 130: 339-351

Murray, D.S., Schumacher, M.A., and Brennan, R.G. (2004) Crystal structures of QacR-diamidine complexes reveal additional multidrug-binding modes and a novel mechanism of drug charge neutralization. *J Biol Chem* 279: 14365-14371

Nelson, R., Sawaya, M.R., Balbirnie, M., Madsen, A.O., Riekel, C., Grothe, R., and Eisenberg, D. (2005) Structure of the cross-beta spine of amyloid-like fibrils. *Nature* 435: 773-778

Noel, L., Thieme, F., Nennstiel, D., and Bonas, U. (2002) Two novel type III-secreted proteins of *Xanthomonas campestris* pv. vesicatoria are encoded within the *hrp* pathogenicity island. *J Bacteriol* 184: 1340-1348

Oh, C.S., and Beer, S.V. (2007) AtHIPM, an ortholog of the apple HrpN-interacting protein, is a negative regulator of plant growth and mediates the growth-enhancing effect of HrpN in Arabidopsis. *Plant Physiol* 145: 426-436

Oh, J., Kim, J.G., Jeon, E., Yoo, C.H., Moon, J.S., Rhee, S., and Hwang, I. (2007) Amyloidogenesis of type III-dependent harpins from plant pathogenic bacteria. *J Biol Chem* 282: 13601-13609

Ohtsuka, K. and Hata, M (2000) Molecular chaperone function of mammalian Hsp70 and Hsp40—a review. *Int. J. Hyperthermia*. 16(3): 231-45

Orth, P., Alings, C., Schnappinger, D., Saenger, W., and Hinrichs, W. (1998a) Crystallization and preliminary X-ray analysis of the Tet-repressor/operator complex. *Acta Cryst.* D54: 99-100

Orth, P., Cordes, F., Schnappinger, D., Hillen, W., Saenger, W., and Hinrichs, W. (1998b) Conformational changes of the Tet repressor induced by tetracycline trapping. *J Mol Biol* 279: 439-447

Orth, P., Saenger, W., and Hinrichs, W. (1999) Tetracycline-chelated Mg^{2+} ion initiates helix unwinding in Tet repressor induction. *Biochemistry* 38: 191-198

Orth, P., Schnappinger, D., Hillen, W., Saenger, W., and Hinrichs, W. (2000) Structural basis of gene regulation by the tetracycline inducible Tet repressor-operator system. *Nat Struct Biol* **7**: 215-219

Otwinowski, Z. and Minor, W. (1997) Processing of X-ray diffraction data collected in oscillation mode. Methods in Enzymology Volumne 276: Macromolecular Crystallography, partA, p.307-326, C.W. Carter, Jr. and R.M. Sweet, Eds

Page, R., Grzechnik, S. K., Canaves, J. M., Spraggon, G., Kreusch, A., Kuhn, P., Stevens, R. C. & Lesley, S. A. (2003). *Acta Cryst*. D59, 1028-1037

Paul, K., Erhardt, M., Hirano, T., Blair, D.F., and Hughes, K.T. (2008) Energy source of flagellar type III secretion. *Nature* 451: 489-492

Peng, J., Bao, Z., Ren, H., Wang, J. and Dong, H. (2004) Expression of $Harpin_{Xoo}$ in transgenic tobacco induces pathogen defense in the absence of hypersensitive cell death. *Phytopathology* 94: 1048-1055

Petkova, A.T., Ishii, Y., Balbach, J.J., Antzutkin, O.N., Leapman, R.D., Delaglio, F., and Tycko, R. (2002) A structural model for Alzheimer's beta -amyloid fibrils based on experimental constraints from solid state NMR. *Proc Natl Acad Sci USA* 99: 16742-16747

Pohl, E., Holmes, R.K. and Hol, W.G.J. (1999) Crystal structure of a cobalt-activated diphtheria toxin repressor-DNA complex reveals a metal-binding SH3-like domain. *J. Mol. Biol*. 292, 653-667

Pohl, E., Pradervand, C., Schneider, R., Tomizaki, T., Pauluhn, A., Chen, Q., Ingold, G., Zimoch, E. and Schulze-Briese, C. (2006) Facility update: the new protein crystallography beamline X10SA at the Swiss Light Source. *Synchrotron Radiation News* 19(1): 24-26

Pozidis, C., Chalkiadaki, A., Gomez-Serrano, A., Stahlberg, H., Brown, I., Tampakaki, A.P., Lustig, A., Sianidis, G., Politou, A.S., Engel, A., Panopoulos, N.J., Mansfield, J., Pugsley, A.P., Karamanou, S., and Economou, A. (2003) Type III protein translocase: HrcN is a peripheral ATPase that is activated by oligomerization. *J Biol Chem* 278: 25816-25824

Quist, A., Doudevski, I., Lin, H., Azimova, R., Ng, D., Frangione, B., Kagan, B., Ghiso, J., and Lal, R. (2005) Amyloid ion channels: a common structural link for protein-misfolding disease. *Proc Natl Acad Sci USA* 102: 10427-10432

Racape, J., Belbahri, L., Engelhardt, S., Lacombe, B., Lee, J., Lochman, J., Marais, A., Nicole, M., Nurnberger, T., Parlange, F., Puverel, S., and Keller, H. (2005) Ca^{2+}-dependent lipid binding and membrane integration of PopA, a harpin-like elicitor of the hypersensitive response in tobacco. *Molecular Microbiology* 58: 1406-1420

Ramos, J.L., Martinez-Bueno, M., Molina-Henares, A.J., Teran, W., Watanabe, K., Zhang, X., Gallegos, M.T., Brennan, R., and Tobes, R. (2005) The TetR family of transcriptional repressors. *Microbiol Mol Biol Rev* 69: 326-356

Resch, M., Striegl, H., Henssler, E.M., Sevvana, M., Egerer-Sieber, C., Schiltz, E., Hillen, W. and Muller, Y.A. (2008) A protein functional leap: how a single mutation reverses the function of the transcription regulator TetR. *Nucleic Acids Research* 36, 4390-4401

Routledge, K.E., Tartaglia, G.G., Platt, G.W., Vendruscolo, M. and Radford, S.E. (2009) Competition between intramolecular and intermolecular interactions in an amyloid-forming protein. *J. Mol. Biol*. 389: 776-786

Sachse, C., Fandrich, M., and Grigorieff, N. (2008) Paired beta-sheet structure of an Abeta(1-40) amyloid fibril revealed by electron microscopy. *Proc Natl Acad Sci USA* 105: 7462-7466

Sanchez, P., Alonso, A., and Martinez, J.L. (2002) Cloning and characterization of SmeT, a repressor of the *Stenotrophomonas maltophilia* multidrug efflux pump SmeDEF. *Antimicrob Agents Chemother* 46: 3386-3393

Sawaya, M.R., Sambashivan, S., Nelson, R., Ivanova, M.I., Sievers, S.A., Apostol, M.I., Thompson, M.J., Balbirnie, M., Wiltzius, J.J., McFarlane, H.T., Madsen, A.O., Riekel, C., and Eisenberg, D. (2007) Atomic structures of amyloid cross-beta spines reveal varied steric zippers. *Nature* 447: 453-457

Schmitt, J.P. and Scholtz, J.M. (2003) The role of protein stability, solubility and net charge in amyloid fibril formation. *Protein Sci.* 12, 2374-2378

Schneider, T.R. and Sheldrick, G.M. (2002) Substructure solution with ShelxD *Acta Cryst.* D58: 1772-1779

Scholz, O., Henβler, E., Bail, J., Schubert, P., Bogdanska-Urbaniak, J., Sopp, S., Reich, M., Wisshak, S., Kostner, M., Bertram, R. and Hillen, W. (2004) Activity reversal of Tet repressor caused by single amino acid exchanges. *Molecular Microbiology* 53(3), 777-789

Schumacher, M.A., Miller, M.C., Grkovic, S., Brown, M.H., Skurray, R.A., and Brennan, R.G. (2001) Structural mechanisms of QacR induction and multidrug recognition. *Science* 294: 2158-2163

Schumacher, M.A., and Brennan, R.G. (2002) Structural mechanisms of multidrug recognition and regulation by bacterial multidrug transcription factors. *Molecular Microbiology* 45: 885-893

Schumacher, M.A., Miller, M.C., Grkovic, S., Brown, M.H., Skurray, R.A., and Brennan, R.G. (2002) Structural basis for cooperative DNA binding by two dimers of the multidrug-binding protein QacR. *EMBO J.* 21: 1210-1218

Schumacher, M.A., Miller, M.C., and Brennan, R.G. (2004) Structural mechanism of the simultaneous binding of two drugs to a multidrug-binding protein. *EMBO J.* 23: 2923-2930

Seo, Y.S., Sriariyanun, M., Wang, L., Pfeiff, J., Phetsom, J., Lin, Y., Jung, K.H., Chou, H.H., Bogdanove, A., and Ronald, P. (2008) A two-genome microarray for the rice pathogens *Xanthomonas oryzae* pv. oryzae and *X. oryzae* pv. oryzicola and its use in the discovery of a difference in their regulation of *hrp* genes. *BMC Microbiol* 8: 99

Serio, T.R., Cashikar, A.G., Kowal, A.S., Sawicki, G.J., Moslehi, J.J., Serpell, L., Arnsdorf, M.F., and Lindquist, S.L. (2000) Nucleated conformational conversion and the replication of conformational information by a prion determinant. *Science* 289: 1317-1321

Shao, M., Wang, J., Dean, R.A., Lin, Y., Gao, X., and Hu, S. (2008) Expression of a harpin-encoding gene in rice confers durable nonspecific resistance to *Magnaporthe grisea*. *Plant Biotechnol J* 6: 73-81

Sheldrick, G.M. (2008) A short history of SHELX *Acta Cryst*. A64: 112-122

Shorter, J. (2008) Hsp104: a weapon to combat diverse neurodegenerative disorders. *Neurosignals.* 16: 63-74

Shorter, J. and Lindquist, S. (2008) Hsp104, Hsp70 and Hsp40 interplay regulates formation, growth and elimination of Sup35 prions. *EMBO J*. 27: 2712-2724

Smith, D.P., Jones, S., Serpell, L.C., Sunde, M., and Radford, S.E. (2003) A systematic investigation into the effect of protein destabilisation on beta 2-microglobulin amyloid formation. *J Mol Biol* 330: 943-954

Sorg, I., Wagner, S., Amstutz, M., Muller, S.A., Broz, P., Lussi, Y., Engel, A., and Cornelis, G.R. (2007) YscU recognizes translocators as export substrates of the *Yersinia injectisome*. *EMBO J.* 26: 3015-3024

Stefani, M., and Dobson, C.M. (2003) Protein aggregation and aggregate toxicity: new insights into protein folding, misfolding diseases and biological evolution. *J Mol Med* 81: 678-699

Stohr, J., Weinmann, N., Wille, H., Kaimann, T., Nagel-Steger, L., Birkmann, E., Panza, G., Prusiner, S.B., Eigen, M., and Riesner, D. (2008) Mechanisms of prion protein assembly into amyloid. *Proc Natl Acad Sci USA* 105: 2409-2414

Tampakaki, A.P., Fadouloglou, V.E., Gazi, A.D., Panopoulos, N.J., and Kokkinidis, M. (2004) Conserved features of type III secretion. *Cell Microbiol* 6: 805-816

Tan, S., Hunziker, Y., Pellegrini, L. and Richmond, T.J. (2000) Crystallization of the Yeast MATα2/MCM1/DNA ternary complex: general methods and principles for protein/DNA cocrystallization. *J. Mol. Biol.* 297: 947-959

Tardy, F., Homble, F., Neyt, C., Wattiez, R., Cornelis, G.R., Ruysschaert, J.M., and Cabiaux, V. (1999) *Yersinia enterocolitica* type III secretion-translocation system: channel formation by secreted Yops. *EMBO J.* 18: 6793-6799

Taylor, G. (2003) The phase problem. *Acta Cryst.* D59: 1881-1890

Tjernberg, L., Hosia, W., Bark, N., Thyberg, J., and Johansson, J. (2002) Charge attraction and beta propensity are necessary for amyloid fibril formation from tetrapeptides. *J Biol Chem* 277: 43243-43246

Tjernberg, L.O., Callaway, D.J., Tjernberg, A., Hahne, S., Lilliehook, C., Terenius, L., Thyberg, J., and Nordstedt, C. (1999) A molecular model of Alzheimer amyloid beta-peptide fibril formation. *J Biol Chem* 274: 12619-12625

Torrent, J., Alvarez-Martinez, M.T., Harricane, M.C., Heitz, F., Liautard, J.P., Balny, C., and Lange, R. (2004) High pressure induces scrapie-like prion protein misfolding and amyloid fibril formation. *Biochemistry* 43: 7162-7170

Torrent, J., Alvarez-Martinez, M.T., Liautard, J.P., and Lange, R. (2006) Modulation of prion protein structure by pressure and temperature. *Biochim Biophys Acta* 1764: 546-551

Touze, T., Eswaran, J., Bokma, E., Koronakis, E., Hughes, C., and Koronakis, V. (2004) Interactions underlying assembly of the *Escherichia coli* AcrAB-TolC multidrug efflux system. *Molecular Microbiology* 53: 697-706

Uversky, V.N., and Fink, A.L. (2004) Conformational constraints for amyloid fibrillation: the importance of being unfolded. *Biochim Biophys Acta* 1698: 131-153

Vestergaard, B., Groenning, M., Roessle, M., Kastrup, J.S., van de Weert, M., Flink, J.M., Frokjaer, S., Gajhede, M., and Svergun, D.I. (2007) A helical structural nucleus is the primary elongating unit of insulin amyloid fibrils. *PLoS Biol* 5: e134

Walsh, C. (2000) Molecular mechanisms that confer antibacterial drug resistance. *Nature* 406: 775-781

Weber, E., Ojanen-Reuhs, T., Huguet, E., Hause, G., Romantschuk, M., Korhonen, T.K., Bonas, U., and Koebnik, R. (2005) The type III-dependent Hrp pilus is required for productive interaction of *Xanthomonas campestris* pv. vesicatoria with pepper host plants. *J Bacteriol* 187: 2458-2468

Wei, Z.M., Laby, R.J., Zumoff, C.H., Bauer, D.W., He, S.Y., Collmer, A., and Beer, S.V. (1992) Harpin, elicitor of the hypersensitive response produced by the plant pathogen *Erwinia amylovora*. *Science* 257: 85-88

White, A., Ding, X., vanderSpek, J.C., Murphy, J.R. and Ringe, D. (1998) Structure of the metal-ion-activated diphtheria toxin repressor/tox operator complex. *Nature* 394: 502-506

Whitmore, L., and Wallace, B.A. (2004) DICHROWEB, an online server for protein secondary structure analyses from circular dichroism spectroscopic data. *Nucleic Acids Res* 32: W668-673

Whitmore, L., and Wallace, B.A. (2008) Protein secondary structure analyses from circular dichroism spectroscopy: methods and reference databases. *Biopolymers* 89: 392-400

Woolley, R.C., Vediyappan, G., Anderson, M., Lackey, M., Ramasubramanian, B., Jiangping, B., Borisova, T., Colmer, J.A., Hamood, A.N., McVay, C.S., and Fralick, J.A. (2005) Characterization of the *Vibrio cholerae vceCAB* multiple-drug resistance efflux operon in *Escherichia coli*. *J Bacteriol* 187: 5500-5503

Wu, X., Wu, T., Long, J., Yin, Q., Zhang, Y., Chen, L., Liu, R., Gao, T., and Dong, H. (2007) Productivity and biochemical properties of green tea in response to full-length and functional fragments of HpaG $_{Xooc}$, a harpin protein from the bacterial rice leaf streak pathogen *Xanthomonas oryzae* pv. oryzicola. *J Biosci* 32: 1119-1131

Yang, B., Zhu, W., Johnson, L.B., and White, F.F. (2000) The virulence factor AvrXa7 of *Xanthomonas oryzae* pv. oryzae is a type III secretion pathway-dependent nuclear-localized double-stranded DNA-binding protein. *Proc Natl Acad Sci USA* 97: 9807-9812

Yang, B., and White, F.F. (2004) Diverse members of the AvrBs3/PthA family of type III effectors are major virulence determinants in bacterial blight disease of rice. *Mol Plant Microbe Interact* 17: 1192-1200

Zarivach, R., Deng, W., Vuckovic, M., Felise, H.B., Nguyen, H.V., Miller, S.I., Finlay, B.B., and Strynadka, N.C. (2008) Structural analysis of the essential self-cleaving type III secretion proteins EscU and SpaS. *Nature* 453: 124-127

Zgurskaya, H.I., and Nikaido, H. (2000) Multidrug resistance mechanisms: drug efflux across two membranes. *Molecular Microbiology* 37: 219-225

Zhao, B., Ardales, E.Y., Raymundo, A., Bai, J., Trick, H.N., Leach, J.E., and Hulbert, S.H. (2004) The *avrRxo1* gene from the rice pathogen *Xanthomonas oryzae* pv. oryzicola confers a nonhost defense reaction on maize with resistance gene *Rxo1*. *Mol Plant Microbe Interact* 17: 771-779

Zhao, B., Lin, X., Poland, J., Trick, H., Leach, J., and Hulbert, S. (2005) A maize resistance gene functions against bacterial streak disease in rice. *Proc Natl Acad Sci USA* 102: 15383-15388

Zhu, W., Yang, B., Chittoor, J.M., Johnson, L.B., and White, F.F. (1998) AvrXa10 contains an acidic transcriptional activation domain in the functionally conserved C terminus. *Mol Plant Microbe Interact* 11: 824-832

Zhu, W., MaGbanua, M.M., and White, F.F. (2000) Identification of two novel hrp-associated genes in the hrp gene cluster of *Xanthomonas oryzae* pv. oryzae. *J Bacteriol* 182: 1844-1853

Zou, L.F., Wang, X.P., Xiang, Y., Zhang, B., Li, Y.R., Xiao, Y.L., Wang, J.S., Walmsley, A.R., and Chen, G.Y. (2006) Elucidation of the hrp clusters of *Xanthomonas oryzae* pv. oryzicola that control the hypersensitive response in nonhost tobacco and pathogenicity in susceptible host rice. *Appl Environ Microbiol* 72: 6212-6224